Spin Dependent Forces in a Planar Paul Trap

Dissertation

zur Erlangung des Grades

"Doktor

der Naturwissenschaften"

am Fachbereich Physik, Mathematik und Informatik

der Johannes Gutenberg-Universität

in Mainz

Jens Welzel
geb. am 05.01.1985 in Überlingen

Radolfzell, den 14.10.2023

Abstract

In this work the quantum dynamics of single trapped ions and ion crystals in linear or planar configurations are investigated under the exposure to *transverse* magnetic field gradients. A surface-electrode Paul trap is employed to trap $^{40}Ca^{+}$ ions. The trap features submerged current-carrying wires to generate magnetic field gradients of up to 16.3(9) T/m. This gradient is aligned in the direction perpendicular to the axis of weakest confinement, along which linear ion crystals are formed.

With this setup and using the Zeeman levels m=+1/2=$|\uparrow\rangle$ and m=-1/2=$|\downarrow\rangle$ of the electronic ground state $S_{1/2}$ of the ions, fast Rabi oscillations with t_{π}=0.55 μs are driven, with HF radiation near 10 MHz with a coherence time up to $t_{coh} = 0.5$ ms. It will be demonstrated, that the magnetic field gradient couples the internal degree of the ions, i.e. the spin of the valence electron, to the ion motion, wherein thermal states and coherent states were employed. HF side band spectroscopy is performed upon directly driving the spins with a high frequency field for single ions and for crystals of up to four ions. The investigated ion crystals have a one-dimensional or two-dimensional configuration and a spin-motion coupling has been investigated with the ion crystals being close to a transition between these configurations, where a movement restriction of the ions in a direction overlapping with the magnetic field gradient becomes relatively weak. In particular, 3-ion-crystals on their linear-to-zigzag structural transition have been studied. Additionally, the rich excitation spectrum of vibration modes are observed in a planar crystal comprised of four ions.

Furthermore, this work entails detailed information of the experimental setup and the involved design choices regarding the creation of the magnetic field gradient. The submerged wires carry up to 9 A to create the magnetic field gradient while compensating mutually their magnetic flux density at the position of the ion. Heat production associated with the current is counteracted by water-cooling and monitored by electrical resistance measurements of the wires. To measure the created magnetic field gradient, the remaining magnetic flux density and also to characterise the experimental setup as a whole, measurements with single trapped ions or a pair of trapped ions are presented.

Zusammenfassung

Im Rahmen dieser Arbeit werden das quantenmechanische Verhalten einzelner, gefangener Ionen und von linearen oder planaren Ionenkristallen unter der Einwirkung eines *transversalen* magnetischen Feldgradienten untersucht. Es wird eine planare Paulfalle mit Oberflächenelektroden verwendet, um $^{40}Ca^{+}$ Ionen zu fangen. Unter den Oberflächenelektroden sind stromführende Drähte in die Paulfalle eingebettet, welche eine magnetischen Feldgradienten von bis zu 16,3(9) T/m erzeugen. Dieser Gradient ist in diejenige Richtung ausgerichtet, welche senkrecht zur Achse des schwächsten Einschlusses der Ionen durch die Paulfalle steht und entlang derer sich lineare Ionenkristalle bilden.

In dieser Konfiguration wurden schnelle Rabi-Oszillationen mit t_π=0,55 μs zwischen den Zeeman-Niveaus m=+1/2=$|\uparrow\rangle$ und m=-1/2=$|\downarrow\rangle$ des elektronischen Grundzustands der Ionen getrieben, wobei die hierzu eingestrahlte Hochfrequenz nahe bei 10 MHz liegt und eine Kohärenzzeit bis zu $t_{coh} = 0,5$ ms erreicht wird. Es wird aufgezeigt, dass der magnetische Feldgradient innere Freiheitsgrade der Ionen, insbesondere den Spin des Valenzelektrons, mit der Bewegung der Ionen koppelt, wobei thermische und kohärente Zustände verwendet werden. Es wird Hochfrequenz-Seitenbandspektroskopie, bei welcher die Spins direkt mit einem Hochfrequenzfeld getrieben werden, an einzelnen Ionen und an Kristallen aus bis zu vier Ionen durchgeführt. Die Kristalle weisen eine eindimensionale oder zweidimensionale Konfiguration auf und es wurde die Spin-Bewegung-Kopplung in der Nähe eines Übergangs zwischen diesen Konfigurationen untersucht, bei welchem eine Bewegungseinschränkung der Ionen in eine Richtung, welche mit dem magnetischen Feldgradienten überlappt, relativ schwach wird. Ein besonderes Augenmerk wird auf 3-Ionenkristalle gelegt, welche sich an einem Strukturübergang zwischen einer linearen Konfiguration und einer Zickzackkonfiguration befinden. Darüber hinaus wird das reichhaltige Anregungsspektrum von Schwingungsmoden in einem planaren Kristall, der vier Ionen umfasst, untersucht.

Zusätzlich umfasst diese Arbeit Details zum Versuchsaufbau und zur gewählten Ausgestaltung bezüglich einer Realisierung des magnetischen Feldgradienten. Die eingebetteten Drähte führen Ströme von bis zu 9 A, um den magnetischen Feldgradienten zu erzeugen, während sie das von ihnen erzeugte Magnetfeld am Ort der Ionen gegenseitig kompensieren. Eine aufgrund des Stromfluss entstehende Wärme wird von einer Wasserkühlung abtransportiert und anhand des elektrischen Widerstand der Drähte überwacht. Um den erzeugten magnetischen Feldgradient und das verbleibende Magnetfeld zu messen, sowie um den Gesamtaufbau zu charakterisieren, werden Messungen mit einzelnen Ionen und Ionenpaaren präsentiert.

Contents

Chapter 1

Introduction

1.1 Quantum Computation and Simulation

In our constant struggle to understand the surrounding world, we nowadays rely heavily on numerics and simulations. Since we learned how to outsource routine jobs to machines, their computational power appears to be ever increasing, allowing us to analyse more complex systems with less simplifications.

On an abstract level, a computation is an algorithmic solution to a mathematical problem which needs three resources: space, energy and time [BCS04]. Space is basically needed for memory, energy for the computation process and erasing of information and time for the physical process behind the computation to take place. Nowadays flash drives are commercially available with several gigabyte of volume at the size of a thumbnail, in that sense space is virtually infinite. Energy, although a constant subject to political debate in recent decades, is also far from being a limiting factor to computational power with state of the art technologies. The bottle neck is time. By principle, any computation can be done by a conventional computer which is implemented as a universal Turing machine [Tur37]. However, depending on the size of a system in which a problem is to be solved, the process may take hundreds of years in extreme cases, especially if the necessary number of steps of calculation grow exponentially with the number of constituents of said system. Algorithms for these kind of problems are called *inefficient* in contrast to problems for which the number of steps of calculation grow merely polynomial with the number of constituents. Prominent examples are the salesman problem and the prime factorisation of large numbers. Up to date encryption (e.g. RSA) is based on the fact that there is no known efficient algorithm for the last example.

This is where the concept of quantum computation steps in with the promise to have efficient solutions or at least a major speed up for some problems, for which only inefficient solutions are known so far. Known algorithms using quantum computation are for example Shor's prime factorisation [Sho97] and Grover's search of an item in an unsorted database [Gro97]. Quantum computation was proposed by Feynman [Fey82] for an efficient simulation of a quantum mechanical system and a first framework on this subject was worked out by Benioff [Ben82]. In most general terms quantum computation solves a mathematical problem by exploiting quantum mechanical properties and phenomena like entanglement. The basic computational unit of quantum computation is called a *qubit* in analogy to the classical bit. Any constituent of a system with two distinct (eigen-)states, often denoted by $|0\rangle$ and $|1\rangle$

in analogy to the classical bit, can be used to implement a qubit. Due to the quantum mechanical nature any superposition of these states is possible and a qubit has to be described by a two dimensional vector space in contrast to the classical binary bit. A qubit can be implemented in various ways, some examples are atomic energy levels, the polarisation of a photon or the number of flux quanta in a Josephson junction. A computation is for example carried out by a time development of the qubits under a designed Hamiltonian. This approach is referred to as *circuit based quantum computing*. Other approaches include *measurement based* and *adiabatic quantum computing*. We speak of *quantum simulation*, when we use a quantum system, which is well-known and/or easy to control, to describe another (quantum) system, which is usually more complex. If we can shape and tune the Hamiltonian of the describing quantum system in a way that resembles the described more complex system, we can get insight into the latter, by investigating the first [JVW09].

Whether a given system is suitable to perform quantum computations and simulations, comes down to the following criteria [DiV00]:

- *A scalable physical system with well characterised qubits.* The Hamiltonian governing the qubit's overall dynamics should be known as well as the interaction with other states of the qubit, if present, and the interaction with other qubits as well as the influence of the environment on the qubit. A physical system is scalable with regards to quantum computation when there is neither a fundamental limit to the number of qubits the system can be worked with nor that an exponential increase in technical overhead is necessary to work with an arbitrarily large number of qubits. Scalability is necessary for non trivial computations.

- *The ability to initialise the state of the qubit to a simple fiducial state.* At the start of each calculation the qubits have to be resettable for a reproducible outcome.

- *A universal set of quantum gates.* A gate refers to a manipulation of a state of one or of several qubits, e.g. a logical operation (AND, OR, NOT...). A calculation can be carried out by a specific sequence and repetition of gates. If a set of gates can reproduce any possible state of the total system it is called universal.

- *Long relevant decoherence times, much longer than the gate operation time.* Decoherence is the collective term for any undesired evolution of the qubit's state, due to e.g. interaction with the environment or unstable control parameters. This evolution can corrupt the information stored in the qubits up to complete loss. The ball park figure for the number of gates necessary for any meaningful computation is often stated to be ten to hundreds of thousands.

- *A qubit-specific measurement capability.* After the computation is done the information stored in the qubits has to be read out, which in general requires a qubit specific measurement, that does not disturb other qubits.

1.2 Cold Ions in Paul Traps

One system currently under investigation and making huge progress in the last two decades, uses cold ions confined in linear Paul traps [CZ95]. Traps devised by Paul [Pau90] use a mixture of static and dynamic electrical fields to hold charged particles within a small space. 'Cold' has to be understood as a measure of the ion's movement, which has to be small compared to the distance to the next ion. Thus, the confined particles form a crystalline structure with each particle oscillating around a fixed position within the trap's volume. Due to their simplicity, hydrogen-like ions are usually employed as charged particles, especially singly charged alkaline earth metals. Two levels of the electronic state serve as a qubit, which can be manipulated and read out with electromagnetic radiation at high fidelities [HRB08]. The interaction due to the mutual Coulomb repulsion couples the ions to collective oscillator modes, thus forming a bus system.

Using an electric potential well is an obvious approach to trap a charged particle. However, the electric potential ϕ in a virtually charge-free space obeys the Laplace equation $\Delta\phi = 0$. Thus, the curvatures along all space dimensions cannot have the same sign and the potential is confining the particle in two directions at most. In at least one direction the particle will be accelerated away from the centre of the trap. Therefore, it is not possible to hold a charged particle with only static voltages alone. If one applies an alternating potential, the above stated is still true but with the addendum 'at any time'. If the curvature changes its sign along the direction in which the particle tries to escape, the particle is pushed back towards the centre of the trap instead, see fig. 1.1. Somewhat like balancing a marble on a plate. If a frequency of the alternating potential is tuned to a mass-charge-ratio of the particle, the particle will execute oscillations, which are at least approximately harmonic, within a confined volume of space.

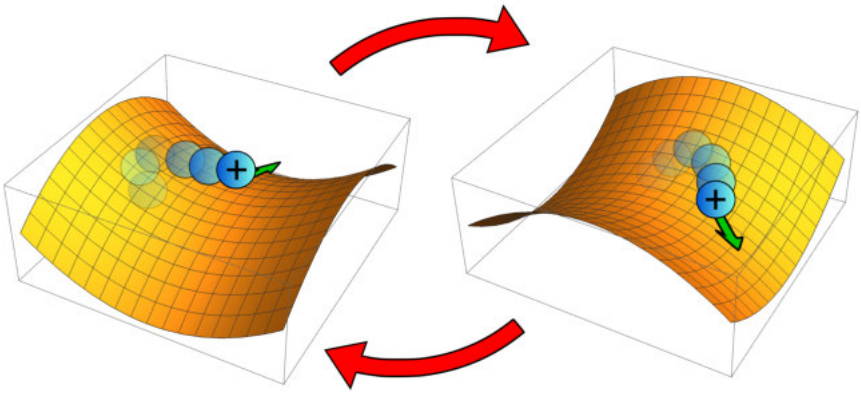

Figure 1.1: *Trapping principle of a Paul trap.*

A linear Paul trap works with a quadrupole field, created by four rods, as seen in fig. 1.2, a). The ion is confined in the plane perpendicular to the rods, referred to as the *radial* directions. Along the rods, called the *trap axis*, two additional electrodes create a static potential well to keep the ion from escaping. For the charge-to-mass ratio of a single ion, the dynamic part of the potential needs change rates in the radio frequency (RF) regime. Excessive motion accumulating over time can be counteracted by laser cooling, allowing to trap an ion for hours and even days.

If the RF-ground rods are segmented, as shown in sub-fig. b), where each segment can be addressed individually, the potential along the trap axis can be shaped and changed at will. The limits are given by the distance to the trap centre, the width of a single segment and the precision of the DC power supply. In a properly designed trap the controlled transport of ions [Rus+14] between different regions of the trap is possible, e.g. a transport between a storage zone and a processing zone [Lak+15]. For the trap to work under optimal conditions however, the different parts have to be

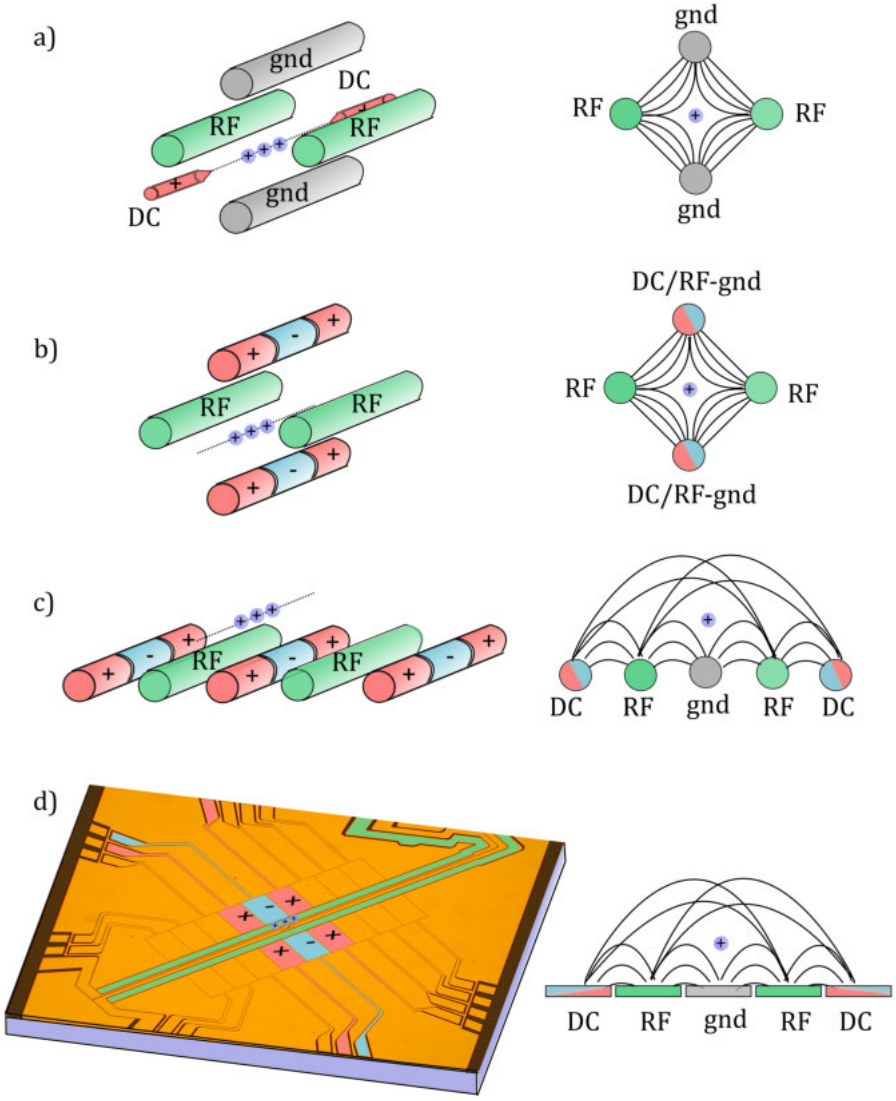

Figure 1.2: *Setup of different Paul traps: a) linear trap with separate electrodes for RF and DC voltages b) linear segmented trap with an integration of the DC electrodes into the RF-ground electrodes c) idea of a surface trap by 'unfolding' a linear segmented trap, wherein in a five wire realisation, one of the RF-ground electrodes was split/doubled d) real surface trap implemented as microchip*

aligned very carefully. Furthermore, including regions with different trap parameters is also a challenge. Therefore, a modification of the trap was proposed [Chi+05], where the rods are dragged into a single plane. Sub-fig. c) shows a model of the so-called *five-wire* realisation. The quadrupole field becomes distorted on a large scale but remains confining at a certain point above the newly formed surface, although

with a potential wall, which is an order of magnitude smaller than before. With such an arrangement of the electrodes the trap can be realised as a microchip and well established techniques like photo lithography for its production can be used. Thus, allowing the easy realisation of arbitrarily complex designs. $\mathbf{x_0}$

In this work, the used Paul trap was designed to confine $^{40}Ca^+$ ions [BS15]. To see how this system fulfils the criteria stated above, we look at the electronic energy level diagram of $^{40}Ca^+$ ions, depicted in fig. 1.3. A $^{40}Ca^+$ ion has one valence electron and the electronic ground state $4S_{1/2}$ has spin 1/2. By employing an external magnetic field to lift degeneracy, the qubit can be encoded in the Zeeman sub-levels of the ground state, i.e. (m=+1/2)≡ $|\uparrow\rangle$ and (m=-1/2)≡ $|\downarrow\rangle$. It can be initialised, i.e. a population of the ground state sub-levels can be shifted to either of the Zeeman sub-levels, by circular polarised laser light at 397 nm and/or by optical pumping of one of the Zeeman sub-levels to a sub-level of the metastable state $3D_{5/2}$ and re-pumping. For the readout, the population of the $|\downarrow\rangle$ level is shelved to the metastable state $3D_{5/2}$. The population remaining in the $4S_{1/2}$ level is excited to the short lived $4P_{1/2}$ level and the fluorescence at 397 nm from spontaneous emission can be detected [Pos+09]. Since the ions float midway in the vacuum, they are greatly decoupled from the environment, opposed to e.g. solid state approaches.

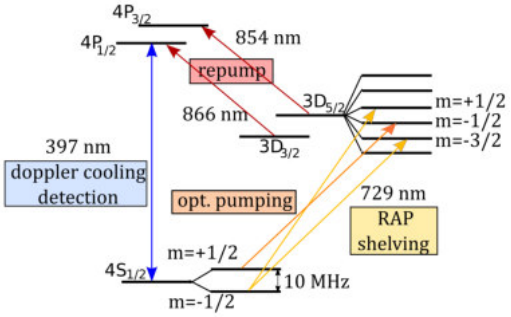

Figure 1.3: *Energy levels of* $^{40}Ca^+$

It can be shown that a controlled NOT gate and single qubit gate are a universal set of quantum gates, c.f. [BCS04, sec. 3.5]. Both have been realised with high fidelities [Lei+03a] using precisely timed laser pulses to drive Rabi oscillations. While the control of the constituents, i.e. the confined ions, of this system is great, the challenge is scalability.The entanglement of up to 14 ions has been demonstrated [Mon+11]. Furthermore, schemes for robust gates in the presence of excessive micro motion have been proposed [Wan15]. Recently, stable trapping and cooling of crystals comprising more than 100 ions [Kie+23] have been demonstrated. Nonetheless, thousands and more qubits would be necessary for a meaningful task. Additionally, focused laser beams are necessary to avoid cross-talk between different ions during gate operations, while at the same time the inter-ion distance will drop with larger crystals. Here, the use of magnetic field gradients promises a reduction in technical complexity [MW01; CLJ08; Wei+16].

1.3 Magnetic Field Gradients

The application of a magnetic field gradient to the ions allows the use of atomic transitions in the RF and microwave regime [MW01]. Thus, a commercial microwave horn and a signal generator could replace the more complex laser systems to manipulate the qubit's state. At the same time one gains higher frequency and amplitude stability, thereby simplifying the whole setup.

The interaction strength between an electromagnetic wave with wave vector k and an ion of mass m, which is trapped in a harmonic potential well with an angular

frequency ω_t, can be characterised by the Lamb-Dicke factor:

$$\eta = \sqrt{\frac{\hbar^2 k^2}{2m} \frac{1}{\hbar\omega_t}} \tag{1.1}$$

It compares the change in the kinetic energy of the ion upon emitting or absorbing a photon with the energy spacing between the levels of the harmonic potential well. It is therefore a criterion whether the ion will also change its movement when its internal state is changed. For $^{40}Ca^+$ ions Paul traps are used that typically show a trapping frequency ω_t in the few MHz regime. If a flip between the internal states is done by a magnetic dipole transition in the high frequency (HF) range, the above equation yields $\eta \approx 10^{-9}$, which in turn gives rise to a spin-motion coupling strength of $\eta\Omega/\pi \approx 10$ mHz. Compared to the demonstrated coherence time of up to 2 s [Rus+16] of qubits in such a system, the coupling is obviously too weak to be harnessed for quantum simulations.

Applying a magnetic field gradient to the system however, changes the game completely by making the atomic transition energy $\hbar\omega_a$ of the magnetic dipole transition between the internal states dependent of a position x of the trapped ion along the magnetic field gradient. Thereby, the ion receives an additional impulse each time it changes its internal state, see fig. 1.4.

This can be described with the same formalism as the 'regular' interaction without gradient, but with an *effective* Lamb-Dicke factor [Wun02]

$$\tilde{\eta} \approx \frac{\partial\omega_a}{\partial x} \frac{x_0}{\omega_t}, \tag{1.2}$$

where x_0 is the spatial extent of the ion's wave packet in the ground state of the harmonic potential. Thus, $\tilde{\eta}$ can be tuned to any value, if one can supply a high enough spatial derivation of the atomic transition energy. For a magnetic dipole transition this could be achieved by a magnetic field gradient at the order of magnitude of 10^0 to 10^2 T/m.

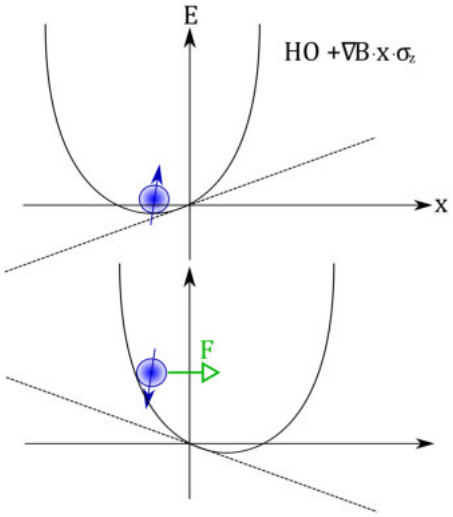

Figure 1.4: *With a magnetic field gradient, the ion will receive a momentum kick upon flipping its internal state. Modified from [JVW09].*

The arise of an interaction with an effective Lamb-Dicke factor was used to individually address ions in a chain [Joh+09] with low cross-talk [Pil+14] by applying the gradient along the chain axis. Thereby, each ion has a different Zeeman splitting. Furthermore, the realisation of a CNOT gate [Khr+12] as well as a robust controlled phase gate [Bar+22] was shown. Furthermore, magnetic side band cooling of an ion to the ground state [Wei+15] has been demonstrated, as well as Schemes using oscillating [Osp+11; Har+16] or static [Wei+16] magnetic field gradients to induce coupled dynamics. To achieve high gradients, approaches with permanent magnets [Khr+12; Lak+15; Kaw+17] or with currents [Wan+09; Kun+14] have been investigated. In particular, two-qubit gates to fully entangle qubits with high

fidelity have been proposed by using a static magnetic field gradient [Val+21] and demonstrated by using an RF magnetic field gradient [Zar+19; Sri+21].

For a chain of ions, this spin-motion coupling also mediates a J-type spin-spin coupling. If the spin of one ion is flipped, it gets a kick. Due to the mutual Coulomb repulsion between the ions, the neighbouring ions will change their movement as well. In their rest frame this is the same as a changing magnetic field, which in turn can induce a spin flip. Thus, allowing the realisation of spin-models, like the (transverse) Ising model [Kim+10; Lan+11] or XY-model. Similar studies have also been made by employing a Penning trap instead of Paul trap [Bri+12]. The collective motion can also be seen as a boson bath, opening a rich playground for the investigation of spin-boson models [WSNR17; Por+08]. These models are relevant to our understanding of quantum magnetism [Jur+14; Isl+13], for studies of non-linear dynamics [Ges+14; Lem+15] and quantum phase transitions [JVW09]. Simulating phase transitions in interacting linear spin systems [Zha+17; Jur+17] have been demonstrated. Linear to two-dimensional self-assembled spin arrays [Ber+11; ZCH23] or even fully controlled geometries of interacting spins [Kum+11; Mie+16; Kum+16] opens up investigations of interesting quantum phases in systems with frustrated interactions.

1.4 How This Work Fits In

In this work, a magnetic field gradient transverse to the trap axis was employed. It is generated by three current carrying wires, that are situated beneath the trap chip. This way, the metal surface of the trap shields the ion from an electrical field of the wires. In a previous setup, the magnetic field gradient was created by a wire that was integrated in the surface of the chip [BS15]. This led to the excitation of various non-linear resonances [Alh+96]. In a segmented Paul trap, ions can be moved inside the external magnetic field with high precision. Thereby, the ion was used as a probe for the magnetic field and its gradient by observing frequency shifts in the ion's atomic transitions as a function of the ion's position [Wal+11]. A magnetic field gradient of 16.3(9) T/m was achieved in the radial plane perpendicular to the trap axis, generating a homogeneous spin-motion coupling for all ions in a chain. HF side band spectroscopy of the transition between the Zeeman sub-levels of the $^{40}Ca^{+}$ ground state $4S_{1/2}$ was established. I investigated the side bands for a single ion, a chain of ions and a planar crystal, which can be used as a basis for a future implementation of spin-models and the investigation of frustration effects [Qia+22]. The major results of this work were published as "Spin and motion dynamics with zigzag ion crystals in transverse magnetic field gradients" in *J. Phys. B: At. Mol. Opt. Phys.* 52 (2019) p. 025301 by J. Welzel, F. Stopp and F. Schmidt-Kaler.

This work is organised as follows: In chapter 2, mechanics of Paul traps are described and the interaction between an atom and an electromagnetic field is recapitulated briefly. In chapter 3, the physical implementation in the laboratory as well as the electronic and optical setup is presented. The main part consists of two chapters: In chapter 4 some aspects of the performance of the experimental apparatus are characterised. In chapter 5, results from HF sideband spectroscopy are discussed for a single ion and for 2-, 3- and 4-ion crystals in linear and planar configuration. Finally, in chapter 6 the results are summarised and future improvements are discussed.

Chapter 2

Theoretical Foundations

A trapped ion interacting with an incidental electromagnetic wave, is described by a Hamiltonian

$$H = H_m + H_e + H_i \tag{2.1}$$

with the first term representing the motion of the ions within the trap, which is discussed in the first section of this chapter. The second term describes the inner electronic state of the ion. The last term denotes the interaction between the ion and the electromagnetic wave, which is covered in section 2.2. As briefly touched in the last chapter, a strong coupling of internal states of the ion with a movement of the ion inside the trap can be implemented by using magnetic field gradients, which is the topic of the successiv section. Finally, possibilities are discussed to include a magnetic field gradient into a Paul trap.

2.1 Ions in Planar Paul Traps

The movement of particles of charge Ze, where e is the elementary charge and Z an integer, within the electrical potential ϕ_{trap} of a Paul trap is governed by the Hamiltonian $H_m = T + V$, with the kinetic energy T and the potential $V = Ze\phi_{\text{trap}} + Ze\phi_{\text{ion}}$. The term ϕ_{ion} describes the mutual Coulomb interaction of the particles with each other. In a first subsection, the trap potential ϕ_{trap} of Paul traps and its effect on a single ion is reviewed. In a second subsection, the specific form of the trap potential is discussed in more detail for planar Paul traps. In a third subsection the effects of ϕ_{ion} are investigated. Finally, there will be a brief overview of the most important motional states in context of this work.

2.1.1 Trapping Potential of Paul Traps

This and the following subsection follow in large parts the description given in [Hou08]. An ion of mass m trapped within the potential well of a Paul trap will move around an equilibrium position $\mathbf{x_0}$ with the displacement $\mathbf{x}$. The classical equation of movement is given by

$$\ddot{\mathbf{x}} = -\frac{Ze}{m}\nabla\phi_{\text{trap}} \tag{2.2}$$

The potential of a Paul trap can be separated into a static part (ϕ_{DC}) and a time-dependent part ($\phi_{RF}\cos(\Omega t)$) oscillating at an angular drive frequency Ω of the

trap. If both parts of the trapping potential have a minimum that coincides with the equilibrium position, the leading term in a Taylor expansion around $\mathbf{x_0}$ is:

$$\phi_{\text{trap}}(\mathbf{x},t) = \frac{1}{2}\sum_{i,j=1}^{N}\left(\frac{\partial^2\phi_{\text{DC}}}{\partial x_i \partial x_j}\right)_{\mathbf{x}_0} x_i x_j + \frac{1}{2}\cos(\Omega t)\sum_{i,j=1}^{N}\left(\frac{\partial^2\phi_{\text{RF}}}{\partial x_i \partial x_j}\right)_{\mathbf{x}_0} x_i x_j \tag{2.3}$$

With the definition of the time parameter $\tau = \Omega t/2$ and the matrices A and Q, which are defined entry-wise by

$$A_{ij} = \frac{4Ze}{m\Omega^2}\left(\frac{\partial^2\phi_{DC}}{\partial x_i \partial x_j}\right)_{\mathbf{x}_0} \text{ and } Q_{ij} = \frac{2Ze}{m\Omega^2}\left(\frac{\partial^2\phi_{RF}}{\partial x_i \partial x_j}\right)_{\mathbf{x}_0} \tag{2.4}$$

eq. (2.2) reads:

$$\ddot{\mathbf{x}} + (A + 2Q\cos(2\tau))\,\mathbf{x} = 0 \tag{2.5}$$

This is a Mathieu differential equation and the Floquet theory shows that the solutions are of the form:

$$\mathbf{x} = \mathrm{e}^{\imath\beta_i\tau}\mathbf{b}_i(\tau) \tag{2.6}$$

with a π-periodic amplitude $\mathbf{b}_i(\tau)$ and a characteristic exponent β_i, which in general has to be found numerically. The solutions always come as pairs with $\beta_j = -\beta_i$. Therefore, if one of the solutions has a non-vanishing imaginary part, there is a solution that will grow exponentially in time and the motion of the ion in the trap is unstable. Otherwise, if β_i has only a real part, eq. (2.6) represents a sinusoidal oscillation at angular frequency

$$\omega_i = \beta_i\Omega/2, \tag{2.7}$$

called the secular motion, see fig. 2.1. If all β_i are real, the trap is stable and the ion will be confined around $\mathbf{x_0}$.

A Fourier expansion of $\mathbf{b}(\tau)$ yields $\mathbf{x} = \mathrm{e}^{\imath\beta_i\tau}\sum_{n=-\infty}^{\infty}\mathbf{b}_n\mathrm{e}^{\imath 2n\tau}$. While $\mathbf{b}_0$ depicts amplitude and direction of the secular motion, higher terms are called micro motion and have usually a smaller amplitude. Putting this expression into eq. (2.5) yields a recursive formula for the $\mathbf{b}_n$. Rearranging and repeated application of this formula yields a relation between the characteristic exponent β and the matrix entries given in eq. (2.4), if one can neglect higher $\mathbf{b}_n$. If the trap axes of the trapping potential are collinear with the axes of the trap chip implementing the Paul trap, i.e. $A_{i,j} \ll A_{i,i}$ and $Q_{i,j} \ll Q_{i,i}$ for $i \neq j$, the characteristic exponent is then approximately given by

$$\beta_i^2 \approx A_{i,i} + \frac{Q_{i,i}^2}{2}. \tag{2.8}$$

Note also, that the trace of A and Q has to vanish. For linear Paul traps, with a symmetry axis in the z-direction $Q_{z,z} \approx 0$ and therefore $Q_{x,x} = -Q_{y,y}$. Furthermore, $A_{z,z} > 0$ for trapping positively charged ions and $A_{x,z},\ A_{y,z} \approx 0$.

In the case that $|\mathbf{b}_0| \gg |\mathbf{b}_{\pm1}| \gg |\mathbf{b}_{\pm2}|$ the dynamics can be approximated by the secular motion with a pseudo potential energy:

$$E_p = \frac{Z^2e^2}{4m\Omega^2}|\nabla\phi_{\text{RF}}|^2 \tag{2.9}$$

For some time-critical applications [Ulm+13; Kau+12], the pseudo-potential approximation will yield inferior results and the full dynamic of the RF drive [Lei+03b] has to be considered.

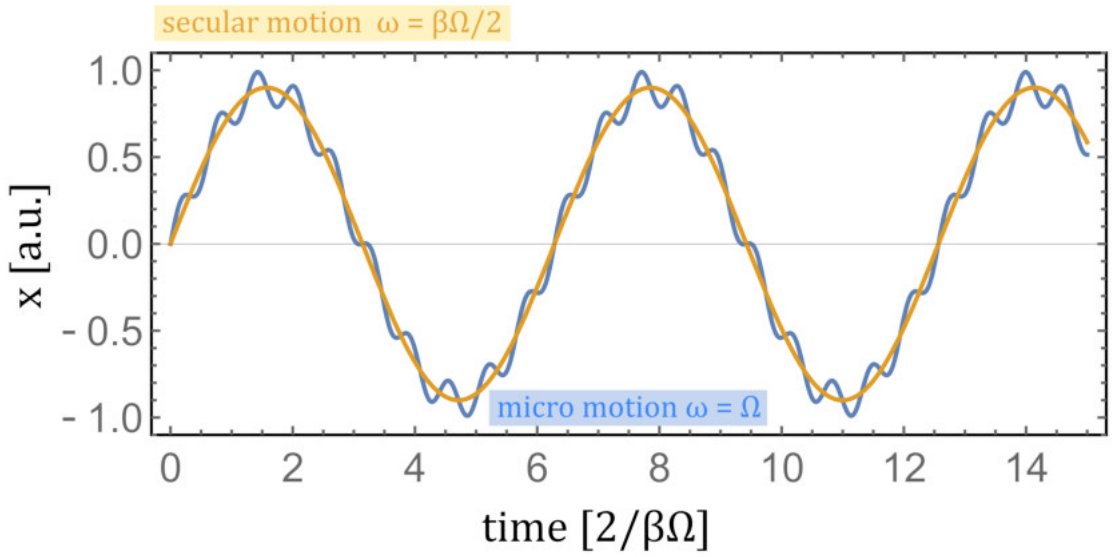

Figure 2.1: *Visualisation of the ion's motion in a Paul trap. The ion oscillates with a secular frequency (orange) according to eq. (2.7). The secular motion may be superimposed with micro motion (blue) with a higher frequency. Micro motion is especially excited, if the ion is not situated in the node of the RF potential.*

2.1.2 Trapping Potential of Planar Paul Traps

The trapping potential in our case is created by thin rectangular, conducting electrodes E_n, which are all arranged in the same plane $y = 0$. The electrodes are each held at a homogeneous voltage V_n. If the opposite corners of electrode n have the coordinates $(x_1, 0, z_1)$ and $(x_2, 0, z_2)$ and the rest of the plane $y = 0$ is grounded, the Laplace equation for the potential of this electrode above the plane $y = 0$ can be solved analytically:

$$\begin{aligned}\phi_n(\mathbf{x}) = \frac{V_n}{2\pi}\Bigg[&\arctan\left(\frac{(x_2-x)(z_2-z)}{y\sqrt{y^2+(x_2-x)^2+(z_2-z)^2}}\right)\\ &-\arctan\left(\frac{(x_1-x)(z_2-z)}{y\sqrt{y^2+(x_1-x)^2+(z_2-z)^2}}\right)\\ &-\arctan\left(\frac{(x_2-x)(z_1-z)}{y\sqrt{y^2+(x_2-x)^2+(z_1-z)^2}}\right)\\ &+\arctan\left(\frac{(x_1-x)(z_1-z)}{y\sqrt{y^2+(x_1-x)^2+(z_1-z)^2}}\right)\Bigg]\end{aligned} \tag{2.10}$$

The trapping potential is then the sum of the potentials of all the electrodes $\phi_{\mathrm{trap}} = \sum^{n_{DC}} \phi_n + \cos(\Omega t) \sum^{n_{RF}} \phi_n$.

In a five wire design of the trap chip as shown in fig. 2.2. There is a first RF electrode with a width a, a second RF electrode with width c separated from the first RF electrode by an RF-ground electrode of width b, wherein the width is measured in the x-direction.

With this layout the ion will be trapped around a local minimum of ϕ_{RF}, which is located approximately[1] at:

$$x_0 = \frac{ab}{a+c},\ y_0 = \frac{\sqrt{abc(a+b+c)}}{a+c}, \tag{2.11}$$

wherein $x = 0$ is at the centre between the first RF electrode and the RF-ground electrode. Note, the ideal trap position is solely dependent on the geometry of the trap electrodes and not e.g. the applied voltage. Shifting the ion out of this RF node with additional static voltages will increase the amplitude of the micro motion. From here on, we will use the notation of $z-$, *axial*-direction and *trap axis* synonymously. Likewise, the *lateral position* refers to the x-coordinate and *height* refers to the y-coordinate. For any direction perpendicular to the trap axis, in particular either of x or y, we may use the term *radial*. The depth of the potential well can be estimated by a saddle point in the pseudo potential before its dropping to zero as one moves away from the surface, see fig. 2.3. The saddle point is the point where the ion can escape from the trap with the lowest energy.

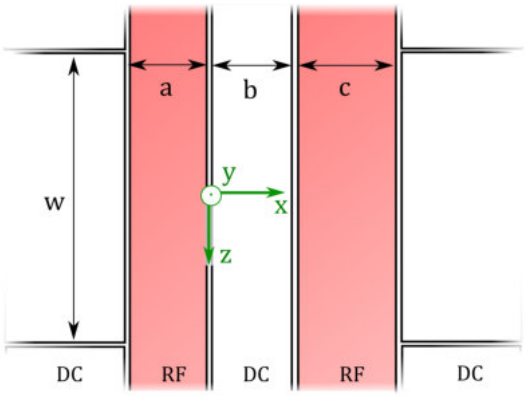

Figure 2.2: *Schematics of the relevant dimensions of the trap electrodes. In the trap used for experiments* $w = 430$ µm, $a = 100$ µm, $b = 100$ µm *and* $c = 120$ µm.

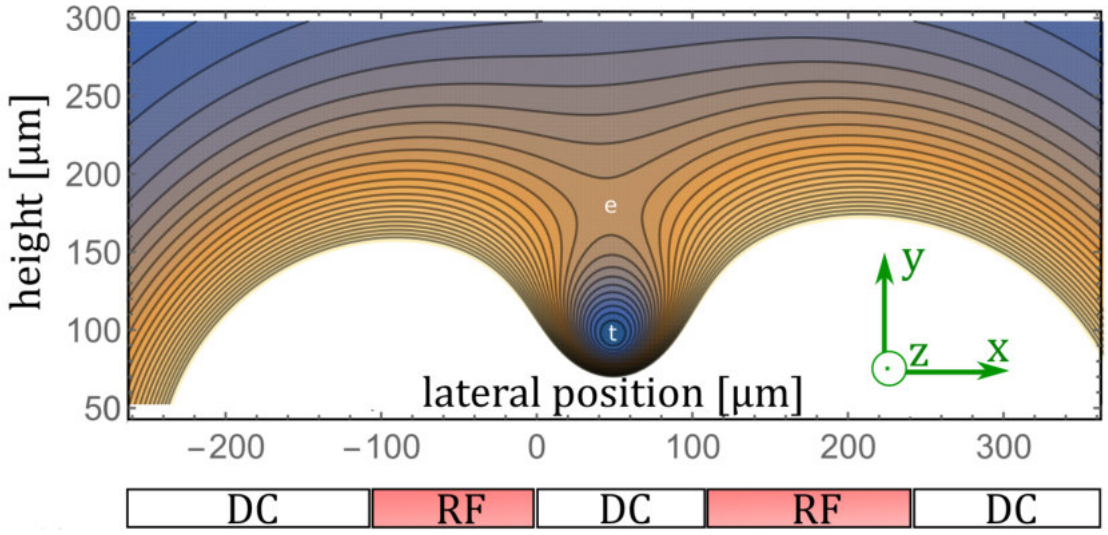

Figure 2.3: *Pseudo potential of a trap geometry that was used in this work according to eq. (2.9). Blue represents a relative low value and yellow a relative high value of the pseudo potential.* ***t*** *is marking the trapping centre and* ***e*** *the escape point. The radial principle axes of the trap centre are slightly rotated around the axial direction, due to the different widths of the RF electrodes.*

[1] for in the z-direction infinitely long RF electrodes

With eq. (2.10) the potential can be calculated for given voltages. The voltage of the RF electrode is fixed in our setup. However, the voltage of the DC electrodes can be chosen at will. Therefore, the inverse problem of eq. (2.10) is of greater interest in day-to-day work, i.e., which DC voltages are necessary to achieve a given DC potential, which will yield a specific trap frequency in particular along the trap axis without moving the ion out of the minimum of the RF potential? For this, one can employ the method of Lagrange multipliers λ. From a technical point of view, to avoid arbitrary high voltages, it is useful to minimise the function

$$f = \sum_{i=1}^{N} V_n^2, \tag{2.12}$$

where N is the number of available DC electrodes. The constraints c_i can be summarised as:

$$\begin{pmatrix} c_1 \\ c_2 \\ c_3 \end{pmatrix} = \sum_{i=1}^{N} V_n \nabla \phi_n \Big|_{\mathbf{x}_0} = \mathbf{0} \tag{2.13}$$

$$c_4 = \sum_{i=1}^{N} V_n \frac{\partial^2 \phi_n}{\partial z^2}\Big|_{\mathbf{x}_0} - \frac{m\Omega^2}{4Ze} A_{zz} = 0, \tag{2.14}$$

where ϕ_n is the potential of the n^{th} electrode with unit voltage applied. The first equation nullifies the electric field at the trap centre and minimises the micro motion. The second equation stipulates the curvature along the trap axis. Differentiation of $L = f + \sum^4 \lambda_i c_i$ with respect to the V_n and λ_i yields $N + 4$ linear equations, that can be restated to the form of a matrix equation:

$$\begin{pmatrix} 2 & 0 & \cdots & 0 & \frac{\partial L/\partial V_1}{\lambda_1} & \cdots & \frac{\partial L/\partial V_1}{\lambda_4} \\ 0 & 2 & \cdots & 0 & \frac{\partial L/\partial V_2}{\lambda_1} & \cdots & \frac{\partial L/\partial V_2}{\lambda_4} \\ \vdots & \vdots & & \vdots & \vdots & & \vdots \\ 0 & 0 & \cdots & 2 & \frac{\partial L/\partial V_N}{\lambda_1} & \cdots & \frac{\partial L/\partial V_N}{\lambda_4} \\ \frac{c_1}{V_1} & \frac{c_1}{V_2} & \cdots & \frac{c_1}{V_N} & \frac{c_1}{\lambda_1} & \cdots & \frac{c_1}{\lambda_4} \\ \vdots & \vdots & & \vdots & \vdots & & \vdots \\ \frac{c_4}{V_1} & \frac{c_4}{V_2} & \cdots & \frac{c_4}{V_N} & \frac{c_4}{\lambda_1} & \cdots & \frac{c_4}{\lambda_4} \end{pmatrix} \cdot \begin{pmatrix} V_1 \\ V_2 \\ \vdots \\ V_N \\ \lambda_1 \\ \vdots \\ \lambda_4 \end{pmatrix} = \mathbf{0} \tag{2.15}$$

This equation was solved using the C++ library *Eigen*, integrated into the experimental control software. Thus, allowing a quick change of trap frequencies by calculating and setting a set of DC voltages automatically, which yield a given curvature A_{zz} of the trap potential in axial direction.

2.1.3 Ion Crystals

If N ions are trapped and their kinetic energy is low enough, they will crystallise. That is, each ion will only move around a fixed equilibrium position $\mathbf{x}_n^{(0)}$, given by:

$$\frac{\partial V}{\partial \mathbf{x}_n}\Big|_{\mathbf{x}_n^{(0)}} = 0 \tag{2.16}$$

With a harmonic approximation of the trapping potential and the electric constant ϵ_0, we can write:

$$V = \sum_{i=0}^{2}\sum_{n=1}^{N}\frac{1}{2}m\omega_i^2 x_{i,n}^2 + \frac{e^2}{8\pi\epsilon_0}\sum_{\substack{n,m=1\\ n\neq m}}^{N}\frac{1}{|\mathbf{x}_n - \mathbf{x}_m|}, \tag{2.17}$$

wherein the angular frequencies ω_i are given by eq. (2.7). If $\omega_x,\ \omega_y \gg \omega_z$ the ions will form a linear, virtually one dimensional chain along the z-axis. Usually, the exact positions have to be found numerically [Jam98]. Due to the mutual Coulomb repulsion of the ions, they form a system of coupled oscillators with $3N$ degrees of freedom. The dynamics of such a system can be described by $3N$ normal modes Q_f [Fli09, ch. 25]. A displacement $q_{iN+n} = (\mathbf{x}_n)_i - (\mathbf{x}_n^{(0)})_i$ from the equilibrium position of the n^{th} ion in the i^{th} direction can than be expressed by $q_g = \sum_{f=1}^{3N} S_{fg}Q_f$. The entries S_{fg} constitute a matrix that diagonalises the potential expanded around the equilibrium position $V \approx \frac{1}{2}\sum_{i,j=1}^{3N}\left(\frac{\partial^2 V}{\partial x_i \partial x_j}\right)_{\mathbf{x}^{(0)}} q_i q_j = \frac{m\omega_z^2}{2}\sum_{i,j} M_{i,j}q_i q_j$. The Matrix M evaluates to [Wel+11]:

$$\begin{aligned} M_{jN+o,kN+p} &= \frac{\delta_{jk}\delta_{op}}{\alpha_j} + \frac{l^3}{2}\sum_{n\neq m}(\delta_{on}-\delta_{om})(\delta_{np}-\delta_{mp})\times \\ &\quad \times\left[\frac{3(x_{n,k}^{(0)} - x_{m,k}^{(0)})(x_{n,j}^{(0)} - x_{m,j}^{(0)})}{|\mathbf{x}_n^{(0)} - \mathbf{x}_m^{(0)}|^5} - \frac{\delta_{kj}}{|\mathbf{x}_n^{(0)} - \mathbf{x}_m^{(0)}|^3}\right], \end{aligned}$$

with o and p denoting the number of the ions and j and k denoting the spatial direction, wherein δ_{jk} is the Kronecker delta symbol and wherein several factors can be summarised to a scaling factor $l^3 = q^2/4\pi\epsilon_0 m\omega_z^2$. The parameter $\alpha_i = (\omega_z/\omega_i)^2$ is called the anisotropy of the trap. If μ_i denotes the eigenvalues of the matrix M, the angular frequencies of the normal modes are given by $\sqrt{\mu_i}\omega_z$.

For a linear string of ions along the z-axis the Matrix M reduces to a block diagonal matrix [Enz+00; Jam98] with entries $(\mathcal{B}^x, \mathcal{B}^y, \mathcal{A})$ where

$$\mathcal{A}_{n,m} = \begin{cases} 1 + 2\sum_{\substack{p=1\\ p\neq m}}^{N}\frac{l^3}{|z_m^{(0)} - z_p^{(0)}|^3} & \text{if } n = m \\ \frac{-2l^3}{|z_m^{(0)} - z_n^{(0)}|^3} & \text{if } n \neq m \end{cases} \tag{2.18}$$

$$\mathcal{B}^i_{n,m} = \left(\frac{1}{\alpha_i} + \frac{1}{2}\right)\delta_{nm} - \frac{1}{2}\mathcal{A}_{nm}, \tag{2.19}$$

wherein $i = x$ or y. The matrix $\mathcal{A}$ governs the normal modes in the axial direction and the matrices $\mathcal{B}^x, \mathcal{B}^y$ govern the normal modes in the radial directions. As one can see, all the matrices $\mathcal{A}$ and $\mathcal{B}^i$ share the same eigenvectors, but have generally different eigenvalues. If a_j is the j^{th} eigenvalues of the axial Matrix $\mathcal{A}$, the eigenfrequencies of the radial modes can be expressed as $\omega_{i,j} = \omega_z\sqrt{1/\alpha_i + 1/2 - a_j/2}$. Thus, a critical value of α_i arises, for which one mode of the radial oscillation has zero frequency:

$$\alpha_{crit} = \frac{2}{\bar{a} - 1}, \tag{2.20}$$

where $\bar{a}$ is the biggest eigenvalue of $\mathcal{A}$. In this case a structural transition takes place: first to a planar crystal in a zigzag configuration on to a three dimensional

helix [BKH92; Fis+08; Kau+12]. Since $\bar{a}$ usually has to be found numerically, it is convenient to use a simple model [Enz+00], predicting $\alpha_{\text{crit}} = 2.94N^{-1.80}$ for the beginning of the transition from a linear to a zigzag crystal. In fig. 2.4 different configurations for a ten-ion crystal are shown.

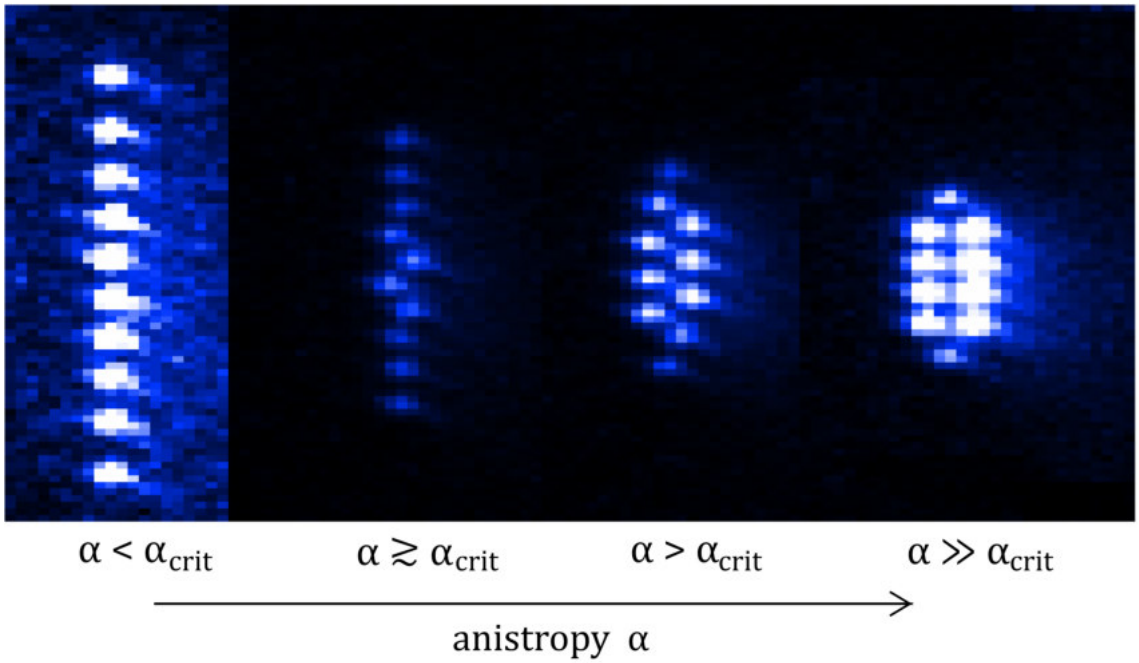

Figure 2.4: *Camera pictures of the structural transition of a ten-ion crystal due to an increasing anisotropy parameter of the trap frequencies from a linear configuration (left) to a zigzag configuration (middle) to a symmetric planar crystal (right). Usually, the anisotropy parameter is much smaller than 1, such that an orientation of the crystal along the trap axis is predominant in all shown configurations. Thus, an increasing anisotropy parameter means, that the axial confinement of the ions and one of the radial confinements get closer together.*

2.1.4 Motional State

To describe the motional state of the ions inside the trap potential, the formalism of Fock states can be employed. In a Fock state $\psi_{fock} = |n\rangle$ the probability to measure n phonons is one and to measure any other number is zero. An arbitrary motional state can be denoted in this basis as $\psi_{motion} = \sum_n \sqrt{p_n}\,|n\rangle$, where p_n is the probability to find n phonons. The following two cases are of particular interest in this work, both are illustrated in fig. 2.5:

Thermal State

Several processes, like fluctuating supply voltages, can excite the motional modes. To counteract this the ions are laser cooled, c.f. sec. 2.2.2, which leads to a thermal equilibrium at temperature T. In this thermal equilibrium a mode shows a mean phonon number $\bar{n} = (\frac{\hbar\omega_t}{k_B T} - 1)^{-1}$, with the Boltzmann constant k_B. The probability

to find n phonons is then given by [Fox06]:

$$p_n = \frac{\bar{n}^n}{(\bar{n}+1)^{n+1}}, \tag{2.21}$$

with a variance of $\mathrm{Var}(n) = \bar{n}^2 + \bar{n}$.

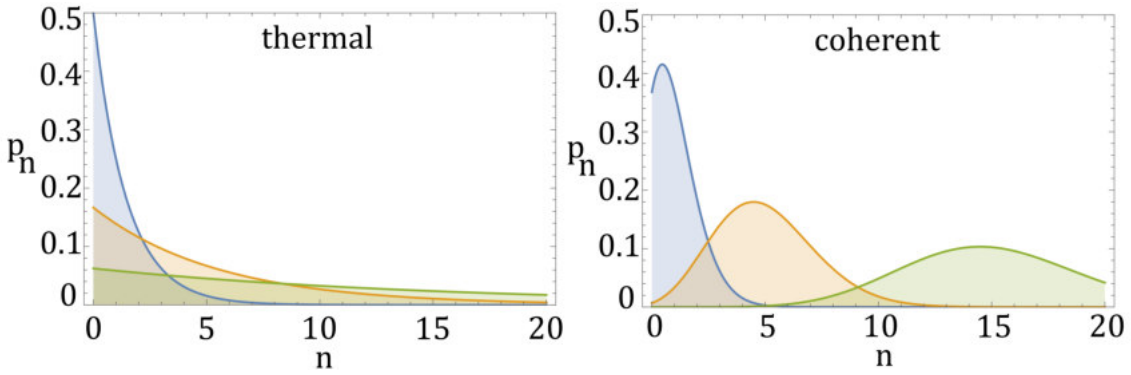

Figure 2.5: *Phonon distribution of thermal and coherent state with a mean phonon number $\bar{n} = 1$ (blue), 5 (red) and 15 (green)*

Coherent State

A coherent state is characterised by a complex number κ and can be written as: $|\kappa\rangle = \exp[\kappa a^\dagger - \kappa^* a]\,|0\rangle$, where $a, a^\dagger$ are the ladder operators of the harmonic oscillator. This describes a displacement of the vacuum state in phase space and is often called a minimum uncertainty state. The probability of detecting n phonons is given by the Poisson distribution:

$$p_n = |\,\langle n\,|\kappa\rangle\,|^2 = \mathrm{e}^{-\bar{n}}\frac{\bar{n}^n}{n!} \tag{2.22}$$

Thus, the mean phonon number $\bar{n} = |\kappa|^2$ equals the distribution's variance.

2.2 Basic Ion-Light Interaction

The transition between two energy levels $E_1 < E_2$ of an atom can take place upon emission or absorption of a photon of energy $\hbar\omega_a = E_2 - E_1$. From a classical point of view, a time dependent electromagnetic field induces dipole oscillations in the atom, which in turn emits a photon of the same frequency. This is a resonance process, i.e. the closer the field frequency is to the atomic transition frequency, the stronger the oscillations. On the other hand the further the frequencies are apart, the weaker the oscillations will be. So if the atom at hand has no other transitions with similar frequencies, we can say that it has only two relevant levels. Ignoring all other levels and transition is called the *two level approximation* for the atom. The dynamics within an external harmonic potential with angular frequency ω_t is then governed by

$$H_0 = \hbar\omega_t\left(a^\dagger a + \frac{1}{2}\right) + \frac{\hbar\omega_a}{2}\sigma_z, \tag{2.23}$$

where $\sigma_z = |\uparrow\rangle\langle\uparrow| - |\downarrow\rangle\langle\downarrow|$ and a, $a^\dagger$ are the bosonic ladder operators.

The interaction with an electromagnetic field

$$\boldsymbol{F}(t) = A\boldsymbol{\epsilon}\cos[\boldsymbol{k}\cdot\boldsymbol{x} - \omega_f t + \phi] \tag{2.24}$$

with an angular frequency ω_f close to ω_a, amplitude A, polarisation $\boldsymbol{\epsilon}$, wave vector $\mathbf{k}$ and phase ϕ will give rise to an additional term, such that $H = H_0 + H_1(t)$, wherein

$$H_1 = \frac{\hbar\Omega_0}{2}(\sigma^{(+)} + \sigma^{(-)})(\mathrm{e}^{\imath\eta(a^\dagger + a) - \imath\omega_f t + \imath\phi} + \mathrm{e}^{-\imath\eta(a^\dagger + a) + \imath\omega_f t - \imath\phi}), \tag{2.25}$$

where $\sigma^{(+)} = |\uparrow\rangle\langle\downarrow|$, $\sigma^{(-)} = |\downarrow\rangle\langle\uparrow|$ are the atomic ladder operators. Amplitude and polarisation are merged into Ω_0, called the Rabi frequency denoting the coupling strength, for details see section 2.2.1. The Lamb-Dicke factor

$$\eta = \sqrt{\frac{\hbar k^2}{2m\omega_t}}\cos[\theta], \tag{2.26}$$

also has a dependency on the angle $\theta = \angle(\boldsymbol{k}, \boldsymbol{x})$. After changing into the interaction picture $H_I = U^\dagger H_1 U$ with $U = \exp[\imath/\hbar \cdot H_0 t]$, terms oscillating with $\omega_f + \omega_a$ are omitted (*rotating wave approximation*) and we get:

$$H_I = \frac{\hbar\Omega_0}{2}\left(\sigma^{(+)}\mathrm{e}^{\imath\omega_a t}\mathrm{e}^{-\imath\omega_f t + \imath\phi}\cdot\exp\left[\imath\eta(a^\dagger\mathrm{e}^{\imath\omega_t t} + a\mathrm{e}^{-\imath\omega_t t})\right] + \text{h.c.}\right). \tag{2.27}$$

For a sufficiently small η we can expand the exponential function and arrive at:

$$H_I = \frac{\hbar\Omega_0}{2}[\sigma^{(+)}\mathrm{e}^{-\imath\delta t + \imath\phi}(1 + i\eta e^{\imath\omega_t t}a^\dagger + i\eta e^{-\imath\omega_t t}a + \mathcal{O}(\eta^2)) + \text{ h.c.}], \tag{2.28}$$

where $\delta = \omega_f - \omega_a$ is a detuning of the electromagnetic field from the atomic transition. For a weak coupling $\Omega_0 \ll \omega_t$, we can distinguish three important special cases, in which $\delta = 0$, $+\omega_t$ or $-\omega_t$ respectively. In each case one of the summands in eq. (2.44) will be time independent and dominating the Hamiltonian.

For $\delta = 0$ the electromagnetic field is tuned to the atomic resonance and we have:

$$H_I^{car} \approx \frac{\hbar\Omega_0}{2}[\sigma^{(+)}\mathrm{e}^{\imath\phi}(1 - \frac{\eta^2}{2}(2a^\dagger a + 1) + \text{ h.c.}], \tag{2.29}$$

coupling the states $|\uparrow, n\rangle$ and $|\downarrow, n\rangle$, where n is the number of quanta of the harmonic oscillation, which does not change upon a transition of the internal states of the ion. In this case we speak of the *carrier transition* (car).

If $\delta = -\omega_t$ the field is red detuned from the resonance, yielding:

$$H_I^{rsb} \approx \frac{\hbar\Omega_0}{2}[i\mathrm{e}^{\imath\phi}\eta\sigma^{(+)}a + \text{ h.c.}] \tag{2.30}$$

Upon absorbing a photon the internal state can only be excited, if the motional state is reduced by one phonon. Thus coupling the states $|\downarrow, n\rangle$ and $|\uparrow, n-1\rangle$. This is called the first *red side band transition* (rsb).

A blue detuned field with $\delta = +\omega_t$ leads accordingly to:

$$H_I^{bsb} \approx \frac{\hbar\Omega_0}{2}[i\mathrm{e}^{\imath\phi}\eta\sigma^{(+)}a^\dagger + \text{ h.c.}], \tag{2.31}$$

where the energy of a photon is high enough to excite the internal state as well as the motional state. Coupling the states $|\downarrow, n\rangle$ and $|\uparrow, n+1\rangle$ is therefore the first *blue side band transition* (bsb).

These approximations are applicable in the *Lamb-Dicke regime*, i.e. if $\eta^2(2n + 1) \ll 1$, c.f. eq. (2.29). Higher η and n will give rise to terms absorbing and emitting multiple phonons, leading to higher order side bands.

If we only have to consider two levels, the state vector reads $|\psi\rangle = c_1(t)\,|\uparrow, n\rangle + c_2(t)\,|\uparrow, n+m\rangle$ with the two probability amplitudes c_1, c_2. The time evolution is given by [Roo00; Win+98]:

$$\begin{pmatrix} c_1(t) \\ \\ c_2(t) \end{pmatrix} = \begin{pmatrix} \mathrm{e}^{-\imath\frac{\delta}{2}t}\left\{\cos[\frac{\Omega}{2}t] + \imath\frac{\delta}{\Omega}\sin[\frac{\Omega}{2}t]\right\} & -\imath^{1-|m|}\mathrm{e}^{-\imath\frac{\delta}{2}t+\imath\phi}\frac{\Omega_n^m}{\Omega}\sin[\frac{\Omega}{2}t] \\ \\ (-\imath)^{1-|m|}\mathrm{e}^{\imath\frac{\delta}{2}t-\imath\phi}\frac{\Omega_n^m}{\Omega}\sin[\frac{\Omega}{2}t] & \mathrm{e}^{\imath\frac{\delta}{2}t}\left\{\cos[\frac{\Omega}{2}t] - \imath\frac{\delta}{\Omega}\sin[\frac{\Omega}{2}t]\right\} \end{pmatrix} \cdot \begin{pmatrix} c_1(0) \\ \\ c_2(0) \end{pmatrix} \tag{2.32}$$

Here $\Omega_n^m = \Omega_0 \cdot \langle n+m|\,\mathrm{e}^{\imath\eta(a^\dagger+a)}\,|n\rangle$ is the motional state dependent Rabi frequency and $\Omega = ((\Omega_n^m)^2 + \delta^2)^{1/2}$ the effective Rabi frequency for a small detuning from the resonance.

If we start with $|\downarrow, n\rangle$, the probability for being in the $|\uparrow, n+m\rangle$ state after time t is then:

$$p_{|\uparrow,n+m\rangle} = |c_2(t)|^2 = \frac{(\Omega_n^m)^2}{\Omega^2}\,\sin^2\left[\frac{\Omega}{2}t\right] \tag{2.33}$$

In the resonant case $\delta = 0$ this reduces to a sinusoidal oscillation between both states with frequency Ω_n^m. If the interaction between the ion and the electromagnetic field can be switched off after a time of $t = \pi/\Omega_n^m$, a complete population inversion has taken place. This is referred to as a *π-pulse*. While a *$\pi/2$-pulse* with $t = \pi/(2\Omega_n^m)$ leads to an equal superpostion state, if we start in either electronic eigenstate. The further away the field frequency is from the resonance ($\delta \neq 0$), the faster the oscillation. However the amplitude drops and the population transfer is not complete anymore, as shown in fig. 2.6.

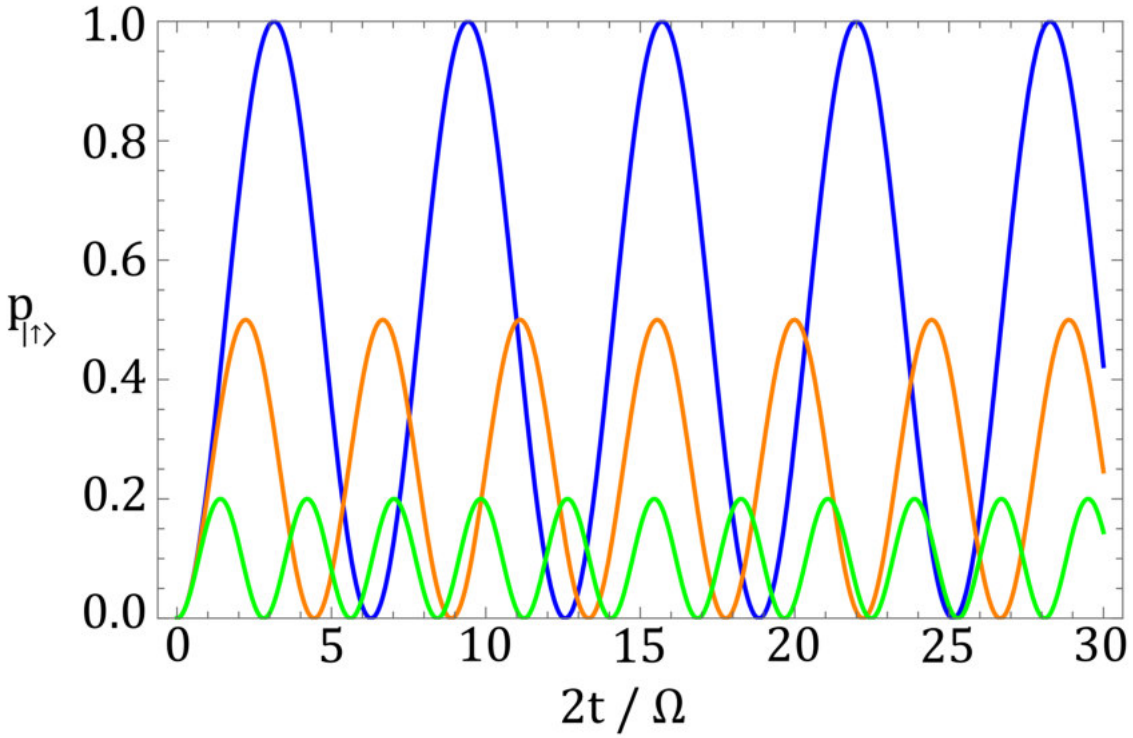

Figure 2.6: *Illustration of Rabi oscillations at resonance $\delta = 0$ (blue) and for $\delta/\Omega = 1$(orange) and $\delta/\Omega = 2$ (green).*

2.2.1 Annotations

Rabi Frequency

The Rabi frequency depends on the coupling mechanism between the ion and the electromagnetic field. In this work, we encounter the three cases of an electrical dipole (E1), a magnetical dipole (M1) and an electrical quadrupole (E2). For these, the interaction strength is given by [Jam98]:

$$\Omega_0^{(E1)} = \left| \frac{eA}{\hbar} \langle\downarrow| \mathbf{x}\cdot\boldsymbol{\epsilon} |\uparrow\rangle \right| \tag{2.34}$$

$$\Omega_0^{(M1)} = \left| \frac{g\mu_B A}{\hbar} \langle\downarrow| \boldsymbol{\sigma}\cdot\boldsymbol{\epsilon} |\uparrow\rangle \right| \tag{2.35}$$

$$\Omega_0^{(E2)} = \left| \frac{eA}{2\hbar} \langle\downarrow| (\mathbf{x}\cdot\boldsymbol{\epsilon})(\mathbf{x}\cdot\mathbf{k}) |\uparrow\rangle \right|, \tag{2.36}$$

with electron charge e the Bohr magneton μ_B and Landé factor g. The phonon dependency of Ω_n^m can be evaluated as [CG69; WI79]:

$$\langle n+m| \, \mathrm{e}^{i\eta(a^\dagger+a)} \, |n\rangle = e^{-\eta^2/2}\eta^{|m|}L_n^{|m|}(\eta^2)\left[\frac{n!}{(n+m)!}\right]^{\mathrm{sign}(m)/2}, \tag{2.37}$$

where $L_n^m(x)$ are the associated Laguerre polynomials. For the three transitions in the Lamb-Dicke regime with small n and $m = 0, \pm 1$ this can be approximated by:

$$\Omega_{car} = \Omega_0 \tag{2.38}$$

$$\Omega_{rsb} = \Omega_0\eta\sqrt{n} \tag{2.39}$$

$$\Omega_{bsb} = \Omega_0\eta\sqrt{n+1} \tag{2.40}$$

Damping

Rabi oscillations depend on the coherent time evolution of the system. Therefore, spontaneous emission of photons and population decay of the involved levels will limit these dynamics. The decay from $|\uparrow\rangle$ to $|\downarrow\rangle$ is characterised by the rate $\gamma_{\uparrow\downarrow}$ and leads to a damping of the oscillation. Likewise, $|\uparrow\rangle$ may decay to other atomic levels not considered so far with the rate $\Gamma_\uparrow$, leading to a permanent loss of a maximal possible population. Other processes, like field fluctuations or elastic collisions, will not change the population of the levels, but induce phase shifts with the rate γ_ϕ in the wave function, also leading to a loss of coherence. For a resonant field ($\delta = 0$) with a total decay rate much smaller than the Rabi frequency, the dynamic can be described by [Kos+05]:

$$|c_2(t)|^2 = \frac{1}{2}\left(\mathrm{e}^{-\frac{1}{2}\Gamma_\uparrow t} - \left(\cos[\Omega t] + \frac{3\gamma_{\uparrow\downarrow}+2\gamma_\phi}{4\Omega}\sin[\Omega t]\right)\mathrm{e}^{-\frac{1}{4}(2\Gamma_\uparrow+3\gamma_{\uparrow\downarrow}+2\gamma_\phi)t}\right) \tag{2.41}$$

A visualisation is shown in fig. 2.7.

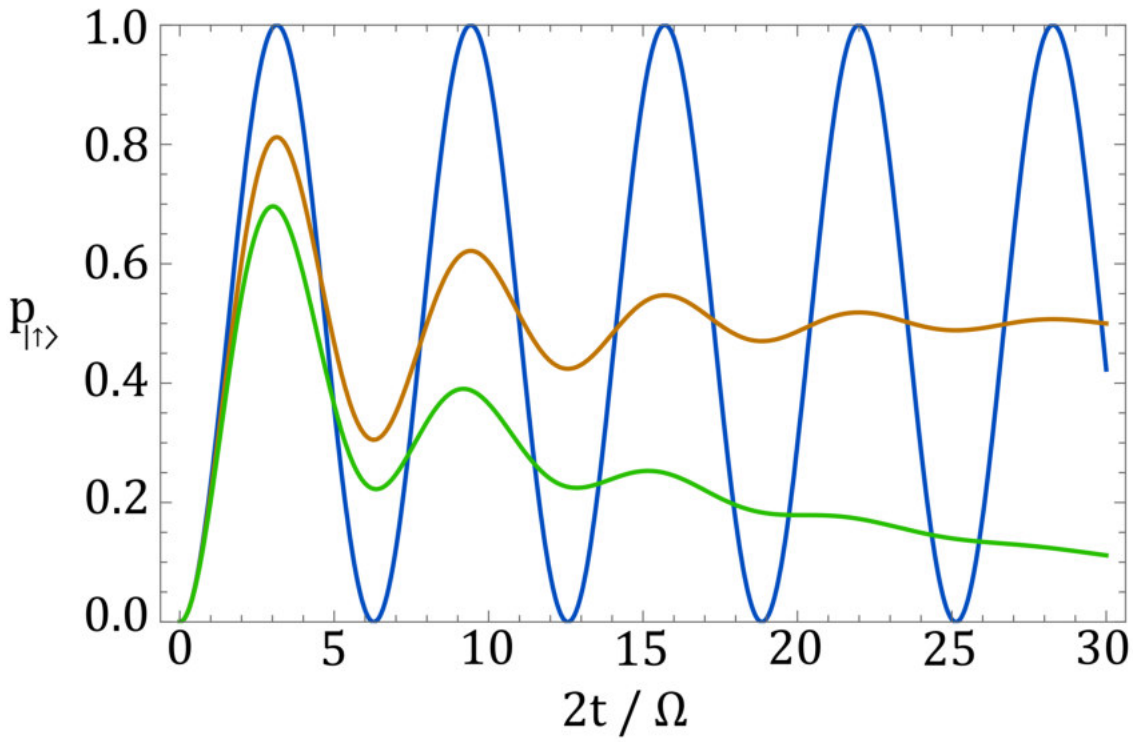

Figure 2.7: *Illustration of unhindered Rabi oscillations (blue) and damped Rabi oscillations with* $\gamma_{\uparrow,\downarrow}/\Omega = 0.2$*(orange) and additionally* $\Gamma_1/\Omega = 0.1$*(green).*

Generalisation for N Ions

For a chain of ions acting with the electromagnetic field, we have to substitute the position in (2.24) by the normal modes $\mathbf{Q}$ in the interaction term for the j^{th} ion:

$$k \cdot x_j = k \sum_n S_{nj} Q_n = \sum_n S_{nj} \eta_n (a_n + a_n^\dagger), \tag{2.42}$$

with the mode dependent Lamb-Dicke factor η_n, in which the mode frequency ω_n replaces ω_t. Thus, the dynamics of a side band on mode n is governed by the coupling strength $S_{nj}\eta_n$.

The Hamiltonian of N ions of mass m and two internal states $\{|\uparrow\rangle, |\downarrow\rangle\}$ trapped by harmonic potentials of a Paul trap in three dimensions can be expressed by their $3N$ collective modes with the angular frequency ν_j^ϕ for the j^{th} mode regarding the spatial direction $\phi \in \{x, y, z\}$:

$$H_0 = \sum_{\{j,\phi\}}^{3N} \hbar \nu_j^\phi (a_j^\phi)^\dagger a_j^\phi + \frac{\hbar}{2} \sum_j^N \omega_j \sigma_{z,j}, \tag{2.43}$$

where a_j^ϕ, $(a_j^\phi)^\dagger$ are the bosonic ladder operators, $\hbar\omega_j$ is the energy splitting of the two internal states for the j^{th} ion and $\sigma_{z,j} = |\uparrow\rangle_j \langle\uparrow|_j - |\downarrow\rangle_j \langle\downarrow|_j$. Driving this two-level system rotates the spin $\sigma_j^{(+)} = |\uparrow\rangle_j \langle\downarrow|_j$ in combination with excitation of motional quanta. The interaction of the the j^{th} ion with a near resonant driving field of angular frequency ω_{f} and phase ζ towards the atomic polarisation can be

approximately described by:

$$H_{I,j} = \frac{\hbar}{2}\Omega_j[\sigma_j^{(+)}\exp[-\imath\delta_j t + \imath\zeta] \times \exp\left[\imath \sum_{\{i,\phi\}}^{3N} \eta_{i,j}^{\phi}\left((a_i^{\phi})^{\dagger}\mathrm{e}^{\imath\nu_i^{\phi}t} + a_i^{\phi}\mathrm{e}^{-\imath\nu_i^{\phi}t}\right)\right] + \text{ h.c.}], \tag{2.44}$$

In the Lamb-Dicke regime with $\sum_{\{i,\phi\}}^{3N} \eta_{i,j}^{\phi}\sqrt{\left\langle (a_i^{\phi} + (a_i^{\phi})^{\dagger})^2 \right\rangle} \ll 1$, the strength of interaction is characterised by the Rabi frequency Ω_j and detuning of the driving field from the two-level transition frequency $\delta_j = \omega_{\mathrm{f}} - \omega_j$. Depending on this detuning either carrier transitions ($\delta_j = 0$), the red ($\delta_j = -\nu_j^{\phi}$) or the blue ($\delta_j = +\nu_j^{\phi}$) side band transitions are excited. While in the first case, only the internal state is rotated, in the other cases this goes along with the creation or annihilation of motional quanta [HRB08]. The dynamics is determined by the Lamb-Dicke factor $\eta_{i,j}^{\phi} = \sqrt{\hbar/2m\nu_i^{\phi}}\sum_{\chi}^{x,y,z} S_{i,j}^{\phi,\chi}k_j^{\chi}$, that depends on the projection of the wave vector k_j^{χ} of the incident driving field onto the modes of vibration, represented by the matrix $S_{i,j}^{\phi,\chi}$ comprising normalised displacements of the j^{th} ion in the χ^{th} direction due to the $\{i,\phi\}^{\text{th}}$ mode. The Lamb-Dicke factor $\eta_{i,j}^{\phi}$ is specific for every mode and depends on the eigenfrequency ν_i^{ϕ} and the direction of the eigenvector of each mode respectively. However, for ions in Paul traps showing mode frequencies ν_i^{ϕ} of a few MHz and in case of a typical magnetic dipole transition in the RF range, the resulting spin-motion coupling rates are low and direct magnetic spin-spin interactions are in the mHz regime [Kot+14].

2.2.2 Application

The following section briefly covers, how the interaction between ions and electromagnetic fields are the basic building blocks of a measurement cycle for the concrete case of $^{40}\mathrm{Ca}^{+}$. For the remainder of this work we will use the notation $|\uparrow\rangle$, $|\downarrow\rangle$ synonymously for the $\mathrm{S}_{1/2}$ (m=+1/2) and ($m = -1/2$) state, respectively.

Doppler Cooling

Quantum simulation schemes usually depend on the Lamb-Dicke regime. Thus, the ion's kinetic energy has to be reduced and kept at a low level, which can be achieved with Doppler cooling [HS75; WDW78]. For this, a laser field is applied with a frequency close but lower than that of an atomic transition. When the ion within the trap moves away from the laser source, it is virtually transparent, since the laser frequency will be shifted away from the resonance due to the Doppler effect. Moving in the opposite direction to the Laser propagation however, will shift the frequency towards the resonance. In this case, the ion will start scattering photons and experience a velocity dependent force. If the decay rate of the transition involved is much higher than the trap frequency, many scattering processes take place within one oscillation period of the ion, leading to a net energy transfer from the ion to the environment. Due to the isotropic nature of the spontaneous emission, the involved momentum-kicks cancel each other out on average. However, the expectation value of the squared momentum does not. This leads to a gain in kinetic energy and

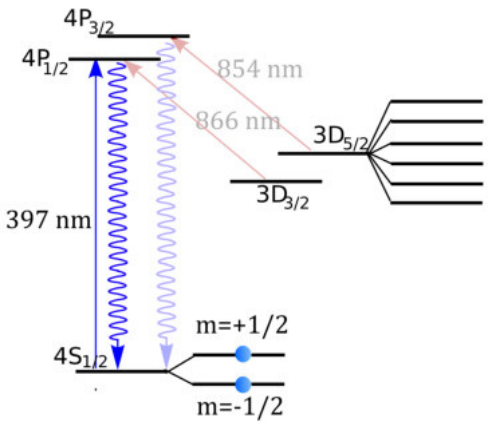

Figure 2.8: *Relevant transitions for Doppler cooling.*

setting a limit to the cooling process. A trapped ion can be cooled by a single laser, if its propagation direction has an overlap with all three trap axes. For Doppler cooling of calcium ions the $4S_{1/2} \leftrightarrow 4P_{1/2}$ transition is employed. The $4P_{1/2}$ state has a mean lifetime of 7.1 ns and the line width is usually broader than the Zeeman splitting of the ground state. During the cooling process 866 nm and 854 nm light is applied as well, to counteract a decaying of population to the 3D levels.

Initialisation

Once the ion is sufficiently cooled, the population of the electronic state will be more or less randomly distributed among the Zeeman sub-levels of the $S_{1/2}$ ground state. To start our measurement with well defined conditions, we have to initialise the ion to one of either states [Pos+09]. If we want to start our measurement in $|\downarrow\rangle$, we can apply a π-pulse to the $|\uparrow\rangle \leftrightarrow D_{5/2}$ (m=-1/2) transition. Followed up by a pulse of a few µs of 854 nm light, bringing the population to the short lived $P_{3/2}$ level. From there it decays back into either sub-level of the $S_{1/2}$. Thereby, we have transferred a percentage of the population formerly residing in the $|\uparrow\rangle$ to the $|\downarrow\rangle$ level. Repetition of the cycle will empty the $|\uparrow\rangle$ level gradually. This scheme is called *optical pumping*. We achieve a initialisation fidelity of 98(2) % with ten repetitions.

To recover any population stranded in the $D_{3/2}$ state, 866 nm light is applied together with the 854 nm pulse. To initialise into the $|\uparrow\rangle$ level, one simply uses e.g. the transition $|\downarrow\rangle \leftrightarrow D_{5/2}$ (m=+1/2). Alternatively the initialisation can be accomplished by $\sigma^{(-/+)}$ polarised 397 nm light. Due to the selection rules only the population of one of the $S_{1/2}$ sub-levels is excited to the $P_{1/2}$ level.

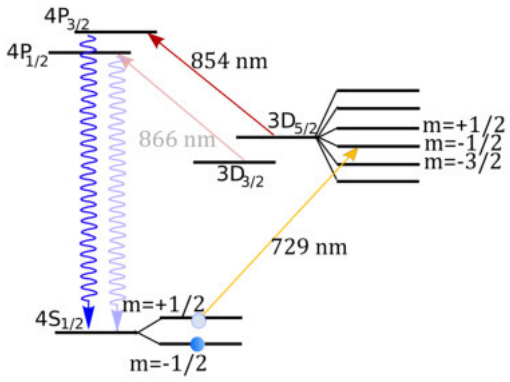

Figure 2.9: *Relevant transitions for initialisation.*

State Manipulation

Now that the ion is prepared in one of the Zeeman sub-levels of the ground state, a coherent manipulation of the dynamic can be implemented. In the line of this work, this is done by an oscillating magnetic field about 10 MHz to directly drive the transition between the sub-levels of the ground state (Zeeman qubit). We will refer to this oscillating magnetic field as HF field, for a distinction from the RF trapping potential. Alternatively, an optical qubit can be implemented using e.g. the states $S_{1/2}$ and $D_{5/2}$, wherein the transition can be driven with a laser of 729 nm.

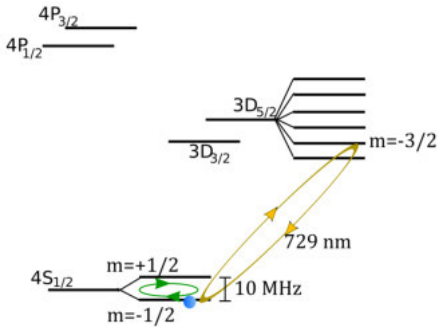

Figure 2.10: *Relevant transitions for state manipulation.*

Detection: State and Ion Discrimination

After the manipulation of the ion's state, we have to read out the result. For this we apply 397 nm light and detect the fluorescence of the ion decaying from the $P_{1/2}$ to the $S_{1/2}$ level. To avoid an accumulation of population in the $D_{3/2}$ state, 866 nm light is active as well. If the ion is in the $D_{5/2}$ level, we will only detect a low count number due to background scattering. Each picture of the camera will give us one fluorescence count number, which we then have to assign to the *dark* $D_{5/2}$ or the *bright* $S_{1/2}$ state.

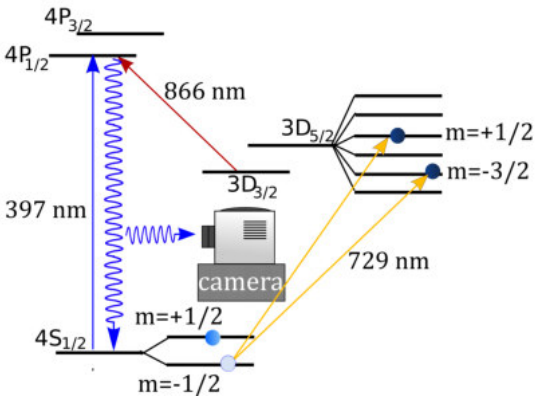

Figure 2.11: *Relevant transitions for detection and shelving. Illustration of* bright *and* dark *states.*

Before the actual measurement, we take several pictures of the ion in the bright and the dark state. The latter is simulated by switching off the 866 nm light during the detection, whereby the population will quickly be stuck in the $D_{3/2}$ state and will not fluorescence anymore. We can then plot the occurrence of any fluorescence count number in a histogram, see fig. 2.12. Each state gives rise to a Poisson distribution of the count numbers. To distinguish between both states, one defines a threshold value σ. If the count number n is smaller than the threshold value σ, we say the ion is dark. If $n > \sigma$, the ion is bright. Which σ to choose, may depend on the measurement: whether it is less damaging to assign an ion in the $D_{5/2}$ state erroneously to be bright or a $S_{1/2}$ ion to be dark. For the balanced case, the geometrical mean $\sigma = \sqrt{b \cdot d}$ of the

expectation values b and d of the distributions can be employed. Longer detection times will separate the distributions further, but increases the chance of a decay of the $D_{5/2}$ state with a lifetime of 1.05 s. We usually work with a detection time of 4 ms.

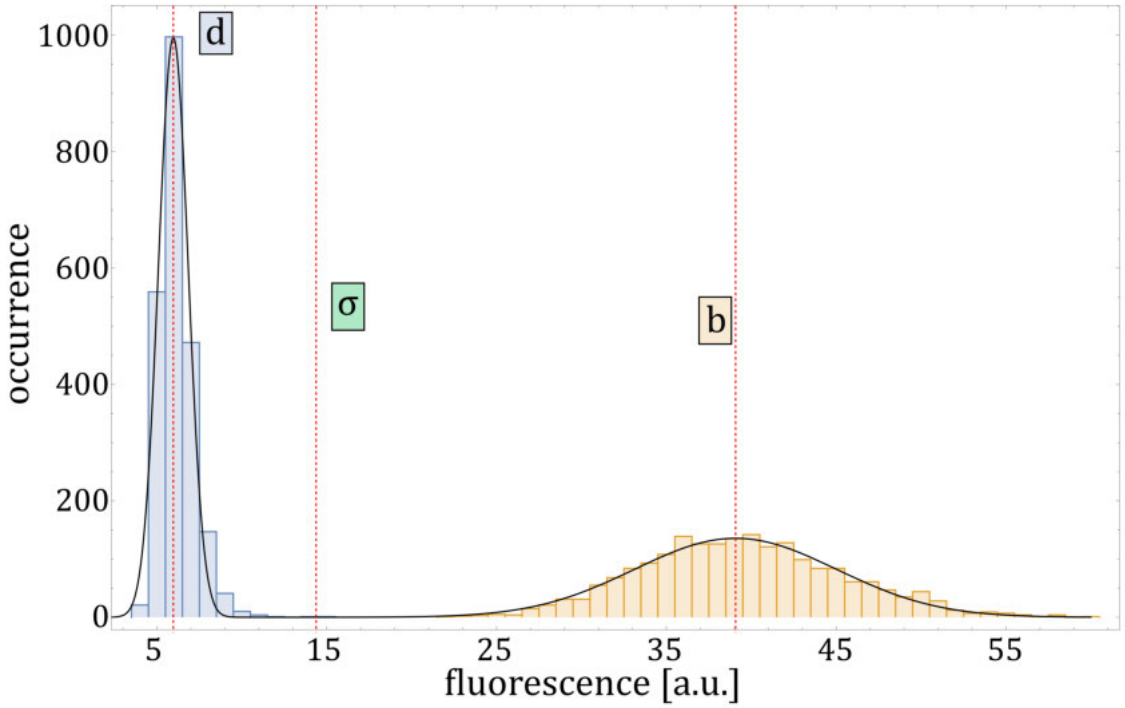

Figure 2.12: *Histogram of the fluorescence count number of a dark(blue) and bright(red) state. The Poisson distribution was approximated with a Gaussian.*

Now each measurement will give us the information dark = 0 or bright = 1. To read out the actual state of the ion, we have to repeat the measurement several times with the exact same parameters. Each time we get the information 0 or 1 and after a sufficiently large amount of measuring cycles, we can determine the probability for the ion to be in the $S_{1/2}$ or $D_{5/2}$ state. If we want to read out any other state, like a superposition of the ground state sub-levels, we have to map it to a population difference between the S and D levels. For this, we can employ a π-pulse on the $|\downarrow\rangle \leftrightarrow D_{5/2}(m=+1/2)$ transition, just prior to the detection. Thus, the population of one of the sub-levels is hidden from the 397 nm light during the detection and the ion is therefore dark. Putting population to a long lived state to suppress interaction induced dynamics is commonly referred to as *shelving*. To improve the efficiency of the procedure, we also employ another transition to empty the (m=-1/2) state. Since the π-time of transition in the optical regime depend strongly on the laser amplitude and the motional state of the ion, a more robust transfer can be achieved with a rapid adiabatic passage (RAP) [MK01; Wun+07]. For this, the laser frequency of the according transition is detuned from resonance and then slowly swept over the resonance. Slowly means, that a temporal change in the detuning should be much smaller than the square of the peak Rabi frequency. Under these conditions, an inversion of the population takes place, wherein frequency and amplitude fluctuations have no noteworthy influence.

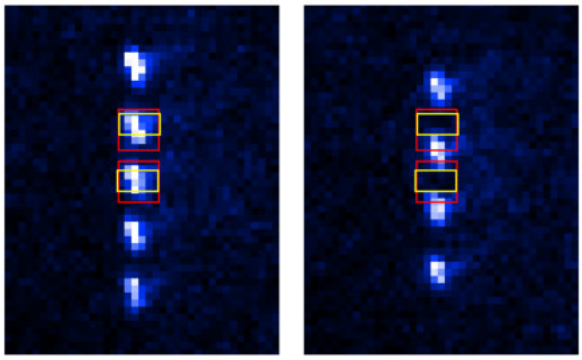

Figure 2.13: *Typical camera image with different sized regions of interest.*

If working with more than one ion, we can distinguish between the fluorescence of different ions due to the spatial resolution of the camera. Figure 2.13 shows the typical image of a five ion crystal. The handling of the camera[2] allows to define several regions of interest (ROI), that are read out separately. However, a loss of an ion is not always detected, if the size of the ion fluorescence is comparable to the inter ion distance. In the right part of the figure, the red ROIs will still have enough counts to pass the threshold, even though one of the ions has escaped the trap. Whereas the yellow ROIs notice an ion loss, but they will produce a histogram with a lower distance between the distributions, which will lead to higher (inner state) detection errors as long as no loss of ions has occurred.

2.3 Presence of a Magnetic Field Gradient

2.3.1 Considering One Spatial Dimension

In this section we recapitulate the findings of [Wun02]. A magnetic field gradient makes the energy related to the electronic state of ion j position-dependent due to the Zeeman effect:

$$\langle\psi|\, H_e \,|\psi\rangle = \pm\left(E_j(z^{(0)} + \frac{\hbar}{2}\frac{\partial\omega_{a,j}}{\partial z_j}\bigg|_{z^{(0)}} q_j\right) \tag{2.45}$$

We can compare this new term to the energy spacing of the normal mode with the lowest frequency ω_1 and the width of a wave packet in the ground state Δz_1:

$$\epsilon = \frac{|\partial_z\omega_j|\Delta z_1}{\omega_1} \tag{2.46}$$

If ϵ is much smaller than one, the additional potential term will influence the eigenfrequencies of the oscillator modes merely insignificantly. Thus, the motional state can be described by the unperturbed oscillator modes Q_n with $P_n = m\dot{Q}_n$ and the complete Hamiltonian reads:

$$H = \frac{\hbar}{2}\sum_{n=1}^{N}\omega_a(z_{0,n})\sigma_{z,n} + \frac{1}{2m}\sum_{n=1}^{N}P_n^2 + \frac{m}{2}\sum_{n=1}^{N}\omega_n^2 Q_n^2 + \frac{\hbar}{2}\sum_{n=1}^{N}\left[\frac{\partial\omega_{a,n}}{\partial z_n}\bigg|_{z_{0,n}}\sigma_{z,n}\sum_{l=1}^{N}S_{l,n}Q_l\right] \tag{2.47}$$

With the unitary transformation $\tilde{H} = U^\dagger H U$, where

$$U = \exp\left[-\imath\sum_l\left(\frac{1}{2m\nu_l^2}\sum_n\frac{\partial\omega_{a,n}}{\partial z_n}\bigg|_{z_{0,n}}\sigma_{z,n}S_{l,n}\right)P_l\right] \tag{2.48}$$

[2] by A. Wiens [Wie11] using the Andor Software Development Kit

it can be rewritten as

$$\tilde{H} = \frac{\hbar}{2}\sum_{n}^{N}\omega_{a,n}(z_n^{(0)})\sigma_{z,n} + \sum_{n}^{N}\hbar\omega_{t,n}a_n^\dagger a_n - \frac{\hbar}{2}\sum_{n<l}^{N}J_{n,l}\sigma_{z,n}\sigma_{z,l} \tag{2.49}$$

with the following abbreviations:

$$\epsilon_{n,l} = S_{n,l}\tfrac{\partial_z\omega_{a,l}\Delta z_n}{\omega_n} \tag{2.50}$$

$$J_{n,l} = \textstyle\sum_j^N \omega_j\epsilon_{j,n}\epsilon_{j,l} \tag{2.51}$$

Thus, the magnetic field gradient gives rise to an additional term compared with eq. (2.23). The last part of $\tilde{H}$ denotes a coupling between the spins of two ions with a coupling strength $J \sim (\partial_z|B|)^2/\omega_n^{3/2}$. The interaction of ion j with a driving field is given by:

$$H_1 = \frac{\hbar}{2}\Omega_R(\sigma_j^{(+)} + \sigma_j^{(-)})\left\{\exp\left[\sum_n \imath S_{n,j}\eta_n(a_n^\dagger + a_n) - \imath\omega_f t + \imath\phi\right] + \text{h.c.}\right\} \tag{2.52}$$

As before, we make the unitary transformation $\tilde{H}_1 = U^\dagger H_1 U$, change into the interaction picture $H_I = V^\dagger\tilde{H}_1 V$ with $V = \text{Exp}[\imath/\hbar\tilde{H}t]$, and neglect fast rotating terms. With the following notation

$$\eta'_{n,j}\exp[\imath\phi_j] = \eta_n S_{n,j} + i\epsilon_{n,j} \tag{2.53}$$

$$\phi_j = \frac{\pi}{2} - \tan[\frac{\eta_n S_{n,j}}{\epsilon_{n,j}}] \approx \frac{\pi}{2} \tag{2.54}$$

$$\Delta_j = \frac{1}{2}\sum_n \omega_{t,n}\epsilon_{n,j}, \tag{2.55}$$

we further neglect terms that are only proportional to η instead of η'. This is justified, since a magnetic dipole transition in the HF range gives rise to $\eta \approx 10^{-9}$ for a calcium ion in a Paul trap. We then get:

$$H_I = \frac{\hbar}{2}\Omega_R\left\{\mathrm{e}^{\imath(\omega_{a,j}+\Delta_j-\omega_f)t+\imath\phi}\sigma_j^{(+)}\exp\left[\imath\sum_n \eta'_{nj}(a_n^\dagger \mathrm{e}^{\imath\omega_{t,n}t+\imath\phi_j} + a_n\mathrm{e}^{-\imath\omega_{t,n}t-\imath\phi_j}\right] + \text{h.c.}\right\}, \tag{2.56}$$

which is basically the same as (2.27) with an effective Lamb-Dicke factor $\eta'_{nj} \approx \epsilon_{nj}$ and a constant shift Δ_j of the resonance frequency.

2.3.2 More Than One Spatial Dimension

Starting from eq. (2.43) and applying a strong magnetic field gradient makes the transition frequency $\omega_\text{j}(q_j^\phi)$ of the j^{th} ion depend on its position q_j^ϕ in the trap, wherein $\phi \in \{x, y, z\}$. A corresponding small displacement $\xi_j^\phi = q_j^\phi - q_{0,j}^\phi$ from the equilibrium position $q_{0,j}^\phi$ in the magnetic field gradient modifies H_0 by

$$\pm\frac{\hbar}{2}\left.\frac{\partial\omega_j(q_j^\phi)}{\partial q_j^\phi}\right|_{q_{0,j}^\phi}\xi_j^\phi\sigma_{z,j}. \tag{2.57}$$

This additional spin-motion coupling leads to an effective Lamb-Dicke factor $\tilde{\eta}_{i,j}^{\phi}$ that can be substituted for $\eta_{i,j}^{\phi}$ in (2.44), and if $\eta_{i,j}^{\phi} \ll \tilde{\eta}_{i,j}^{\phi}$:

$$\tilde{\eta}_{i,j}^{\phi} \approx \sqrt{\hbar/2m(\nu_j^{\phi})^3} \sum_{\chi}^{x,y,z} S_{i,j}^{\phi,\chi} \left. \frac{\partial \omega_j}{\partial q_j^{\chi}} \right|_{q_{0,j}^{\chi}} \tag{2.58}$$

The effective Lamb-Dicke factor depends on the projection of the magnetic field gradient onto the eigenmodes. We employ a magnetic field gradient in the radial plane and use a magnetic dipole transition, thus (5.1) results in an effective Lamb-Dicke factor of

$$\tilde{\eta}_{i,j}^{\phi} = \frac{\Delta m_{\mathrm{S}}\, g\, \mu_{\mathrm{B}}}{\sqrt{2\hbar m(\nu_j^{\phi})^3}} \left(S_{i,j}^{\phi,x} \left. \frac{\partial B}{\partial q_j^{x}} \right|_{q_{0,j}^{x}} + S_{i,j}^{\phi,y} \left. \frac{\partial B}{\partial q_j^{y}} \right|_{q_{0,j}^{y}} \right), \tag{2.59}$$

with the difference in the projection of the total angular momentum represented by Δm_{S}, the Landé factor g, the Bohr magneton μ_{B} and the absolute value of the magnetic field B.

Furthermore, the additional spin-motion coupling induced by the magnetic field gradient leads to an indirect spin-spin coupling, that is meditated via the collective vibrational modes. The Hamiltonian H_0 with the additional spin-motion coupling can be transformed to show the effective spin-spin coupling:

$$H_{ss} = -\frac{\hbar}{4} \sum_{i \neq j}^{N} J_{i,j} \sigma_{z,i} \sigma_{z,j}, \tag{2.60}$$

where the coupling strength between the i^{th} and j^{th} ion is given by:

$$J_{i,j} = \frac{\hbar}{2m} \sum_{\phi,\chi}^{x,y,z} \left. \frac{\partial \omega_i}{\partial q_i^{\phi}} \right|_{q_{0,i}^{\phi}} \left. \frac{\partial \omega_j}{\partial q_j^{\chi}} \right|_{q_{0,j}^{\chi}} \sum_{\{h,\psi\}}^{3N} \frac{S_{h,i}^{\psi,\phi} S_{h,j}^{\psi,\chi}}{(\nu_h^{\psi})^2} \tag{2.61}$$

Thus, the spins of the two ions couple indirectly, if there is a mode $\{h, \psi\}$ in which the two ions move along the respective spatial directions ϕ, χ of the magnetic field gradient field at the respective ion's position. The coupling strength $J_{i,j}^{\phi,\chi}$ can be tuned via the magnetic field gradient and the mode frequencies. By using different modes, spins of different ions can be coupled as long as the mode has a non-vanishing projection onto the magnetic field gradient field for those ions. Especially in planar ion crystals, the directions of eigenvector and frequencies of modes allow for tailoring complex spin interactions.

Taking typical experimental conditions for ion traps into account, we find that magnetic field gradients on the order of 10 to 100 T/m are required to drive dynamics based on spin-spin coupling on a ms-timescale.

2.4 Creating a Magnetic Field Gradient

There are two ways to create a magnetic field, either by using permanent magnets or current carrying wires. The first has a better stability, while the other benefits from the possibility to change the field strength in situ, but suffers from Joule heating. In the following we discuss the second approach. A previous attempt to include a current carrying wire into the surface trap itself [BS15] led to a high probability of an ion loss when the current was switched on. For very low currents of 200-300 mA, sideband spectroscopy showed various additional lines that were associated with non linear resonances of the trap [WFW93]. The voltage-kicks going along with the current pulse excited the ions too strongly. To avoid this behaviour in the trap used for this work, the wires were put beneath the trap chip. Thus, the chip's ground plane at the same time serves as a shielding of the ion from the electric field of the current carrying wires.

For the purpose of spin-motion or spin-spin coupling as described in the last chapter, a high magnetic field gradient is needed, while an additional offset magnetic field is not desirable. Therefore, two additional wires are necessary to nullify the two magnetic field components of the first wire at the position of the ion. We assume that a magnetic field component along the wires is negligible, if the wires take a straight course over a length, that is much longer than the distance between the ion and the wires. We used straight wires, that were arranged in parallel for at least a total length of all the DC electrodes of the trap chip.

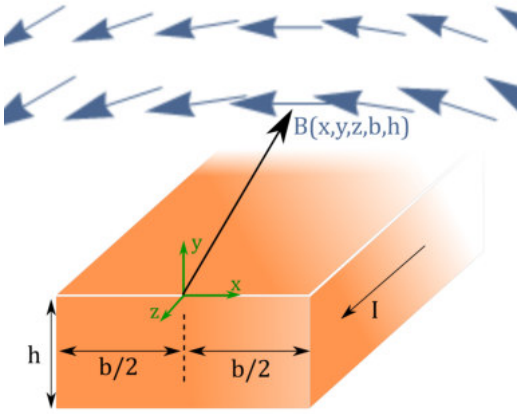

Figure 2.14: *Dimensions for a wire with rectangular cross section.*

For a fast optimisation of the geometry we used the simple model of an infinite long wire in z direction with a rectangular cross section. The model wire has a width b and a height h and carries a current I. The current density j is modelled to be homogeneous within the wire:

$$j(\mathbf{x}) = \begin{cases} \frac{I}{bh} & \text{if } -\frac{b}{2} \leq x \leq \frac{b}{2},\ -h \leq y \leq 0 \\ 0 & \text{otherwise,} \end{cases} \tag{2.62}$$

see also fig. 2.14. For the magnetic field above the wire ($y > 0$), one then obtains from the Biot-Savart law:

$$\begin{aligned} B_x(\mathbf{x}) = \frac{\mu_0 I}{4\pi bh}\Bigg(& 2(h+y)\ \text{ArcTan}\left[\frac{2(h+y)}{b+2x}\right] - 2y\ \text{ArcTan}\left[\frac{2y}{b+2x}\right] \\ & +2(h+y)\ \text{ArcTan}\left[\frac{2(h+y)}{b-2x}\right] - 2y\ \text{ArcTan}\left[\frac{2y}{b-2x}\right] \\ & -(\frac{b}{2}-x)\ \text{Log}\left[\frac{b^2-4bx+4(h^2+x^2+2hy+y^2)}{b^2-4bx+4(x^2+y^2)}\right] \\ & -(\frac{b}{2}+x)\ \text{Log}\left[\frac{b^2+4bx+4(h^2+x^2+2hy+y^2)}{b^2+4bx+4(x^2+y^2)}\right]\Bigg) \end{aligned} \tag{2.63}$$

$$
\begin{aligned}
B_y(\mathbf{x}) = \frac{\mu_0 I}{4\pi b h}\Bigg(& (b+2x)\ \mathrm{ArcTan}\left[\frac{2(h+y)}{b+2x}\right] - (b+2x)\ \mathrm{ArcTan}\left[\frac{2y}{b+2x}\right] \\
& -(b-2x)\ \mathrm{ArcTan}\left[\frac{2(h+y)}{b-2x}\right] + (b-2x)\ \mathrm{ArcTan}\left[\frac{2y}{b-2x}\right] \\
& +(h+y)\ \mathrm{Log}\left[\frac{b^2+4bx+4(h^2+x^2+2hy+y^2)}{b^2-4bx+4(^2+x^2+2hy+y^2)}\right] \\
& -y\ \mathrm{Log}\left[\frac{b^2-4bx+4(x^2+y^2)}{b^2-4bx+4(x^2+y^2)}\right]\Bigg)
\end{aligned}
\tag{2.64}
$$

The total field components can now be calculated as the sum of one instance of these expressions per wire with a suitable coordinate transformation. We took a symmetric approach, i.e. the ion is above the middle of the central (w_c) wire and both the outer wires (w_{o1} and w_{o2}) have the same width. Also the distance d between two wires is the same, c.f. fig. 2.15. Then the field components are:

$$
B_i^{\mathrm{tot}}(x,y) = B_i^{w_c}(x,y) + B_i^{w_{o1}}(x+D,y) + B_i^{w_{o2}}(x-D,y), \tag{2.65}
$$

where $i = (x,\ y)$ denotes the component, and $D = b_o/2 + b_c/2 + d$ is the distance measured from origin to origin, wherein b_o is the width of the outer wires, b_c is the width of the central wire and d is the distance between the wires. If the current in the central wire flows in the opposite direction to the current in the outer wires, a quadrupole field results, as shown in fig. 2.15.

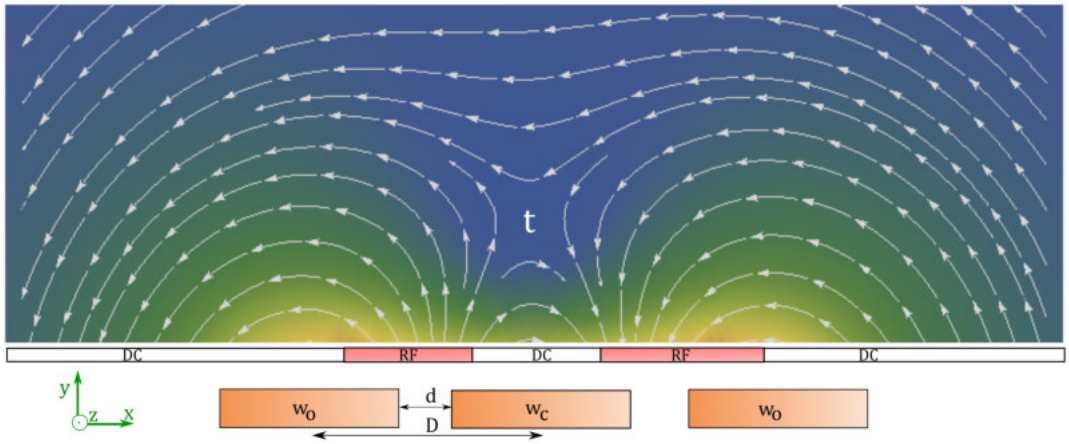

Figure 2.15: *Magnetic field created by three wires. Arrows indicate direction and colour the absolute value of the field, where cold colours signify a low and hot colours a high value. Currents in the wires are set such, that they create a magnetic quadrupole field with a vanishing magnetic field at the trap center 't'. Below the magnetic field, the trap electrodes and the wires are shown (not true to scale).*

The height of the wires is basically fixed by the method of manufacturing the wires. The same is true for the distance between the wires, which should be as short as possible. Thus, leaving the following degrees of freedom to generate a high field gradient: the width b_o and current I_o of the outer wires and the width b_c and current I_c of the inner wires. On the other hand, we have the following constraints:

- The magnetic field at the position of the ion has to vanish for both components in the plane perpendicular to the wires.

- We set a relative arbitrary upper limit for the current of 20 A, influenced by coarse approximations of the gradient and its expected spin-motion coupling on one hand and technical feasibility of sending pulses of this magnitude on the other hand.

- The resistance increase of the wire due to Joule heating has to be limited to 50 % after a current pulse of 10 ms. Complete meltdown of wires have been reported for stronger heating. The temperature increase in a wire mounted on a substrate can be described by [Gro+04]:

$$\Delta T[t] = \frac{hb\rho j^2}{2\pi\lambda}\Gamma\left[0, \frac{Cb^2}{4\pi^2\lambda t}\right], \tag{2.66}$$

  where λ is the heat conductivity and C the heat capacity of the substrate, ρ the cold resistivity of the wire and Γ the incomplete Gamma function. We choose aluminium nitride (AlN) as substrate due to its relative high $\lambda = 170$ W/m·K and $C = 2.41 \cdot 10^6$ J/m^3·K.

We were looking into two methods to manufacture the wires. The first method was based on thick-film technology. Printing three layers on top of each other can reach a height of the wires of $h = 40$ µm. Glueing the trap chip (see sec. 3.1) directly on top of the wire gives a trapping height of the ion above the wires of $y_0 = 200$ µm. As material AgPt (FK1071[3]) was used due to its relative low sheet resistance of 6 mΩ/sq. The minimal distance between the wires is $d = 150$ μm to avoid electrical shorts due to a broadening of the printed structures till they are completely cured, see production report in appendix A. Maximising the magnetic field gradient under this constraints leads to the graph depicted on the left side of fig. 2.16. However,

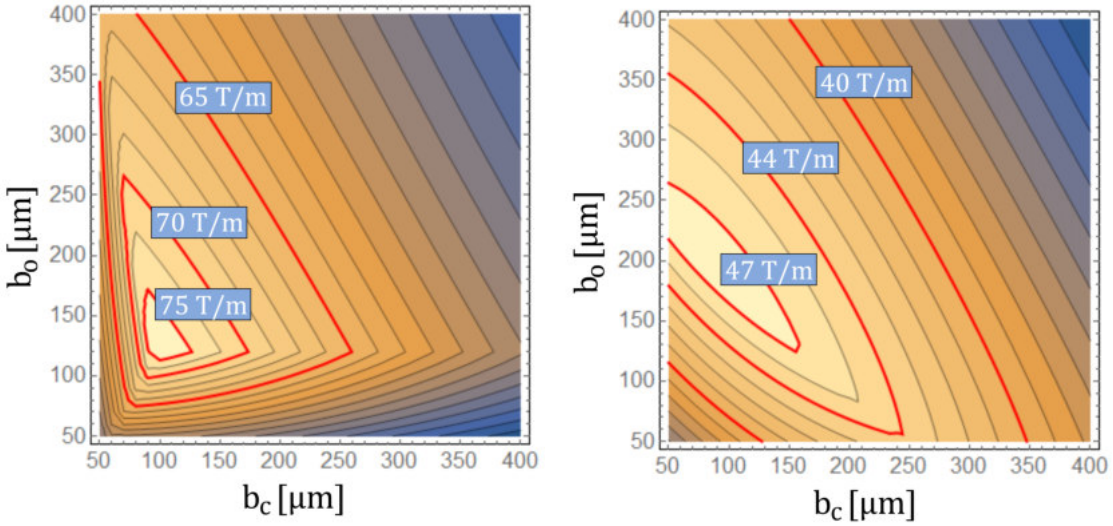

Figure 2.16: *Contour plot of the expected magnetic field gradient for different geometries of the wires. You can clearly see the regions where different constraints limit the geometry. Left: design based on thick film technology with a height of 40 µm. Right: etched copper with a height of 127 µm. The values for the magnetic field gradient are achieved for a maximum current of 20 A in one of the wires.*

[3]Frauenhofer-Institut für Keramische Technologien und Systeme IKTS, Dresden

printing several layers on top of each other is not yet perfected leading to a high number of rejects during the production. In the second method, the wires were etched into a thin copper layer on top of the substrate. Commercially available units go down to a copper layer thickness of $h = 127$ µm. The trap chip is glued to the substrate, leading to a trap height of the ion above the wires of $y_0 = 223$ µm. The minimal distance $d = 150$ µm between the wires is about the same as before. The bulk resistivity is $\rho = 1.68 \cdot 10^{-8}$ Ωm. With this framework we get the picture shown on the right side of fig. 2.16.

Chapter 3

Experimental Setup

This chapter describes the implementation of the trap chip and the experimental apparatus. Major design choices were based on how to get a high magnetic field gradient and how to include an argon gun for the cleaning of the trap chip. The description starts with the Paul trap realised as a microchip, goes on with the supporting structures and the vacuum chamber, followed up by the optical and electrical setup.

3.1 The Trap Chip

The actual trap consists of an approximately 415 nm thin layer of aluminium coated[1] on a micro-machined alumina chip[2]. It has a five wire design with asymmetric RF electrodes, see sec. 1.2. The width of the electrodes in the order (outer DC, smaller RF, central DC, bigger RF, outer DC) is (700, 100, 100, 120, 700) µm. According to eq. (2.11) this leads to a trapping height of 96.9 µm above the surface and a lateral shift of 1.1 µm from the middle of the central DC electrode. The outer DC electrodes are divided into nine independent segment pairs, with a length of 430 µm each. They are insulated by 10 µm wide gaps in the material. These gaps coincide with 50 µm deep trenches in the supporting glass structure to reduce electrical stray fields from the insulator and to avoid a short circuit after an Ar^+ bombardment, c.f. sec. 3.3.5. The chip has a length and a width of 2×1 cm and a height of 250 µm. It features a 150 µm deep slot on the backside to fit in the current carrying wires that generate the magnetic field gradient, see fig. 3.1. This was done to minimise the distance of the wires to the trapped ions. As can be seen in fig. 3.1, the wires are arranged in straight lines parallel to the trap z-axis for a length exceeding an accumulated length of all the DC electrodes. However, the wires fan out before they reach an edge of the trap chip. Thereby, the risk is minimised, that the backside slot of the trap chip resembles a predetermined breaking point. For an overview of the fabrication method of the trap chip, see [BS15, p. 71]. The chip is glued with EPO-TEK H20E[3] to a supporting filter board, containing all electrical supply lines. The trap chip is placed on top of the wires such that the distance between the centre of the wires to the trapped ions is close to 285µm, see Fig. 3.1(b). The cut-out has a clearance fit regarding the wires of 400 µm in a direction perpendicular to the

[1] Thanks to N. Daniilidis

[2] Translume, Inc. - Advanced Glass Micromachining

[3] Epoxy Technology, Inc.

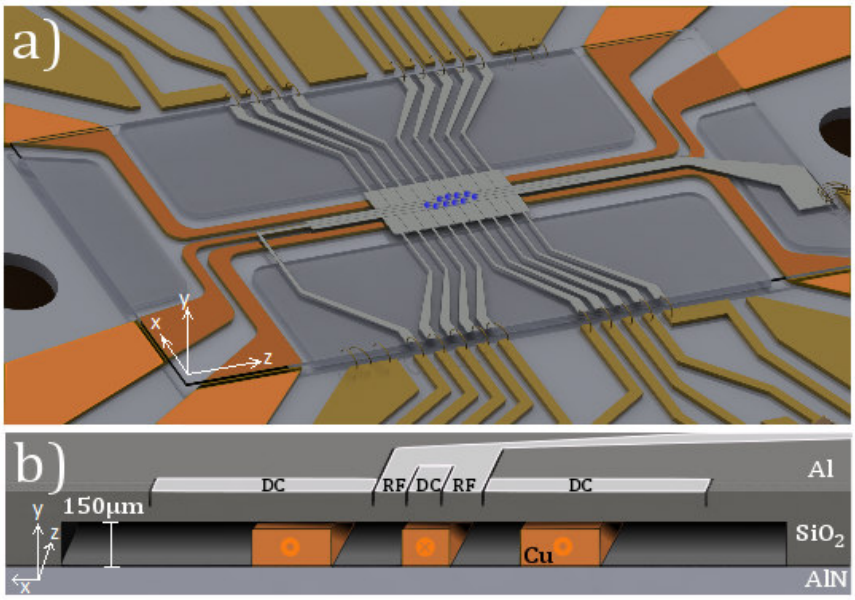

Figure 3.1: ***a)*** *sketch of the employed surface electrode ion trap made from fused silica (SiO_2, dark grey) and coated with a layer of 0.4 µm aluminium, with two RF, one central DC rail and further 2×9 segments for confinement with submerged current wires (orange), which allow for the generation of a transverse magnetic field gradient. A ground plane covering the remaining fused silica surface outide the electrode section is not displayed for illustration purpose.* ***b)*** *Cross section of the chip with 50 µm deep and 10 µm wide trenches (Translume Inc.) between the trap electrodes (light grey) and a cut-out at the backside to fit in three current carrying wires to generate a magnetic quadrupole field at the ion position.*

trap axis and was temporarily fixated with spacers during the glueing process of the trap chip to the AlN chip carrier. Electrical contact is ensured by ball bonding with 25 µm thick gold wires.

3.2 Filter Board and Wires

The electrical supply lines are etched in a 127 µm thick copper layer mounted on a 635 µm thick AlN board[4]. The board is additionally coated with gold for a proper bonding process to the chip. As seen in fig. 3.2, the filter board comprises two sets of nine DC supply lines for the nine segments of DC electrodes on both sides of the RF electrodes and one DC supply line for the RF-ground electrode between the RF electrodes. These 19 lines to the DC electrodes include each a first order low pass filter made from a SMD resistor with a resistance of 332(2) Ω and a SMD capacitor with a capacitance of 6.3(2) nF, measured after the re-flow process and therefore a cut-off frequency of 76 kHz. To each line a kapton insulated wire is soldered[5], which leads to a feed-through in the vacuum chamber. The board also hosts a solder/bonder pad for the RF drive as well as the three wires to create the magnetic field gradient. They have a target width of 150 µm, a distance of 175 µm

[4]Hubert Heusner - Industrievertretungen und Handel
[5]with the alloy SN96.5AG3CU.5, ANSI: J-STD-006B, co. kester

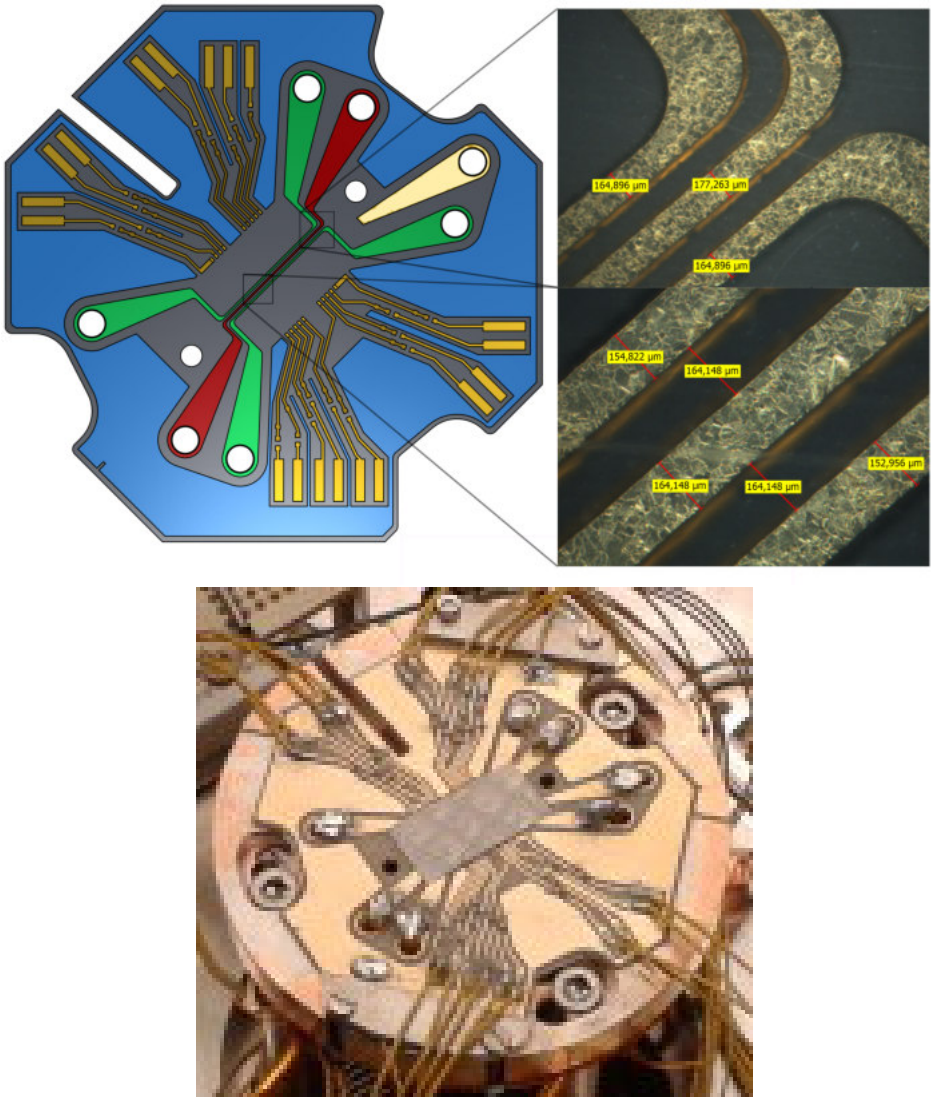

Figure 3.2: ***top:*** *CAD-drawing of the filter board. Yellow: DC supply lines. Light yellow: RF supply. Green and Red: wires for magnetic field gradient. Blue: ground plane. On the right: a close up view of the wires made with an optical microscope.* ***bottom:*** *picture of the assembled trap. Note the pattern on the chip, which is actually the reflection of the flow box lighting due to the high reflectivity of the aluminium surface.*

between each other and the same height of 127 µm as the DC supply lines. For further details see sec. 2.4 and also appendix A, which comprises a survey of these wires as well as of an alternative approach made with thick film technology.

Since the whole system is designed to withstand currents of 20 A, they have to be supplied by cables of 2 mm diameter, which are inserted from the backside of the board for strain-relief. Joule heating from the wires is the reason why AlN was chosen as a mount due to its high thermal conductivity of 170 $\frac{\mathrm{W}}{\mathrm{m \cdot K}}$ [Rei02]. The filter board is glued with EK-1000-MP[6] and additionally clamped to a copper plate, which itself is water cooled to 16°C, see next section. The assembled setup can be seen in the bottom part of fig 3.2.

[6]Epoxy Techonology, Inc.

3.3 Vacuum Chamber

To trap single ions in Paul traps, collisions with air molecules must be avoided, since the transmitted energy is usually higher than the potential well of the trap, especially for surface traps. Therefore, the chip is placed within a stainless steel vacuum chamber based on ConFlat standard (CF), sealed with copper gaskets to reach an ultra high vacuum (UHV). The chamber has the form of a prism with an octagon cross-section, wherein each of the eight sides comprises a flange. Seven of the eight octagon side flanges comprises view ports to let laser light into the chamber. The eighth flange connects the chamber to vacuum pumps. The chamber is closed by a top flange and a bottom flange in a direction of the prism axis. The trap chip is suspended at the top flange, with the electrodes facing the bottom flange. All electrical feed-throughs are arranged in the top flange. The bottom flange comprises a further view port granting a camera a line of sight perpendicular to the trap chip's surface. A sketch of the setup is shown in figs. 3.3 and 3.4, exact dimensions of the chamber and details can be found in [Deu07]. Top and bottom flange of the main chamber have been exchanged for this work and are described in this section, c.f. also [BS15].

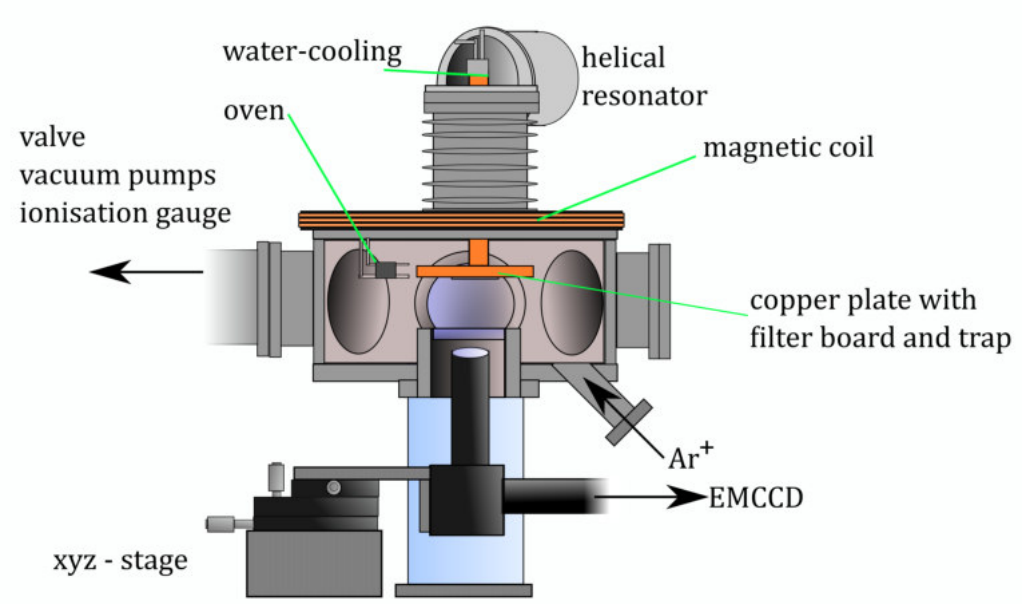

Figure 3.3: *front view of the vacuum main chamber.*

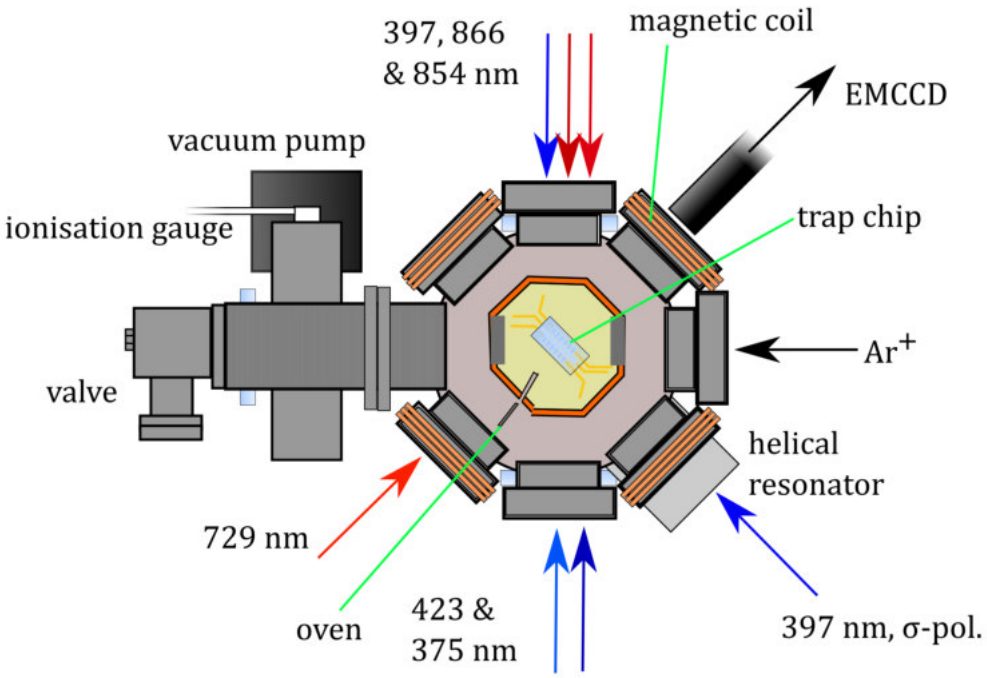

Figure 3.4: *bottom view of the vacuum main chamber.*

3.3.1 Vacuum

To reach an UHV, the apparatus was evacuated with a turbo-pump connected to the chamber with a DN63 CF-valve and baked out at a temperature of 120°C for two weeks. After the bake-out, the valve was closed and the vacuum is maintained continuously by an ion getter pump[7] and additionally by a titan sublimation pump[8], which is set off every 24 h. The pressure inside the chamber is monitored with a ionisation gauge[9] and settled finally around $7 \cdot 10^{-11}$ mbar.

3.3.2 Water-cooling

As mentioned above, the trap and filter board are glued to a water cooled copper plate, which is sketched to the right and made of Oxygen Free High Conductivity (OFHC) copper. The plate itself is clamped by a loose type clamp also made from OFHC copper to a OFHC copper pipe, wherein the copper plate is screwed to the copper clamp. The copper pipe extends to the outside of the vacuum chamber by going through a wide opening of the top flange and through an accurately fitting hole in a DN75 CF flange closing said opening of the top flange. The cooling pipe has a diameter of 16 mm, a wall thickness of 2 mm and comprises a immersion nozzle to feed fresh water close to the copper plate into the cooling pipe. The copper pipe features a thickening at the upper end, providing an inbuilt gasket to seal the chamber with the copper pipe itself, wherein the thickening is clamped between the DN75 CF flange and a DN16 CF flange. The copper plate is further mechanically stabilised by three parallel rods fixed to the DN75 CF flange in parallel to the copper

[7] VacIon Plus 20, StarCell 20 l/s, Varian Inc.
[8] SB-1020, Hositrad - Vacuum Technology
[9] UHV-24p, Varian Inc.

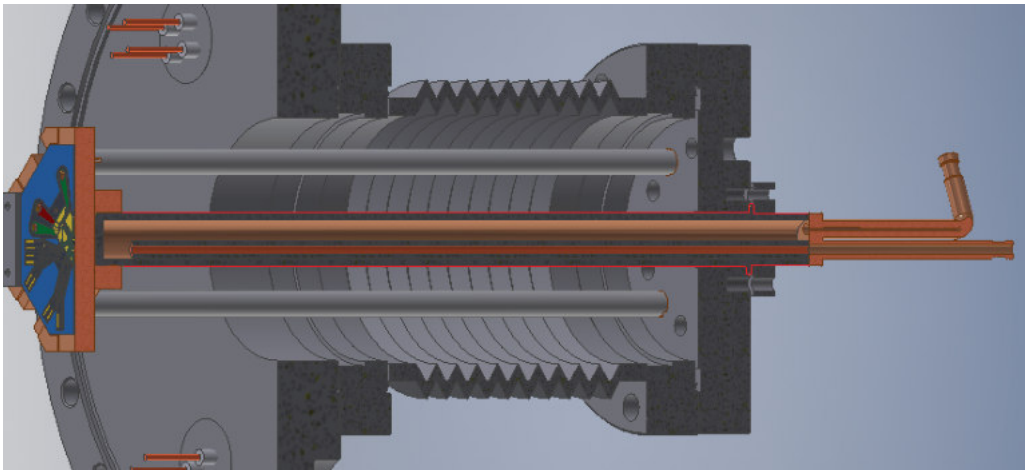

Figure 3.5: *CAD drawing of the trap suspension through the top flange of the vacuum chamber, including a water-cooled copper structure at its centre. The filter board with the trap chip is glued and clamped to a copper plate, with is mounted to a copper pipe and additionally stabilised by three steel rods, of which two are visible here.*

pipe. Outside the chamber the pipe is connected by fabric tubes to a water cooling device[10] to keep the copper plate and filter board at a temperature of 16°C.

3.3.3 Flex Bellow

As can be seen in fig. 3.5 the trap suspension at the DN75 CF flange is connected via a flex bellow to the chamber's top flange (DN200 CF). This allows to change the relative height of the trap within the vacuum chamber. Three different positions are of special interest. Firstly, a position around the middle of the lateral viewports, within the working distance of the objective lens. Secondly, a position where the calcium oven aims at the backside of the copper plate, see fig. 3.6. Thereby protecting the filter board and trap chip from short circuits, when the oven is put to higher temperature than necessary to trap ions. This is typically the case during the bake-out of the chamber to get rid of an oxide layer blocking the oven pipe. Thirdly, a position that is optimised for a bombardment with Ar^+, see sec. 3.3.5. The last position differs from the other two, since the design of the setup was limited by the reuse of the chamber pot from a previous experiment, that did not include an argon cannon.

3.3.4 Calcium Oven

The source for the calcium is an oven as sketched in fig 3.6. It is filled with calcium granules[11], which evaporate upon heating the oven by sending an electrical current through it. A detailed study of this method can be found in [Rot03]. The oven is in line with the slit in the filter board, seen in the top left corner of fig. 3.2, while maintaining a position slightly beneath the conducting layer of the board. This way the atom beam is cut off by the AlN mount and short circuits are prevented,

[10] model no.: SZ 1394 10, Van der Heijden - Labortechnik GmbH
[11] 99.5% purity, Alfa Aesar - A Johnson Matthey Company

while still hitting the trap centre. The oven typically runs at 3.8 A[12] during experiments, ensuring loading times of several seconds to a few minutes. Neutral atom fluorescence can be distinguished from back ground scattering at around 4.5 A.

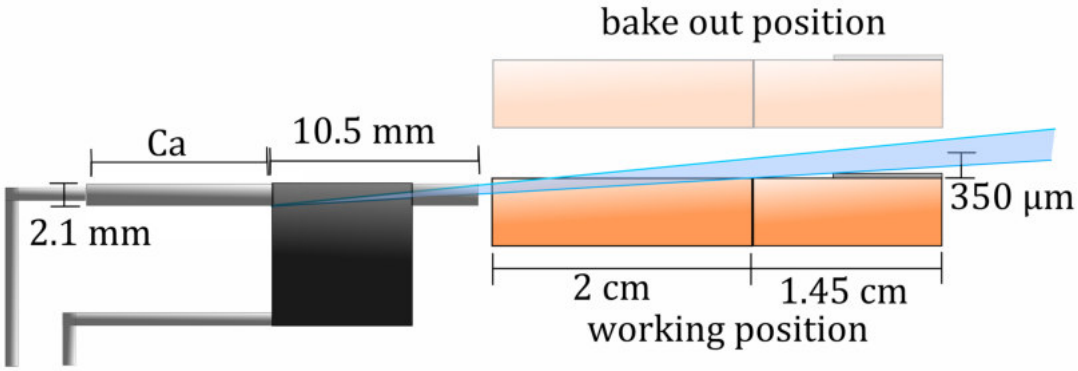

Figure 3.6: *schematics of the calcium oven and different positions of the trap on top of the copper plate. In a working position, the oven opening is situated just below the filter board, such that a rear edge of the slit in the copper plate casts a shadow onto the DC supply lines and the trap chip.*

3.3.5 Argon Cannon

The setup includes an argon cannon[13] at the bottom flange to clean the surface of the trap chip. It has been shown that this process can diminish the heating rate of a trap, usually associated with carbon residues, to a level usually only achieved in cryogenic environments [Hit+12]. The process itself is very forcible, several layers of the trap's coating are removed and the spill can subsequently short circuit the electrodes. Since the success rate of this procedure is still low [HD13] it has not been employed during this work, where heating rates play a minor role.

3.3.6 Magnetic Coils

There are five independent magnetic coils outside the vacuum chamber to provide a quantisation axis for the calcium ions in the trap and to compensate magnetic stray fields in the laboratory. Two can create a magnetic field along the trap axis, another two along the lateral axis and a single coil is wound around the top flange, creating a magnetic field perpendicular to the trap surface, c.f. fig. 3.3. The strength of the magnetic field is of the order of 4 Gs, while applying 0.5 to 2 A[14].

[12]DC power supply, type 3234.1, Statron Gerätetechnik GmbH
[13]IS 40C1 - Henniker Scientific Ltd.
[14]E3633A power supply, Keysight Technologies

3.4 Optics

The following section is dedicated to the optical setup of the used lasers and the imaging system. All lasers are situated on an additional optical table. There the power is split with a λ/2-plate and a polarising beam splitter (PBS) into two branches to supply two different experiments. After further manipulation of the beam, the light is guided with optical fibres to the optical table with the ion trap. All auxiliary optics are present twice to ensure independent working with both experiments at the same time. In the following figures optics that do not belong to this experiment are greyed out. The wavelength of the lasers are monitored by a wave meter[15].

3.4.1 423 & 375 nm - Photo-Ionisation

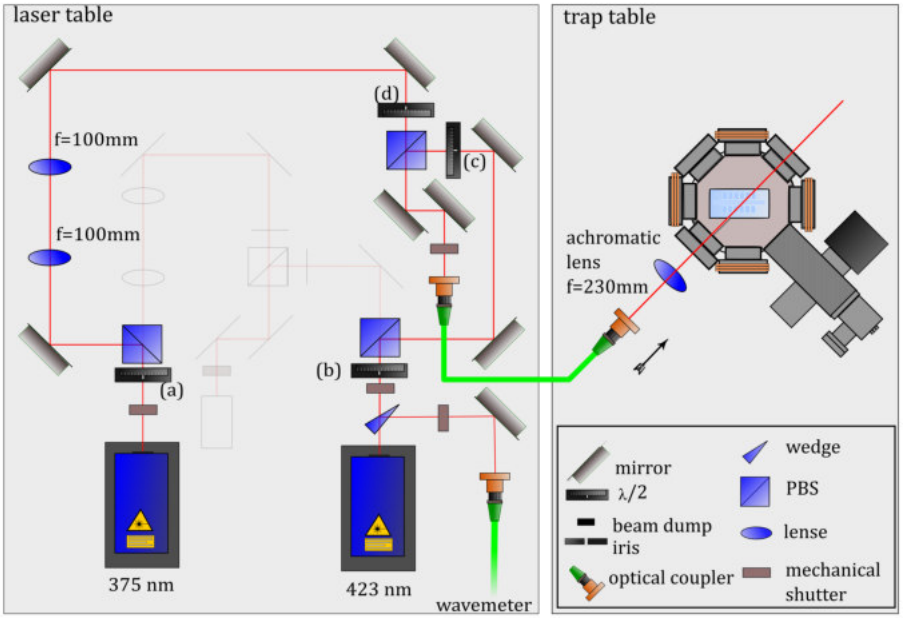

Figure 3.7: *schematics of the optical setup for 423 and 375 nm light. λ/2-plates (a) and (b) set a beam power distribution between the experiments. λ/2-plates (c) and (d) set a power ratio of the 423 nm and 375 nm light in the superimposed beam.*

To trap calcium emitted from the oven, it first has to be ionised. This happens in a two step photo-ionisation process [Gul+01]. First it is resonantly excited to the 4s4p $^1P_1$ state of neutral calcium with light of 423 nm wavelength from a first diode laser[16]. From there, another laser field with a wavelength of 375 nm from a second diode laser[17] excites the atoms further to a Rydberg state, that is easily ionised by the present electric fields of the trap. The setup is shown in fig. 3.7.

Both laser beams are overlapped using a PBS, wherein λ/2-plates allow the independent adjustment of the laser powers. To compensate the different focus length for both wavelengths when coupling into the optical fibre, the 375 nm beam has

[15] HF-ANGSTROM WSU-30, HighFinesse GmbH
[16] DL 100 pro design, TOPTICA Photonics AG
[17] iBeam-Smart-375, TOPTICA Photonics AG

to pass a telescope, consisting of two lenses, with one lens mounted on a micrometer translation stage. At the trap table the collimated beam from the fibre is focused using an achromatic lens, leading to a focus diameters of $f_{423} = 108$ µm and $f_{375} = 93$µm at the trap centre. We typically work with a power of $P_{423} = 600$ µW and $P_{375} = 350$ µW measured as fibre output in front of the vacuum chamber.

Blocking the 375 nm beam allows to observe neutral atom fluorescence due to the spontaneous decay of the 4s4p $^1P_1$ state, which peaks around 422.79220(5) nm in our setup. Usually, we work at a wavelength of 422.79230-422.79245 nm for fast loading. The wavelength of the 375 nm laser is not monitored, since it is not important for the ionisation process to which exact Rydberg level the ion is excited. Both beams are switched on and off by selfmade mechanical shutters based on loudspeakers [Sin+02].

3.4.2 397 nm - Doppler Cooling, Initialisation & Read-out

For Doppler cooling, σ-pumping and read-out of the qubit's state the $4S_{1/2} \leftrightarrow 4P_{1/2}$ transition is employed with a corresponding wavelength of 396.95918(5) nm. The source for the light is a diode laser[18], that is frequency-stabilised by the Pound-Drever-Hall method. The setup is shown in fig. 3.8. As can be seen, the wavelength measured is the one emitted by the laser. However the wavelength gets manipulated with an acousto-optical modulator (AOM) before the beam hits the ion. The exact frequency that is added is usually not monitored.

Two lenses narrow down the beam diameter before the laser power is distributed between four branches: one Doppler and σ-pumping beam per experiment. For a fast and clean switching of the beam AOMs[19][20] in a double-pass configuration [Don+05] are used, before coupling into the optical fibre. The AOMs are supplied by a device[21] ("AOM driver") based on a voltage controlled oscillator (VCO). Its output frequency and amplitude can be controlled stagelessly by a external voltage level. This setup allows to scan the laser frequency by roughly 50 MHz while locked to the cavity and to adjust the power of the beam. In fig. 3.9 the time evolution of the laser intensity during the switching process is shown.

At the trap table the Doppler beam passes another PBS to clean the polarisation and is then overlapped with the re-pump beams, see next section. For this a glass plate, with a coating is used that has a high reflectivity for blue light and a high transmissivity for red light. The resulting beam is focused with an achromatic lens. The beam diameter at the trap centre is $f_{\mathrm{Dop}} = 102$ µm with a typical power of $P_{\mathrm{Dop}} = 15\ \mu$W. A polarisation of the σ-beam is also cleaned by a PBS and thereafter circular polarised by a λ/4 plate before focused to the trap centre with a power of $P_\sigma = 10$ µW.

[18] DL 100 pro design, TOPTICA Photonics AG
[19] Doppler: I-M110-3C10BB-3-GH27, Gooch & Housego PLC
[20] σ: QZF-80-20-397, Brimrose corp.
[21] developed by Heinz Lenk
[22] PDA 36A-EC, Thorlabs Inc.

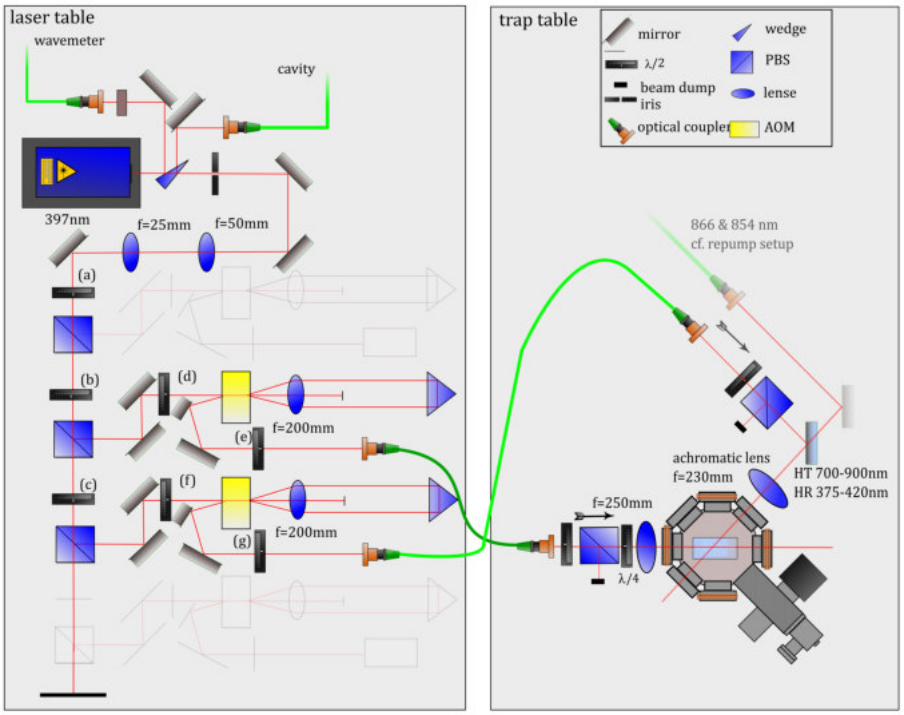

Figure 3.8: *schematics of the optical setup for 397 nm light. One laser is used for four two different experiments with each two branches, i.e. a Doppler-branch for Doppler cooling and a σ-branch for initialisation. λ/2-plates (a), (b) and (c) set a beam power distribution between the four branches. λ/2-plates (b), (d) and (e) are in the σ-branch and λ/2-plates (c), (f) and (g) are in the Doppler-branch. A setting of the absolute power is carried out with the λ/2-plates on the trap table.*

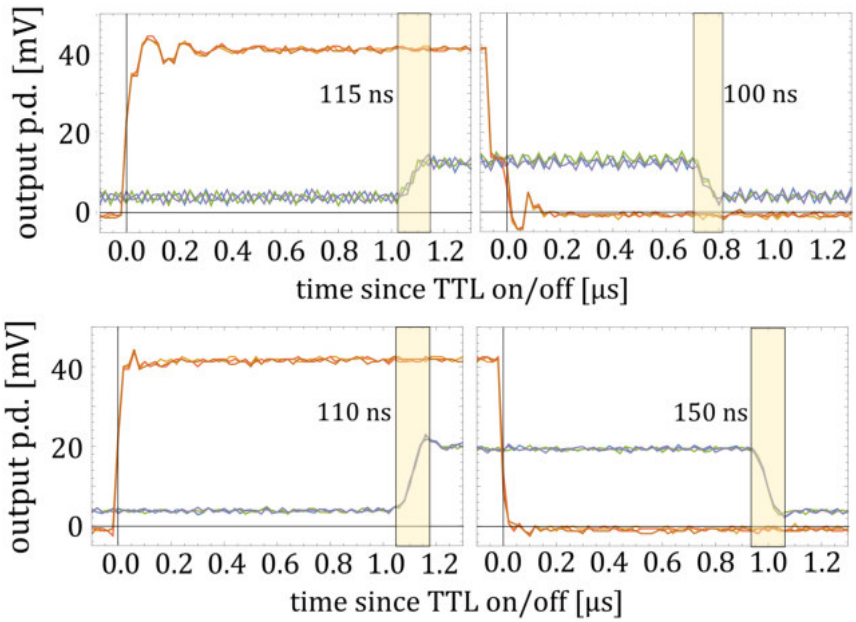

Figure 3.9: *trigger and switching time of the AOM for 397 nm light: Doppler (top) and σ (bottom). Shown are three measurements. Cold colours are the output of a photodiode[22], positioned in front of the view port. Hot colours indicate the TTL signal divided by 100.*

3.4.3 866 & 855 nm - Re-pumping

Light at 866.4518(1) nm and 854.4434(1) nm is needed to empty any population stuck in the meta stable $3D_{3/2}$ and $3D_{5/2}$ states respectively. The light is created by diode lasers[23], where the 866 nm output is frequency-stabilised by the Pound-Drever-Hall method, [Dre+83]. Both beams are overlapped before coupled into a single optical fibre and can be switched independently with AOMs[24] in a double-pass configuration as described in the above section. The setup is shown in fig. 3.10. The beam diameter at the trap centre is $f_{866,854} = 53$ µm with a typical power of $P_{866} = 120$ µW and $P_{854} = 50$ µW. The switching times are shown in fig. 3.11.

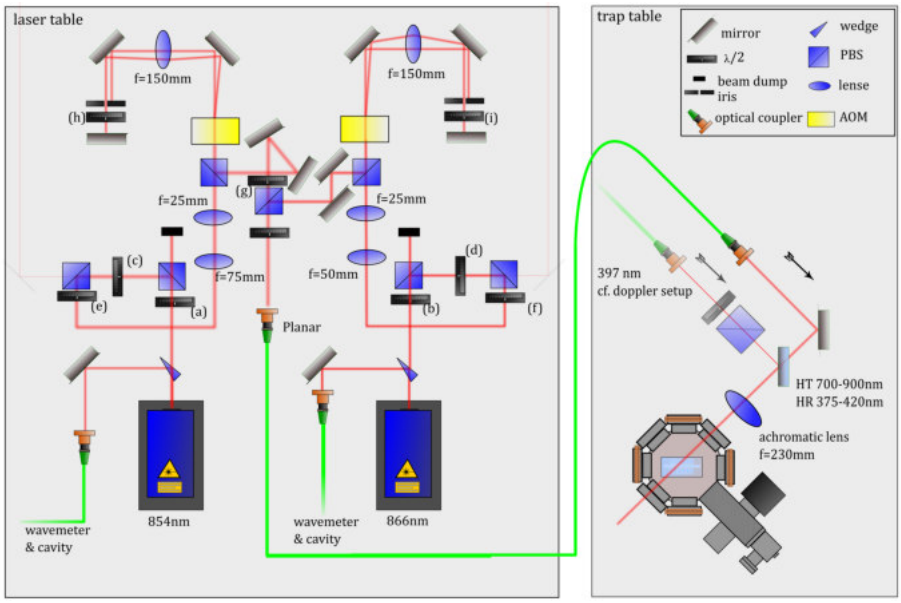

Figure 3.10: *schematics of the optical setup for 866 and 854 nm light. λ/2-plates (a) and (b) set a total power of the beams. λ/2-plates (c) and (d) set a beam power distribution between the experiments. λ/2-plates (e), (h), (f) and (i) set the polarisation for the AOM double-pass. λ/2-plate (g) and sets a power ratio of the 866 nm and 854 nm light in the superimposed beam.*

[23] 866 nm: DL pro, 854m: DL 100 pro design, TOPTICA Photonics AG
[24] TEF-80-20-845, Brimrose corp.

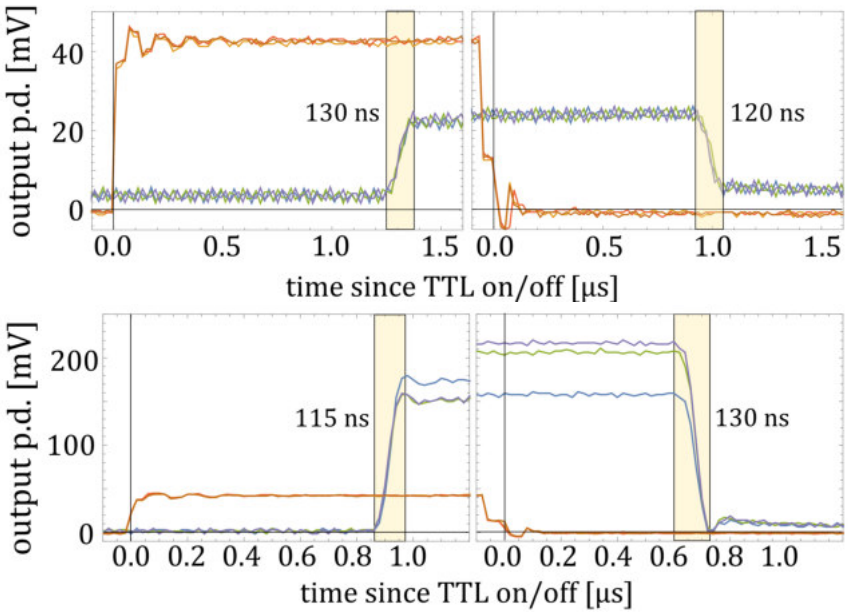

Figure 3.11: *trigger and switching time of the AOM for 866 nm light (top) and 854 nm (bottom) light. Shown are three measurements. Cold colours are the output of a photodiode, positioned in front of the view port. Hot colours indicate the TTL signal divided by 100.*

3.4.4 729 nm - Spectroscopy and Shelving

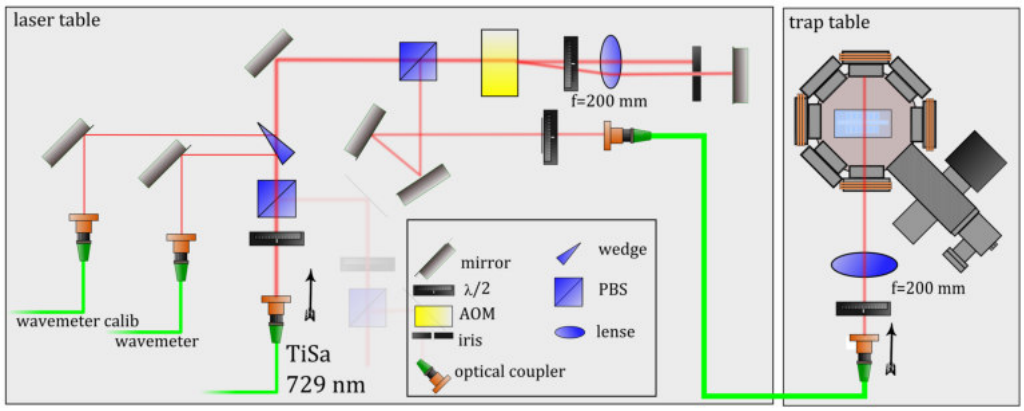

Figure 3.12: *schematics of the optical setup for 729 nm light.*

729.34730(1) nm light drives the $4P_{1/2} \leftrightarrow 3D_{5/2}$ transition which is used to shelve an ion into the metastable excited state and hide it during detection, see sec. 2.2.2, but also for optical pumping and spectroscopy of the trap modes. It is generated by a Titan:Sapphire laser system[25] (Ti:Sa) coupled to a high finesse cavity, that was build up in the neighbouring laboratory. Details of the setup can be found in [Mac12]. It is transported to the laser optical table in our laboratory with a polarisation maintaining fibre. There the power is split up between experiments and the beam can be switched by an AOM[26] in double pass configuration before guided to the trap

[25] Matisse TX, Sirah Lasertechnik GmbH
[26] TEM-85-2-729, Brimrose corp.

table. The switching behaviour is seen in fig. 3.13. A λ/2-plate allows to rotate the polarisation direction in respect to the trap axis. The beam waist at the trap centre is f= 33 µm with a typical power of 15 mW. We also use the stabilised Ti:Sa light to calibrate our wave-meter. To realise e.g. a RAP-sequence, chirped pulses have to be applied, therefore this AOM is driven by a signal generator[27], whose output is amplified first by the ZFL-500HLN+ and then by the ZHL-3A+[28].

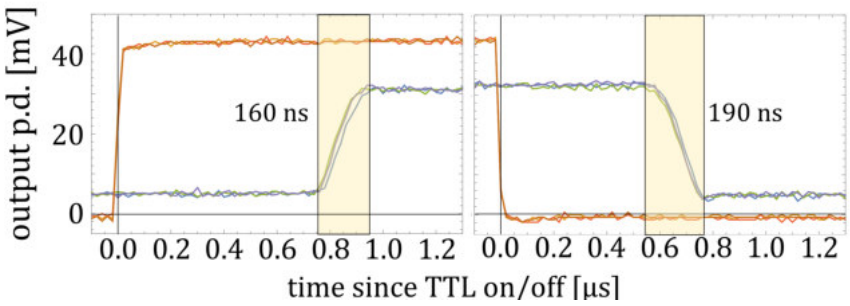

Figure 3.13: *trigger and switching time of the AOM for 729 nm light. Shown are three measurements. Cold colours are the output of a photodiode, positioned in front of the optical fibre leading to the trap. Hot colours indicate the TTL signal divided by 100.*

3.4.5 Detection

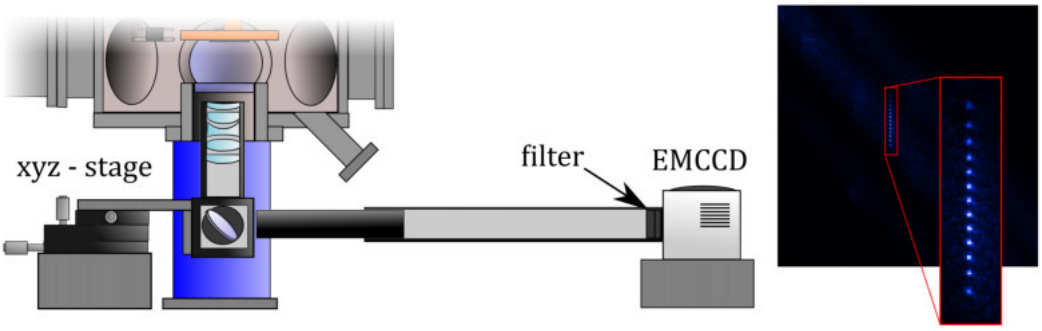

Figure 3.14: *imaging optics for the detection of ions. To the right is a typical image of the camera.*

The light emitted by the ions on the $P_{3/2}$ to $S_{1/2}$ transition at 397 nm is collected by a custom made object lens[29] with an aperture NA≈ 0.27 and a targeted magnification of M=20. The image is caught by an Electron Multiplying Charge-Coupled Device (EMCCD)[30], see fig. 3.14. For a better contrast the light is filtered[31], mainly to suppress stray light from the re-pump lasers. To avoid an overexposure of the camera, the beam path is shielded with a PCB pipe from the surrounding laboratory lighting. The camera has a distance of 110 cm from the object lens and we achieve

[27] VFG-150, TOPTICA Photonics AG
[28] both from Mini-Circuits
[29] Sill Optics GmbH
[30] iXon X_3 x-5665, Andor Technology Ltd.
[31] FF01-377/50-25, Semrock, IDEX Health & Science, LLC.

a resolution of 1.02 µm/px, measured from comparison of inter-ion distance of a two ion crystal with theoretical values [Jam98]. With a total area of 512x512 pixel of the EMCCD this allows to image about one DC pad at a time. The object lens is mounted on an xyz-translation stage to scan the whole trap area and adjust the focus.

3.5 Electronic Setup

3.5.1 Trap RF Drive

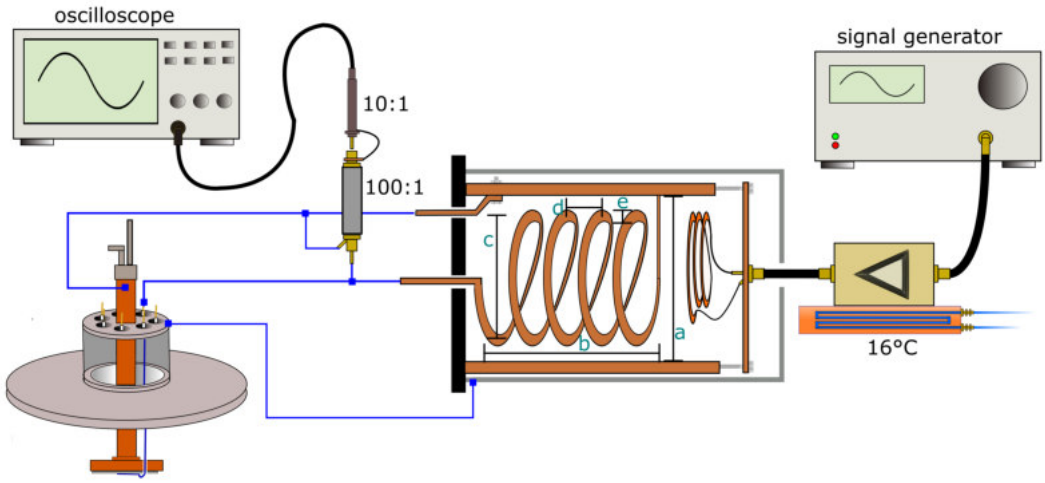

Figure 3.15: *schematics of the RF drive and helical resonator with the dimensions* $a = 8.6$ *cm,* $b = 7.1$ *cm,* $c = 4.7$ *cm,* $d = 1.19$ *cm,* $e = 0.6$ *cm. The RF signal from the signal generator is coupled to the helical resonator inductively.*

The key part to supply a high voltage in the RF regime for the trapping potential is a helical resonator made of copper with the dimensions as shown in fig. 3.15. It resides within a shielding aluminium housing and has a resonance frequency of 84.2 MHz without load. The helical resonator is connected to the RF electrodes of trap chip via an RF feed-through in the DN75 CF flange, which supports the copper pipe for water-cooling. The ground of the resonator is connected to the copper pipe and the DN75 CF flange. The bare trap without any auxiliary electronics has a capacitance around 70 pF, measured from the RF feed-through to the water-cooling pipe, which serves as ground feed-through at the same time - due to its wall thickness and robust contact to the chamber. Together, the helical resonator and the trap have a resonance frequency around 28-35 MHz, depending on the precise total setup and cable guiding. For most experiments we worked at 31.5 MHz, with a typical peak to peak RF amplitude of 80 to 120 V_{pp}. The source for the RF signal is a SMB100A signal generator[32]. Its output is further amplified by a ZHL-5W-1[33] and then coupled into the helical resonator inductively. The ZHL-5W-1 amplifier comprises a heat sink, that is integrated into the 16°C water-cooling loop mentioned earlier to improve amplitude stability. The output of the helical resonator is tapped

[32]Rhode & Schwarz GmbH & Co. KG
[33]Mini-Circuits

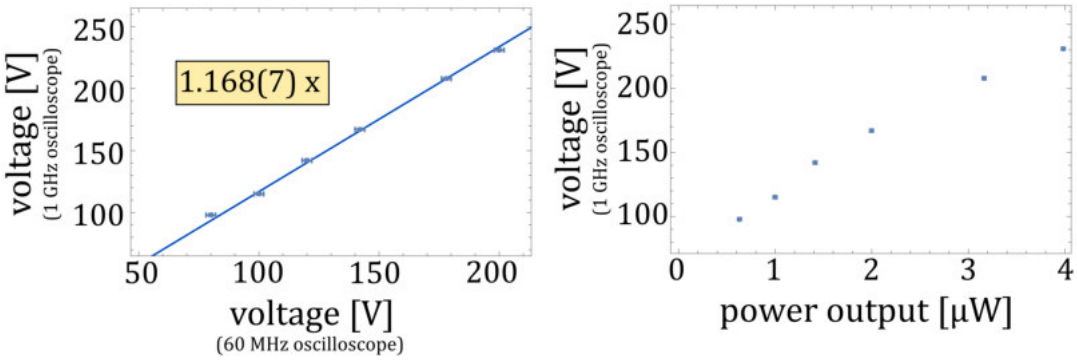

Figure 3.16: ***left:*** *measured RF trap drive amplitude with different bandwidths of the oscilloscopes.* ***right:*** *achieved RF trap drive amplitude versus the output power of the signal generator.*

with a capacitor voltage divider with ratio of 104.6(2):1 and a measuring probe with ratio 10:1 and monitored on an oscilloscope[34]. The measured absolute value of the RF signal is biased by the oscilloscope's limited bandwidth of 60 MHz, but the value is rarely needed. A corrective term for the absolute value has been measured with an oscilloscope with a 1 GHz bandwidth, see fig. 3.16.

3.5.2 DC Supply

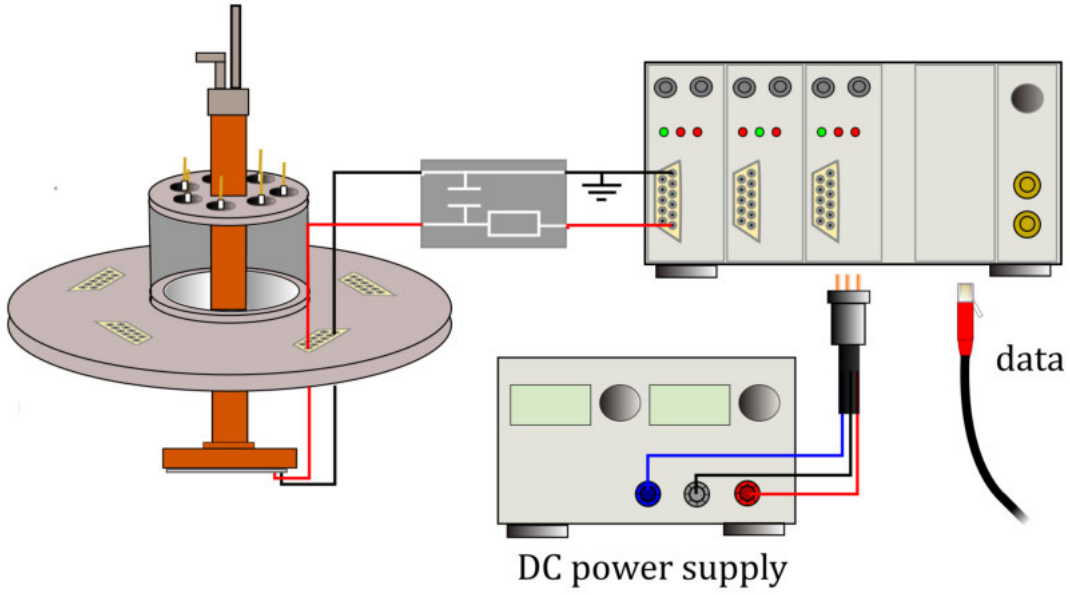

Figure 3.17: *schematics of the DC setup. Details see text.*

The segments of the trap are connected to a DC converter developed in this group. It is based on a high speed, low noise digital analogue converter controlled by a field programmable gate array (FPGA), which also provides 30 digital output signals for transistor-transistor-logic (TTL). The actual power is provided by a standard DC power supply[35]. Communication with a personal computer is realised via

[34] TDS1002B, Tektronix, Inc.
[35] type 2225, Statron Gerätetechnik GmbH

Ethernet protocol. For a more detailed overview see [Zie12, sec. 2.4]. It provides voltages for all 19 DC electrodes with a range from -10 V to +10 V at a resolution of 0.3 mV, which can be updated with 1250 MS/s. Before feeding the DC signals into the chamber, they have to go through an external low pass filter, additionally to the one integrated on the filter board (sec. 3.2). Since fast changes of the trap potentials were not needed, for most applications we chose a RC-circuit with 13 kΩ and 136 µF leading to a cut-off frequency of 85 Hz.

3.5.3 Static and HF Current System

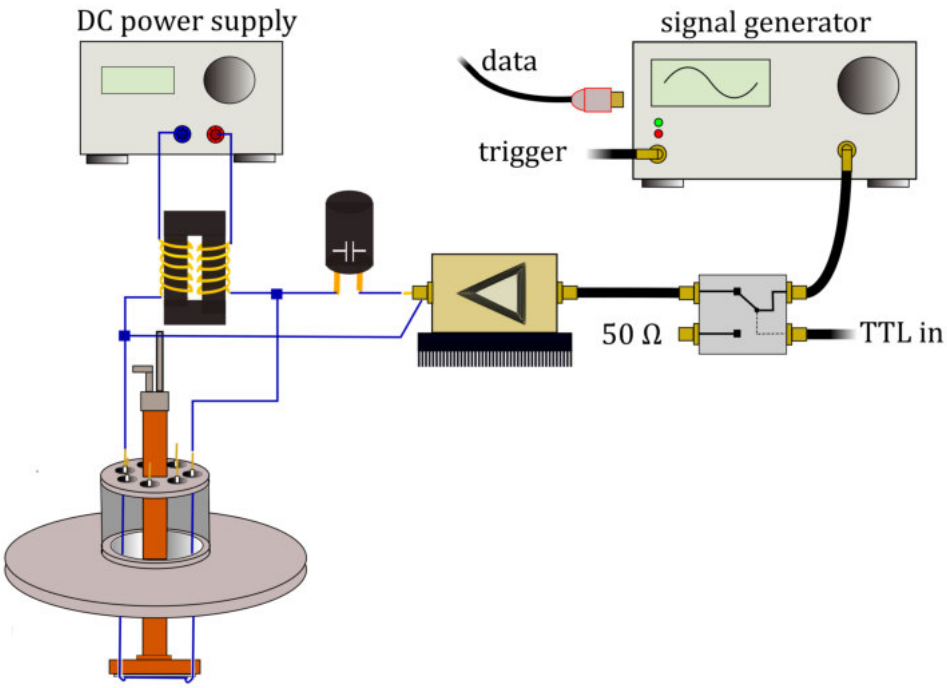

Figure 3.18: *schematics of the HF and static current setup for one of the three current carrying wires. Details see text.*

The three wires to create the magnetic field gradient are each supplied by a DC power source[36], to which they are connected via an additional common mode choke with an inductance of 1000 µH. The feed-throughs[37] can withstand static currents up to 27 A and the in-vacuum cables[38] have a diameter of 2 mm to carry currents up to 20 A. Due to the stiffness of the cables and to avoid breaking them away from the solder pads of the filter board, the feed-throughs have been put on the DN75 CF flange atop the flex bellow, see fig. 3.18.

The wires are also used to feed in HF signals needed during the experiments. This was a later development of the setup. The feed-throughs and the in-vacuum cables are actually not designed to transmit signals in the HF regime, making the incoming power needlessly frequency dependent. During this work we used two devices to generate the HF signal depending on the application: the SMB100A

[36] E3633A power supply, Keysight Technologies
[37] 9791-08-W, Hositrad Vacuum Technology
[38] KAP-L-200, VACOM Vakuum Komponenten & Messtechnik GmbH

Signal Generator[39] for a higher power output and the VFG-150[40] for faster switching between different frequencies. The output of the signal generator is connected to a switch[41] enforcing the correct pulse length. The HF signal is amplified[42] and then coupled onto the DC signal right after the choke with an electrolytic capacitor of capacitance 10 mF.

3.6 Control

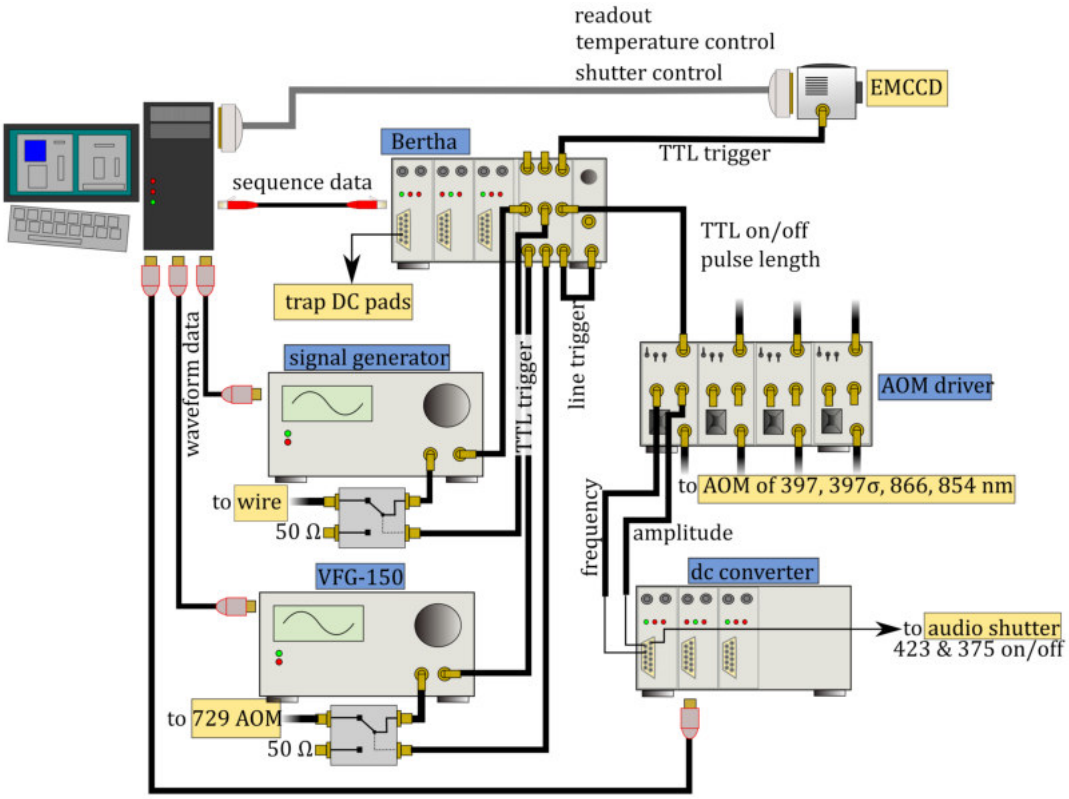

Figure 3.19: *schematics of the experimental data flow. Blue boxes mark devices used as signal sources or processing units. Yellow boxes indicate to where the signals are sent. The type of data and purpose is written next to the signal lines.*

Trapping an ion can be done by manually controlling all the devices mentioned above. For a meaningful experiment though, laser and HF pulses, trap potential changes and read-out of the qubit's state have to be synchronised with a sub µs precision. This feat is done by a device ("Bertha") developed in this group with a field programmable gate array (FPGA) as its heart. Details can be found in [Zie12, sec. 2.4]. Its outputs are divided into two groups: one is used to control the trap potentials via DACs, see ch. 3.5.2, the second group provides 30 digital channels. 28 of these are used to trigger/gate other devices via TTL signals during an experimental sequence, two can be used to trigger the FPGA, e.g. to synchronise an experiment with the power line or the RF drive. In this way the Bertha controls:

[39] Rhode & Schwarz GmbH & Co. KG
[40] TOPTICA Photonics AG
[41] ZYSW-2-50DR, Mini-Circuits
[42] ZHL-3A, Mini-Circuits

the EMCCD, the pulse length of 397 nm, 866 nm, 854 nm and 729 nm light and the pulse length of HF signals to the wires. An overview can be seen in fig. 3.19.

Analogue outputs that are not going inside the vacuum chamber and signals that are not needed within a sequence are governed by a DC converter - an older prototype of the Bertha. Communication is ensured via USB[43]. The mechanical shutters for the photo-ionisation lasers are controlled this way, since they are only needed during the loading of an ion. The power and frequency of the Doppler and re-pump lasers are usually optimised before an experimental sequence. They are adjusted by the AOMs in the beam path. The according driver accepts two analogue inputs for this purpose.

Experiments are planed at a personal computer (PC), using a software comprising two parts: a framework handling communication with the external devices and setting up a stage for the second part - a script-file used to program experimental sequences.

A second PC is used to adjust the frequency locking parameters of the lasers, as well as monitoring their modes and wavelength. Also, a control for setting a length of the cavity by means of piezo elements and the power settings for the 375 nm laser is implemented on the second PC.

The following parameters are only changed manually at the according devices: Amplitude and frequency of the RF drive, the oven current, the static currents for the magnetic field gradient, the wavelength and power of the 423 nm laser.

[43]FT2232H, Future Technology Devices International Ltd.

Chapter 4

Preliminary Measurements

4.1 Tools of the Trade

In this chapter measurements are presented, that characterise the ion trap and the performance of the general setup. The discussed topics cover the loading of ions, achievable trap frequencies and efficiency of Doppler cooling, as well as basic spectroscopy.

4.1.1 Trapping of Ions and Trap Frequencies

Loading of ions into the trap with the parameters given in the last chapter, usually works within 10-20 sec. If Doppler cooled, they stay for up to 30 min within the trap, before getting lost. We were able to trap up to 16-ion crystals. However, in crystals that are bigger than five ions, a loss of at least one ion often happens after only a few minutes.

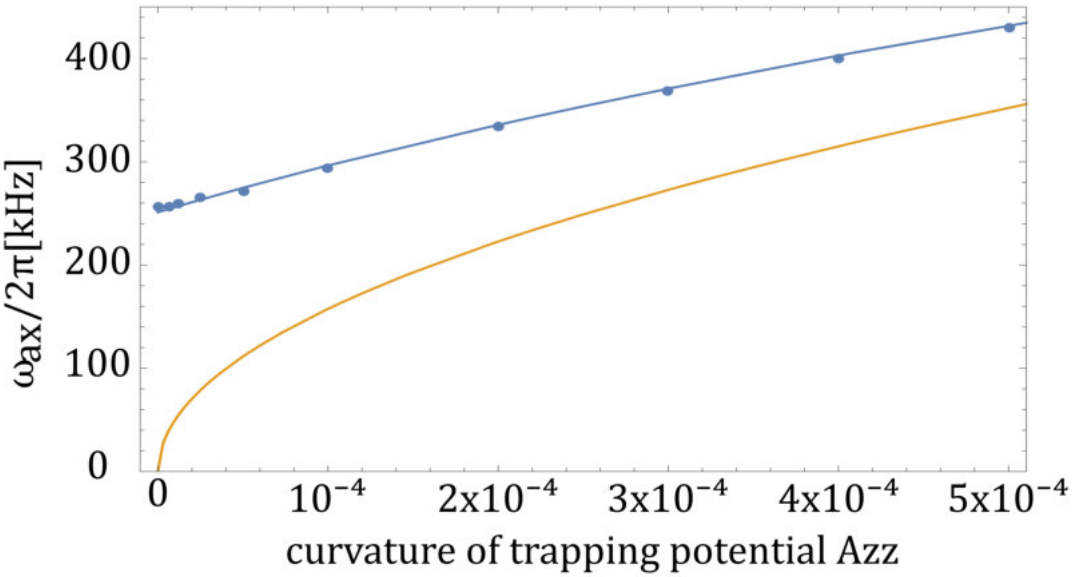

Figure 4.1: *Axial trap frequency measured by electrical excitation (blue) for different DC voltage settings, which were calculated for a given curvature A_{zz}. The orange curve comprises theoretical values for the axial trap frequency.*

For an amplitude of the RF drive $V_{\mathrm{RF}} = 225\ V$ at a frequency of Ω_D =31.6 MHz, we get an axial confinement of $2\pi \times 423$ kHz and a radial confinement of $2\pi \times 4.66$ and 4.80 MHz. The radial confinement was measured by side band spectroscopy of the $S_{1/2} \leftrightarrow D_{5/2}$ transition. Since the 729 nm laser beam for said spectroscopy is perpendicular to the trap axis, there are no axial side bands in the spectrum. The axial trap frequency can be found by electrically exciting the motion of the ion till the amplitude of the motion is strong enough to be seen on the camera. For an excitation of a motion of the ion with the axial trap frequency, an AC signal was put on one of the DC electrodes at low amplitude. The frequency of the AC signal was swept across the expected trap frequency until an excitation occurred. Since a sampling rate of the camera is much slower than the oscillation, the image of the ion blurs along the respective axis as soon as the exciting frequency hits one of the trap frequencies.

Figure 4.1 shows the measured axial trap frequency versus the desired curvature A_{zz} of the trapping potential along the trap axis. The desired curvature A_{zz} determines the DC voltages that were applied to the DC electrodes according to eq. (2.15). Usually, only five of the nine pairs of electrodes were used to create the axial confinement.

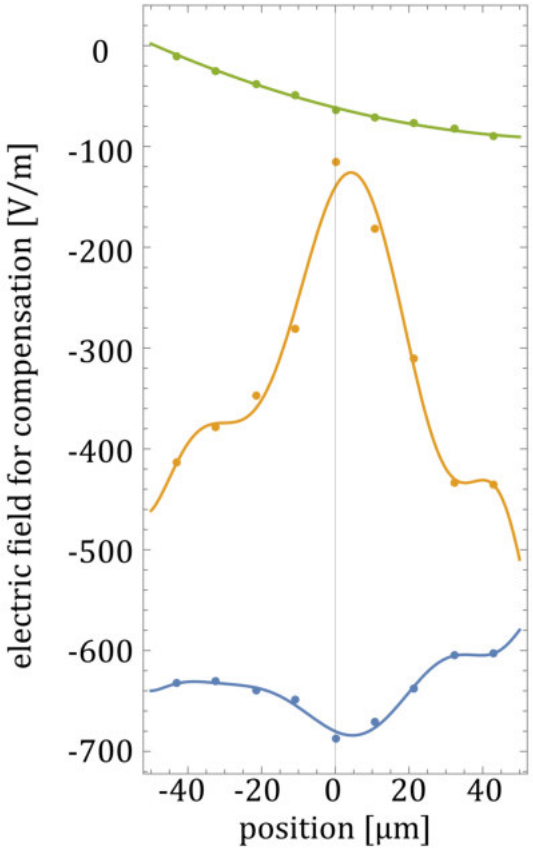

Figure 4.2: *Electrical fields necessary to compensate for stray fields in dependence of the position along the trap axis. Green: electrical field component in axial direction. Orange: electrical field component in lateral direction. Blue: electrical field component along the trap height.*

The other DC electrodes were prespecified to 0 V. There is a gap between the measured values and the theoretical prediction $\frac{\Omega_D}{2}\sqrt{A_{zz}}$, see eq. (2.7). In fact, even for no DC voltages at all, we have a confinement of about 255 kHz, which relates to an additional curvature of $A_{zz} \approx 2.5 \times 10^{-4}$.

With increasing curvature the ion moves along the axis, with decreasing amplitude per step. With a maximum of 10 V per DC segment, we can achieve a curvature of about 5×10^{-3} and an axial frequency of $2\pi \times 1.1$ MHz. For this, the movement is below the resolution of the camera of roughly one micrometer. We define this position as the centre of the trap. Based on this, we changed the constraints for the electrical field, c.f. eq. (2.13), at this new trap centre in such a way that the ion does not move anymore upon changing the curvature. We repeated this procedure for different positions along the trap axis. The results are shown in fig. 4.2. This measurement was made with $V_{\mathrm{RF}} = 122\ V$ and Ω_D =31.5 MHz. We need an electrical field of -61.5 V/m to hold the ion in the (geometrical) trap centre. We found a vanishing point for the electrical field

at a position $z = -48.8$ µm away from the trap centre, where the ion is trapped even without an external DC voltages supplied to any DC electrode. At each point along the axis the ion was compensated in the x and y direction, i.e. the ion was moved in this direction, till the fluorescence was at a minimum. If the ion is not in the RF node, it will undergo excessive micro motion and thus broaden the resonance curve of the $S_{1/2} \leftrightarrow P_{1/2}$ transition, resulting in a brighter image of the ion. The values needed for compensation are also shown in fig. 4.2. These deviations from the theoretical values are due to electrical stray fields, that origin either in residues on the trap surface or from charging the trap chip with the photo ionisation lasers. The mentioned values vary on a daily basis around 10 %.

4.1.2 Doppler Cooling

In Doppler cooling the cooling rate is directly proportional to the line width Γ of the used transition and works most efficient for a detuning of the laser frequency of $\Gamma/2$ [Roo00]. We cool for 8 ms, which is longer than necessary in order for the camera to finish its preparation and readout-cycle. The figure below shows the residual mean phonon number of a thermal distribution after Doppler cooling at a trap frequency of $2\pi \times 3.4$ MHz for different power settings of the laser. For each power level, the

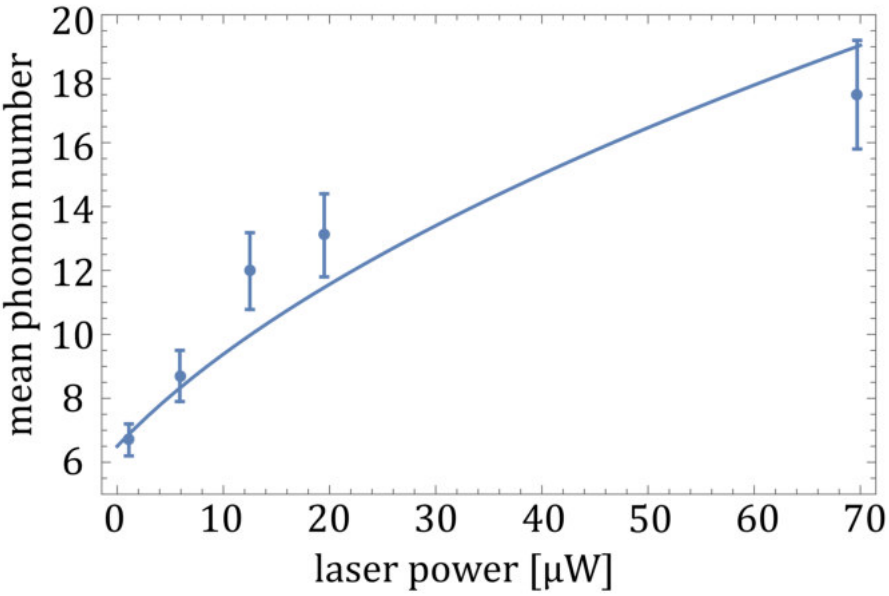

Figure 4.3: *Efficiency of Doppler cooling dependent on the incoming laser power. The power was measured in front of the viewport, where the laser enters the vacuum chamber.*

detuning was adjusted to yield half of the maximum possible fluorescence. To infer the mean phonon number $\bar{n}$, we relied on the weak dependence of the carrier of the $S_{1/2} \leftrightarrow D_{5/2}$ transition on the phonon number, see eq. (2.29):

$$p_{D_{5/2}} = \sum_n p_n^{\text{therm}}(\bar{n}) \text{Sin}^2 \left[\frac{\Omega_0}{2}(1 - \eta^2 n)t \right] \tag{4.1}$$

Examples for this time evolution can be seen in fig. 4.4. Since the lowest phonon number achievable with Doppler cooling is proportional to the line width [WDW78]

and the power is proportional to the saturation S with $\Gamma[S] = \Gamma_0\sqrt{1+S}$ [Cit+77], we find $\bar{n} = 6.5\sqrt{1+0.11P}$ by interpolation. This gives us a saturation of the $S_{1/2} \leftrightarrow P_{1/2}$ of $S = 1$ for about $P = 9$ µW. Usually, we cool with a power around 10-15 µW, which also achieves sufficient fluorescence for state discrimination in the detection phase.

Heating Rate

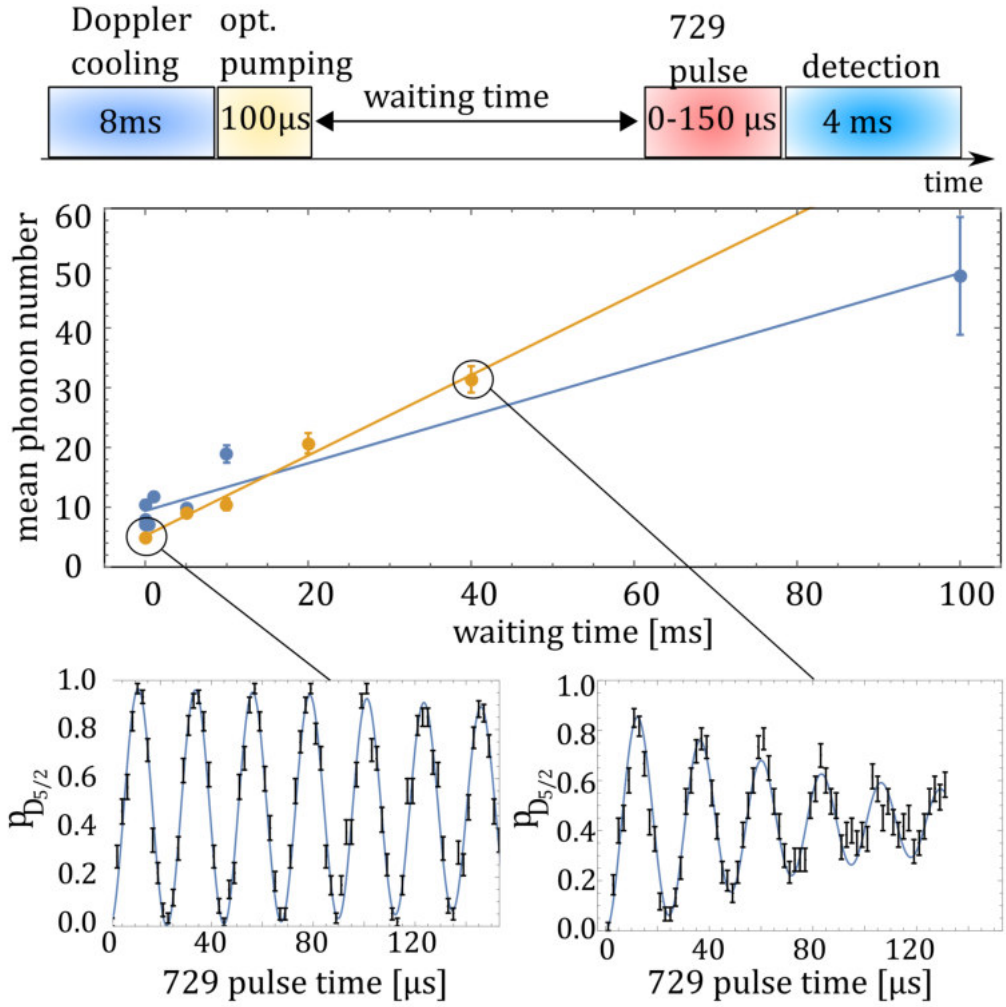

Figure 4.4: ***top:*** *sequence for measuring the heating rate* ***center:*** *mean phonon number after an increasing waiting time. orange and blue indicate two different measurement series on different days.* ***bottom:*** *time evolution for* $\bar{n} = 4.9$ *(left) and for* $\bar{n} = 31.4$ *(right).*

Diverse processes lead to an excitation of the motional modes over time. This behaviour is not fully understood. One of the main suspects are carbon residues on the trap, leading to long ranged dipole interactions that scale with the distance to the fourth power [Hit+12]. Independent of the source, their effect is condensed to the so called *heating rate*, which is the acquired phonons of the ion per time interval, usually normalised with the trapping frequency. Since the Rabi frequencies depend on the phonon number, a significant increase during a sequence of gate processes is undesirable. For a characterisation, the ions are Doppler cooled and initialised.

After a waiting time the dynamic of the $S_{1/2} \leftrightarrow D_{5/2}$ transition is measured and the mean phonon number inferred, see fig. 4.4.

Shortly after the cooling, we see Rabi oscillation with virtually full amplitude (left plot). For increasing waiting times, the phonon distribution flattens out, c.f. sec. 2.1.4, leading to a wider variety of Rabi frequencies and a fast dephasing (right plot). The measurements from two different days lead to the fits: $\bar{n} = 5.2 + 0.7/s$ and $\bar{n} = 9.4 + 0.4/s$. Evaluating the carrier transition is a relative coarse way to measure the mean phonon number, especially for small amounts, as can be seen at the variances for small waiting times. A comparison of the dynamics of the red and blue side band would produce more precise results. However, for a ball park figure the trap has at least less than one phonon per millisecond as a heating rate at typical trapping parameters as given in sec. 4.1.1. This is sufficiently stable for our purposes, since the J-type spin-spin coupling eq. (2.61) is independent of the mean phonon number.

4.1.3 729 nm Spectroscopy

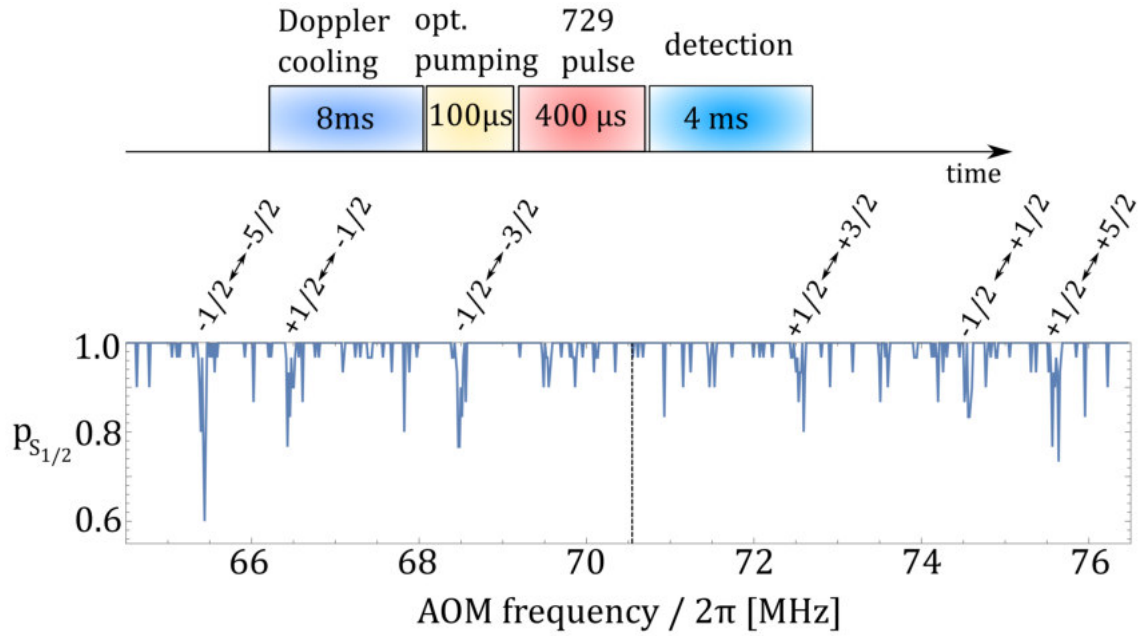

Figure 4.5: ***top:*** *sequence for 729 nm spectroscopy.* ***bottom:*** *spectrum of the $S_{1/2} \leftrightarrow D_{5/2}$ transition for a magnetic field along the trap axis and perpendicular to the laser beam, created by 1 A. The dashed line indicates the point, where the transitions would be for a zero magnetic field. Since the light passes the AOM twice, double the amount printed on the frequency axis is actually added to the frequency of the laser.*

Spectroscopy of the $S_{1/2} \leftrightarrow D_{5/2}$ transition is done according to the sequence shown in fig. 4.5. A pulse time of several hundred micro seconds ensures, that Rabi oscillations have already been faded out and the population is more or less stable. 729 nm spectroscopy can be used to measure trap frequencies by measuring a distance of a side band to the carrier. Furthermore, by monitoring the time evolution one can infer the mean phonon number, as mentioned in the last chapter.

Figure 4.5 shows a spectrum with no initialisation after the Doppler cooling, leading to a more or less equal population of the $|\uparrow\rangle$ and $|\downarrow\rangle$ level and a visibility of all possible transitions with the given laser-trap-arrangement. Usually, we achieve π-times between 5 and 12 µs for the carrier transitions, depending on laser power and polarisation settings.

Within a magnetic field, the atomic levels are shifted due to the Zeeman effect by $\Delta\omega = \Delta m g_j \mu_B B/\hbar$. A transition between a level (1) and a level (2) is then shifted by

$$\Delta\omega^{(1)} + \Delta\omega^{(2)} = (\Delta m^{(1)} g_j^{(1)} + \Delta m^{(2)} g_j^{(2)}) \frac{\mu_B}{\hbar} B \tag{4.2}$$

For the transitions shown in fig. 4.5 the total shift is from left to right:
$\Delta\omega = \left(-\frac{10}{5}, -\frac{8}{5}, -\frac{4}{5}, \frac{4}{5}, \frac{8}{5}, \frac{10}{5}\right) \frac{\mu_B}{\hbar} B$. Since the frequency for a zero magnetic field depends on the laser frequency, it can shift on a daily basis. Therefore, at least two transitions are necessary to discern the total shift caused by the magnetic field. A

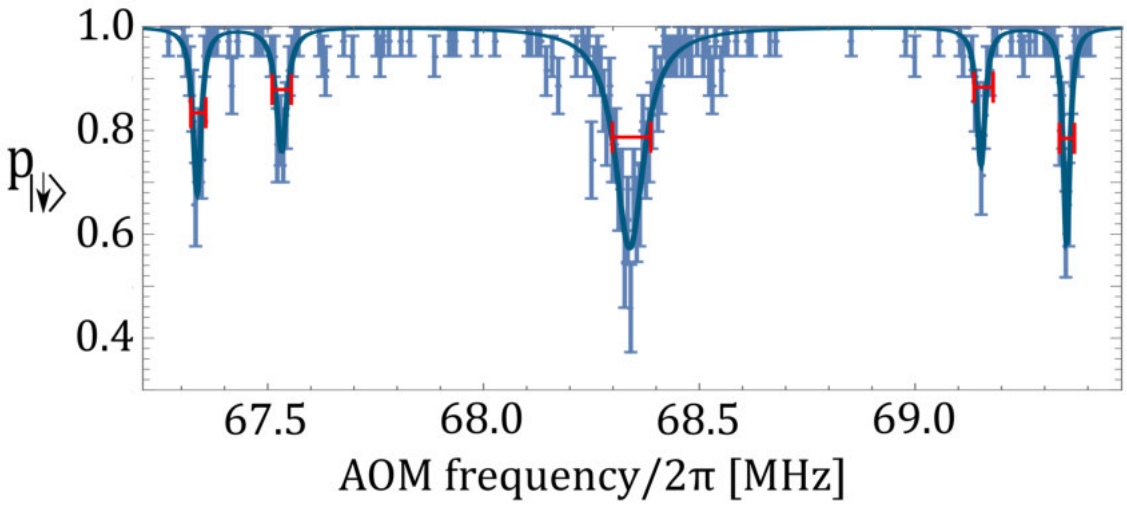

Figure 4.6: *Spectrum of the* $|\downarrow\rangle \leftrightarrow D_{5/2}$ *transition with blue and red radial side bands of* $2\pi \times 2.01$ *MHz and* $2\pi \times 1.62$ *MHz. The red bars indicate the full-width-half-maximum.*

spectrum of the $|\downarrow\rangle \leftrightarrow \mathrm{D}_{5/2}(m = -3/2)$ transition with a higher resolution is shown in fig. 4.6. It features both radial side bands. Since the 729 nm laser beam is close to perpendicular to the trap axis, axial sidebands can usually not be observed. The carrier usually has a line width of about $2\pi \times 140..180$ kHz, while the line width of the side bands is between $2\pi \times 30..60$ kHz. The centre frequency of the side bands varies from measurement to measurement usually less than $2\pi \times 10$ kHz.

4.1.4 Basic HF Spectroscopy without Magnetic Field Gradient

For the $|\uparrow\rangle \leftrightarrow |\downarrow\rangle$ transition the splitting due to a magnetic field is $\omega = 2\mu_B B/\hbar$. With an oscillating current in one of the wires beneath the chip, we can drive this transition. Figure 4.7 shows a spectrum of the splitting for a pulse time of 1.7 µs and a spin resonance of $2\pi \times 12.7$ MHz. Due to the negligible Lamb-Dicke factor, the Rabi frequency is virtually independent of the phonon number, leading to Rabi

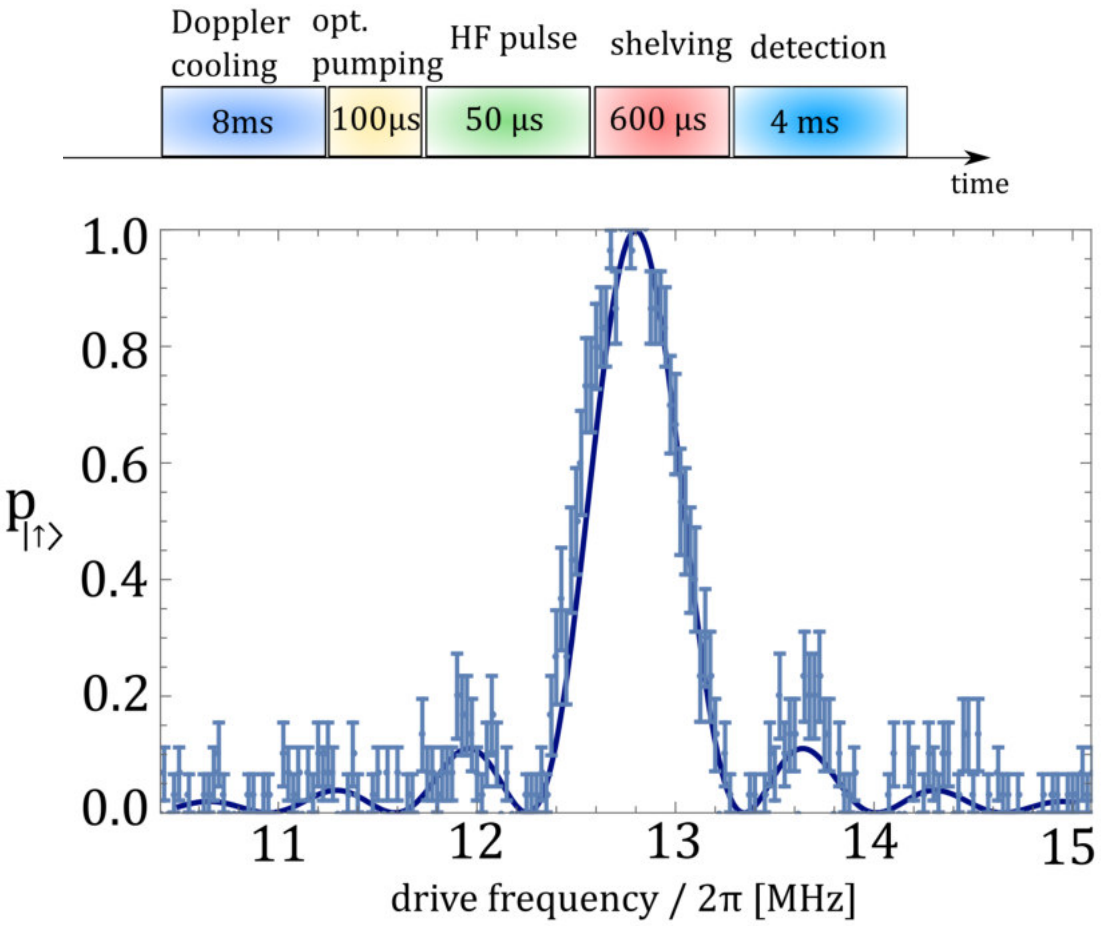

Figure 4.7: ***top:*** *sequence for HF spectroscopy,* ***bottom:*** *HF carrier for a pulse time of 1.7 µs and an output power of 0.06 mW of the signal generator.*

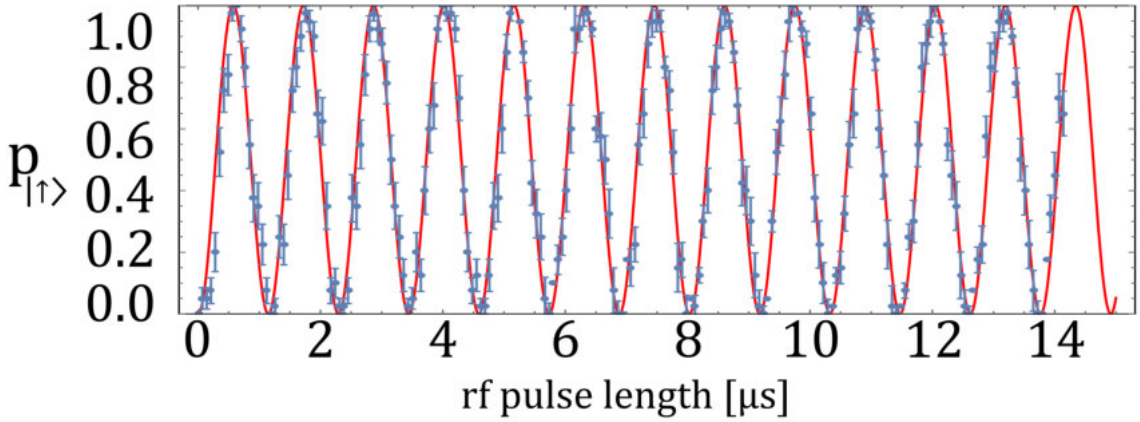

Figure 4.8: *Rabi oscillations on the HF carrier for an output power of 0.4 mW of the signal generator.*

oscillations without dephasing even for only moderately cool ions, see fig. 4.8. This also makes a suited HF pulse length for a spectrum somewhat arbitrary.

In fig. 4.9, spectra for different input powers are combined to a density plot, showing off-resonant Rabi oscillations according to eq. (2.33). For positive detuning

we have a greater deviation from the theoretical values. We attribute this due to a frequency dependency of the incoming power, see fig. 4.10. Upon shifting the spin resonance with the external field and otherwise same parameters, the achieved Rabi frequency varies around ±6 %.

An additional feature at a detuning of about $+2\pi\times1.5$ MHz can be seen (red). This peak is independent of the external magnetic field and presumably a non-linear resonance of the trap [Alh+96]. These have been a major problem in a previous version of the trap, see also sec. 2.4. It can be seen as a success, that we now only encounter the strongest of these additional lines in the spectrum and also only for relative high power settings. A thicker metal layer on the chip may suppress them further. To avoid an overlap of this feature with a motional side band later, we decreased the carrier centre frequency from $2\pi \times 12.7$ MHz to $2\pi \times 9...10$ MHz.

Since the Rabi frequency is proportional to the magnetic field amplitude, which is directly proportional to the applied current, we expect a square root dependency of the frequency from the power. This is shown in fig. 4.11. For an output power

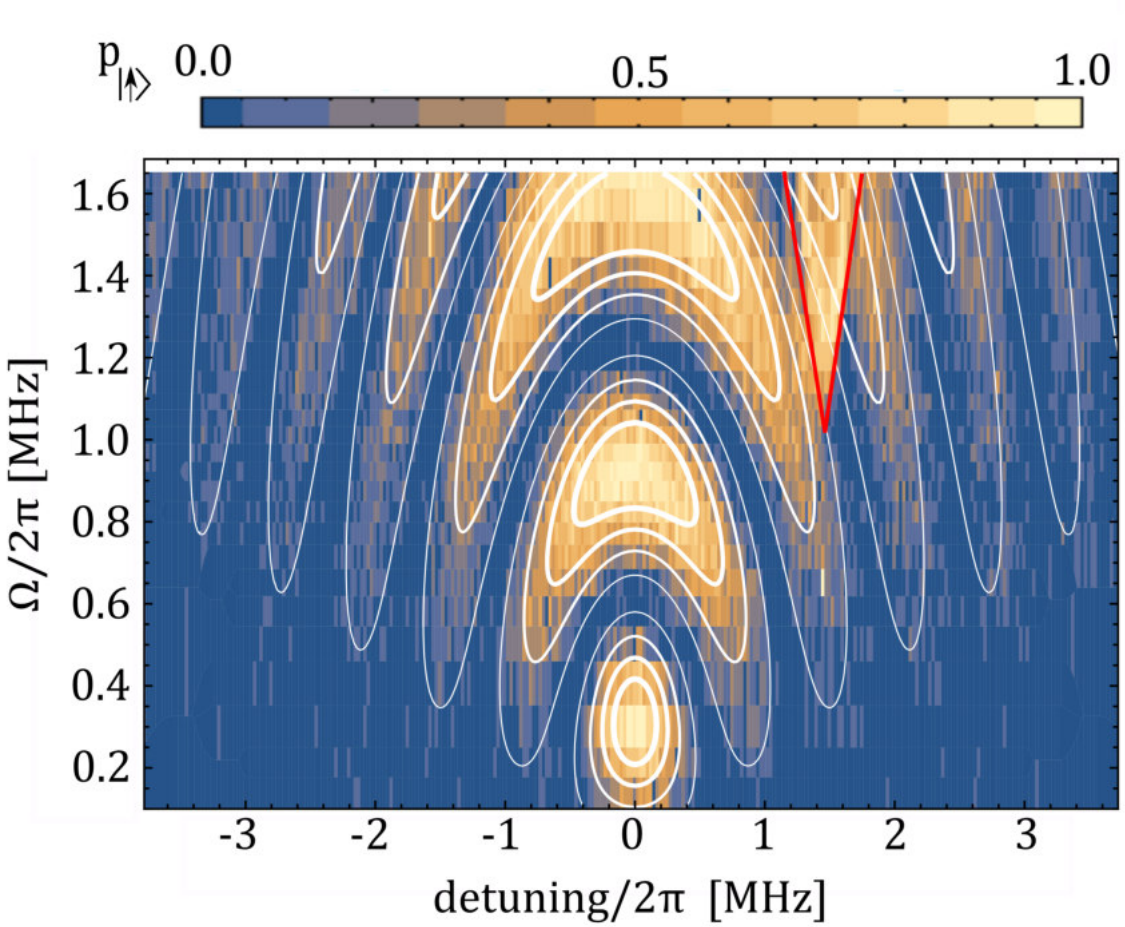

Figure 4.9: *density plot of the probability for $|\uparrow\rangle$ on the carrier transition as function of strength and detuning of the HF driving field. Each data point results for 30 independent measurements at a pulse time of $\tau = 1.7$ μs. The Rabi frequency was inferred from scans of the HF pulse length. The white contour lines are calculated with (2.33) for 5% (thin), 25%, 50% and 75% (thick) probability being in $|\uparrow\rangle$. The red triangle marks a feature which is insensitive to the external magnetic field.*

beyond 1 mW, we notice a diminished return in Rabi frequency, which we attribute to a shrinking of the amplifier's gain for higher power inputs. For up to 1 mW the relationship can be sufficiently well described by $\Omega_R/2\pi = 1.16\sqrt{P/1\text{ mW}}$ MHz.

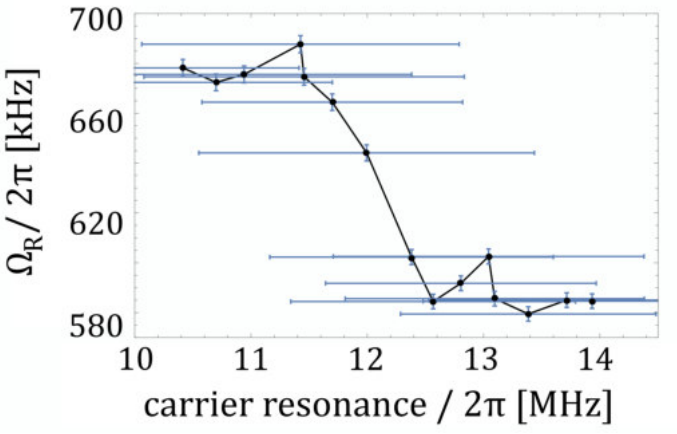

Figure 4.10: *incoming power measured as Rabi frequency versus Zeeman splitting at constant signal generator ouput power. The horizontal error bars indicate the line width of the transition.*

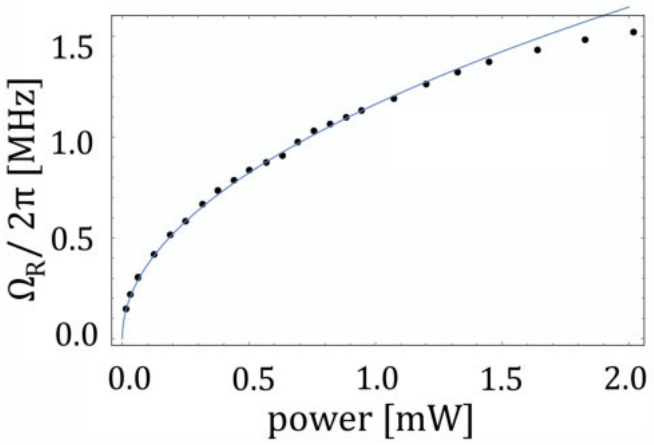

Figure 4.11: *HF Rabi frequency versus signal generator output power. The standard deviations for the Rabi frequency are in the sub-percent regime.*

4.2 Magnetic Fields and Gradient

The following section deals with the creation and characterisation of the necessary magnetic fields and gradients. To measure a magnetic field, we employed spectroscopy of the Zeeman splitting of the $S_{1/2}$ ground state of a single ion and also of the $S_{1/2} \leftrightarrow D_{5/2}$ transition. Since the ions can be moved in the trap with high precision they make an ideal field probe [Wal+11].

4.2.1 External Field

A magnetic field created by coils outside the vacuum chamber serves as a quantisation axis. By adjusting the currents in the five coils, the magnetic field can be tuned and rotated to any direction. As shown in fig. 4.12, shifts in the atomic transition frequencies are directly proportional to the applied current[1]. The frequency-current-ratio is approximately constant and can be used to calculate the absolute value of the magnetic field, which is usually between 0.3 to 0.45 mT. Extrapolation of the data shown in fig. 4.12 yields a consistent offset field of 47(3) µT. Qualitative simulations show that the magnetic field produced by the constantly running oven directs mainly along the trap axis and is therefore supposedly the source. Magnetic stray fields in the other directions where compensated before the measurement.

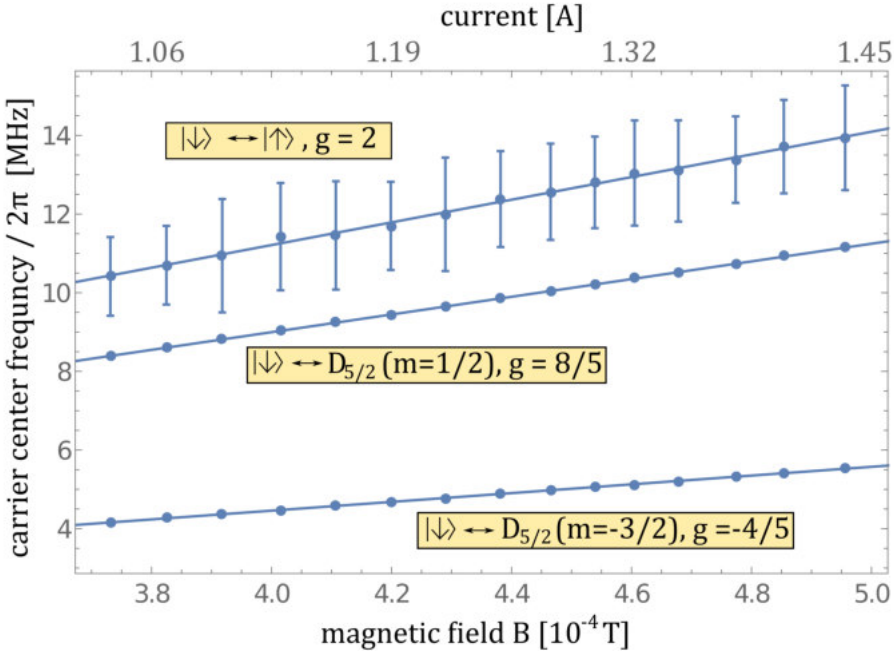

Figure 4.12: *absolute value of the shift of atomic transitions due to the external magnetic field. The errors are the full-width-half-maximum of the according peak in a spectrum. The S↔D transition errors are at the order of 30 kHz and too small to see.*

4.2.2 Current Endurance Test of the Wires and the Water-cooling.

To avoid an electrical breakdown due to excessive power dissipation, the electrical properties of the wires for the magnetic field gradient have to be investigated. Although we used the etched copper realisation for all other measurements in this work, it is worthwhile to have a short look at the performance of the wires printed with thick-film technology. On the one hand, one can see if this manufacturing method is promising enough for other applications. On the other hand, one can approximate the effectiveness of the water-cooling device.

[1] here: in the coils arranged along the trap axis

For this, the thick-film filter board with the wires was put into a vacuum testing chamber with a final pressure of 4.4×10^{-7} mBar and the whole filter board was cooled to 16 °C. The outer wires had a width of 340 µm and the inner wire 220 µ. All had a height of 40 µm and a distance of 150 µm between each other. The results are summarised in fig. 4.13. Firstly, we measured the resistance by sending a constant, relatively low current through each wire and the voltage drop from feed-through to feed-through was measured. We got the ratios $R = 175(15)$ mΩ, 370(40) mΩ and 176(13) mΩ, respectively.

To achieve a high magnetic filed gradient, each wire should withstand 20 A. To reduce the corresponding heat load, the current is pulsed. For a realistic spin-spin coupling below 1 kHz, the gradient needs to last for several milliseconds. Cooling, preparation and detection of ions can usually be done in less than 10 ms. Triggering experiments to the power line can be useful to minimise magnetic field fluctuations. Therefore, we have one measurement cycle every $t_{cyc} = 20$ ms with $t_{pls} = 10$ ms time for a current pulse.

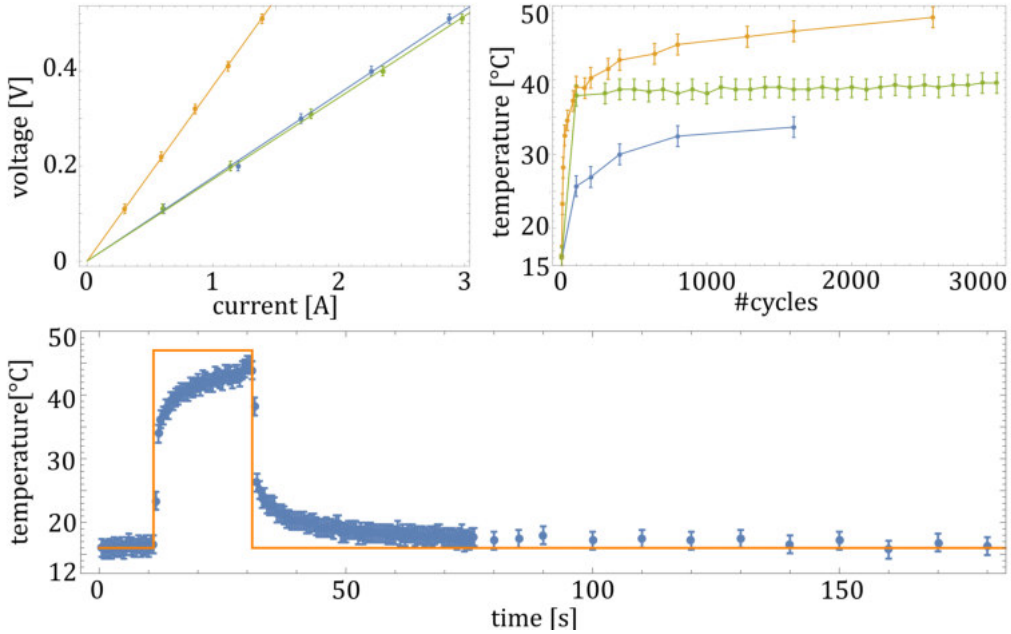

Figure 4.13: ***top left:*** *resistance of the outer wires (blue and green) and central wire (orange).* ***top right:*** *temperature after a number of cycles with 19 A, a repetition rate of 50 Hz and 50% duty cycle for one wire (blue), two wires (orange) and two wires with a 8 s pause after every 100 cycles (green).* ***bottom:*** *temperature during and after 1000 cycles with 19A with a repetition rate of 50 Hz and 50% duty cycle in two wires. The orange line indicates the time window of the cycles.*

To be on the safe side, we applied not more than $I = 19$ A and sent a number of pulses through one or both outer wires. At the same time, a constant current of 2.5 mA was sent through the central wire, while the voltage drop was monitored. Due to Joule heating of the wires with $P_J = I^2R$ the whole board is getting hotter and the resistance of all wires increases accordingly. Thus, the central wire acts as a temperature probe, where we used the weighted average of the temperature coefficient for silver and platinum $\alpha = 3.85 \times 10^{-3}/\mathrm{K}$ for scaling.

During one cycle we have an energy dissipation in one of the outer wires of $E_{cyc} = P_J \cdot t_{pls} = 0.65$ J. After a 10 ms break, the next pulse arrives. With an

increasing number of pulses, the temperature of the whole board increases as well, see fig. 4.13, top right. Therefore, the active cooling during the whole cycle isn't enough and after $n = 1000$ cycles with pulses in both outer wires we need about $t_{cool} = 110$ s to get back to 16°C, see fig. 4.13, bottom. This gives us an average $P_{cool} = n{\cdot}2E_{cyc}/(t_{cool}{+}n{\cdot}t_{cyc}) = 10$ W. For a typical measurement with an ion usually around $n = 100$ measurement cycles with the same parameters are necessary for one data point. Then parameters are changed and communication with the peripheral devices causes a pause. We can prolong this time to let the wires cool down. For two wires, we would need around $n \cdot E_{cyc}/P_{cool} - n \cdot t_{cyc} = 11$ s to get them back to 16 $°C$. For the green data series in fig. 4.13, we used a pause of 8 s and got a stable temperature of $T = 38.9(14)$ °C. With this, we can finally determine the thermal resistance of the system to $\theta = \Delta T/P_J = 1.66(21)$ K/W.

If we want to avoid a temperature increase by 50 K, we cannot dissipate energy with more than 30 W on average. Thus, the upper limit would be a continuous 6.3 A in all three wires or for pulsed currents of 20 A, a duty cycle with less than 10 %.

For the etched copper wires with a height more than three times higher than the thick-film wires, the electrical resistance is much smaller accordingly, as can be seen on the left side of fig. 4.14. We extract $R_{near} = 40.5(5)$ $m\Omega$, $R_{central} = 47.9(42)$ $m\Omega$ and $R_{far} = 43.7(20)$ $m\Omega$, where the subscripts *far* and *near* refer to the outer wires. The naming is explained in the subsequent section.

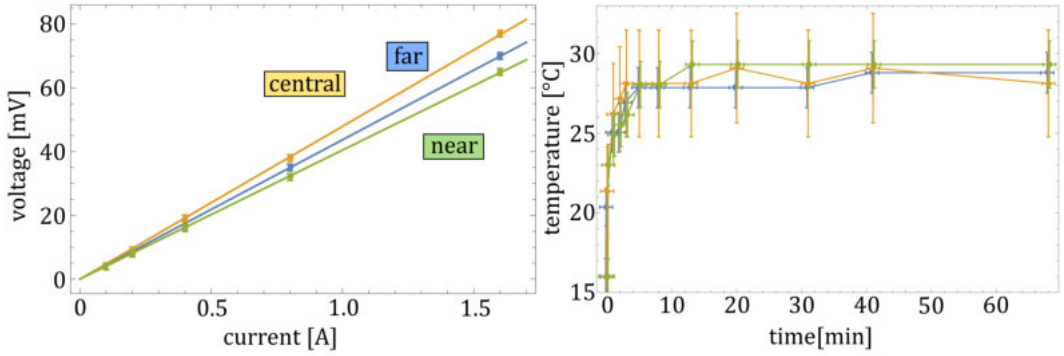

Figure 4.14: ***left:*** *resistance of the wires made from etched copper* ***right:*** *temperature increase in each wire, while sending a continuous current of 6.7 (green), 5.5 (yellow) and 9.2 A (blue) through it.*

A similar test as described above was not conclusive. In the early stage of the project, we measured resistances of 100 to 200 $m\Omega$, which mainly resulted in hindsight from plug contacts. Therefore, a change in the resistance due to increasing temperature while applying current pulses was too low to distinguish from noise. However, in a later stage, the pulsed scheme for the magnetic fields was abandoned, for reasons discussed in section 4.2.6. A magnetic field gradient was usually created with the continuous currents of (6.703, 5.500, 9.293) A. After switching the currents on, the related supply voltage was monitored. The left part of fig. 4.14 shows the result for all three wires, where we used the temperature coefficient $\alpha_{Cu} = 3.93 \times 10^{-3}/\text{K}$. We have a stable temperature of 28.5(20) °C after approximately 10 min, while dissipating with $P = 7.39(45)$ W. Therefore, we get

$$\theta = 1.69(37)\ \frac{\text{K}}{\text{W}} \tag{4.3}$$

for our cooling system, consistent with the measurements for the other wire board. Due to the smaller resistance, we could apply up to 14.7 A continuously to avoid a temperature increase of 50 K.

4.2.3 Magnetic Field of a Single Wire

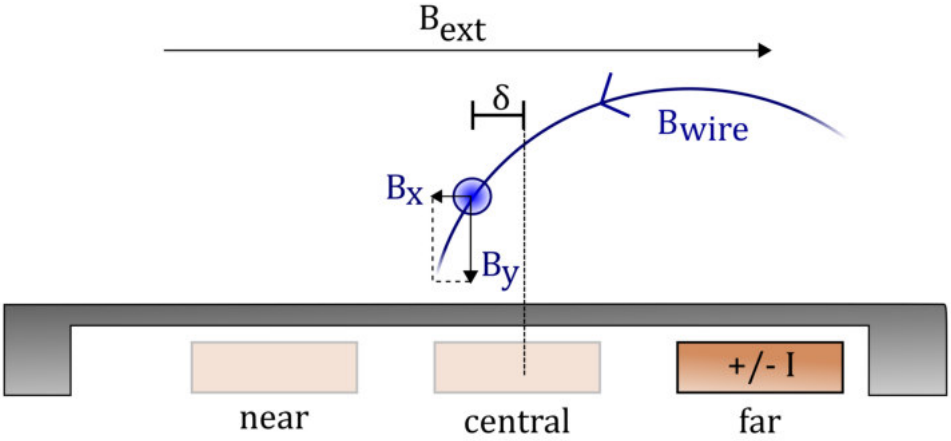

Figure 4.15: *Schematics for measurement of magnetic field of single wire. Since the trap centre shows a displacement δ in lateral direction, the ion is closer to one of the outer wires ('near wire') than to the other ('far wire').*

To create a quadrupole field at the ion's position with three wires, the magnetic field of each wire has to be inferred first. Due to their shape, it is assumed that a wire will produce no significant field along its axis $\mathbf{B} = (B_x, B_y, 0)$, leaving two unknown components in a plane perpendicular to the wire. Since the ion measures only the absolute value of the magnetic field, we do not yet have enough information, to conclude the wire's field. Therefore, we rotate the external field into this plane $\mathbf{B}_{ext} = (B_0, 0, 0)$, thus breaking the symmetry of the problem, see fig. 4.15. Now we can take two measurements, where we switch the sign of the current I producing the wire's field between both measurements, yielding:

$$B_+ = |\mathbf{B}(+I)| = \sqrt{(B_0 + B_x)^2 + B_y^2} \tag{4.4}$$

$$B_- = |\mathbf{B}(-I)| = \sqrt{(B_0 - B_x)^2 + B_y^2} \tag{4.5}$$

Thus, we obtain:

$$B_x = \pm\frac{B_+^2 - B_-^2}{4B_0} \tag{4.6}$$

$$B_y = \pm\sqrt{B_+^2 - (B_0 + B_x)^2} \tag{4.7}$$

The ambiguity of the sign is solved by the direction of the current in the wire. The results of these measurements for all three wires is shown in fig. 4.16. It shows the shift of the Zeeman splitting for several different current settings, with fits according to the eqs. (4.4) & (4.5), with $B_x = b_x I_x$ and $B_y = b_y I_y$. Firstly, we notice two different sets of measurements. For the top three data sets $B_0 \cdot B_x > 0$.

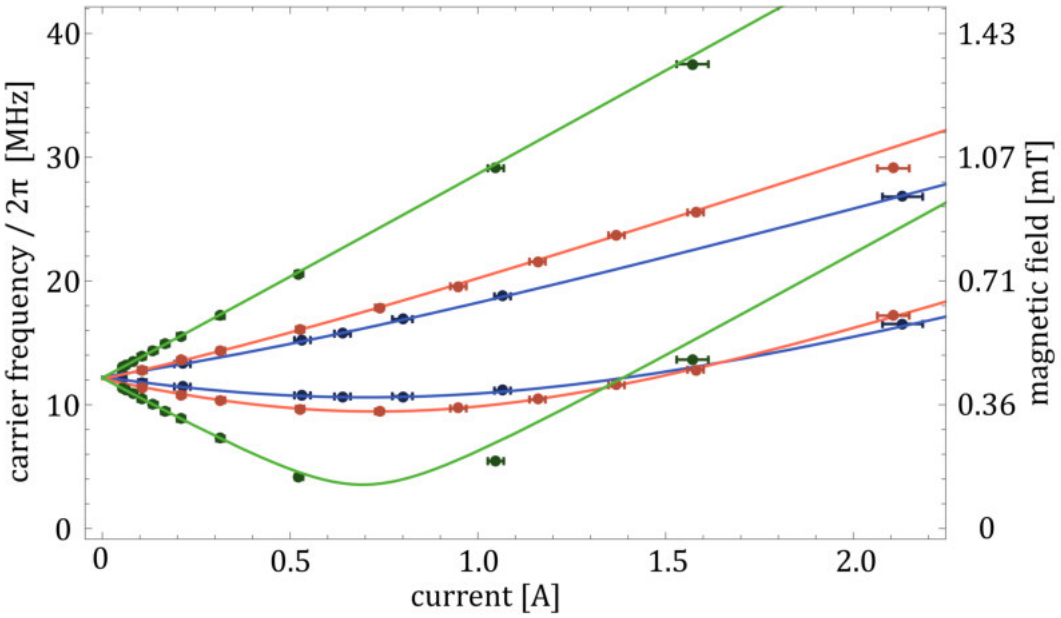

wire	b_x[μT/A]	b_y[μT/A]
far (blue)	-156	-269
central (green)	-574	-175
near (red)	-230	289

Figure 4.16: *HF carrier dependency on the absolute value of the current through a single wire. The magnetic field was calculated from the carrier frequency. The pulsed current was inferred from a voltage measurement over a shunt. The frequency error is too small too see. The table shows the fitting parameters.*

Increasing the current, increases the magnetic field linearly, where we start at the offset $B = B_0$. For the other set of three measurements, the current was inverted and $B_0 \cdot B_x < 0$. With increasing current, the respective wire starts to compensate the external magnetic field, which is heading towards a wire specific minimum $B \approx |B_y|$. Once past this point, the magnetic field of the respective wire asymptotically approach a linear form. The central wire has the closest distance to the ion and $B_y \ll B_x$, i.e. it is more or less (anti-)parallel to B_0. Therefore, it has the strongest slope and the deepest minimum. One of the outer wires has obviously a stronger influence on the ion than the other. Since they have the same dimensions, the only explanation is that the ion is closer to one of them than to the other. The wires and the trap chip are not centrally aligned, but have a small displacement δ against each other, see fig. 4.15. Therefore, we will refer to the three wires accordingly as *central* (c), *far*(f) and *near*(n) wire.

4.2.4 Nullifying Scheme

It is undesirable for the atomic transitions to move, when the wires are active to create a magnetic field gradient. Therefore, the magnetic fields of all wires should cancel each other out:

$$\sum_{i=(f,c,n)} b_x^{(i)} I^{(i)} = 0, \quad \sum_{i=(f,c,n)} b_y^{(i)} I^{(i)} = 0 \tag{4.8}$$

With the coefficients from the previous subsection, we can eliminate two variables and get:

$$I_f = -1.9243 \cdot I_c \quad (4.9)$$
$$I_n = -1.1891 \cdot I_c \quad (4.10)$$

These values serve as a starting point. At each change of the central current, the currents in the outer wires have to be adjusted. For this, the current in one wire is changed, then a spectrum is taken. If the carrier shifts to smaller values, the magnetic field has been successfully compensated a little. If the carrier shifts to higher values, the change in the current has to be reversed. With the external field along the trap-axis, we increased the current in all wires and adjusted the outer wires until we got a shift of less than $2\pi \times 200$ kHz in the $S_{1/2}$(m=-1/2)↔$D_{5/2}$(m=+1/2) transition. A shift of $2\pi \times 200$ kHz can be achieved by 195 mA in the near and by 235 mA in the far wire. The so found current settings are displayed in fig. 4.17 and the ratios between the currents are:

$$I_f = -1.6738 \cdot I_c \quad (4.11)$$
$$I_n = -1.2473 \cdot I_c \quad (4.12)$$

While the ratios for the near wire eqs. (4.10) and (4.12) can be seen as within the accuracy of the measurement, the ratios for the far wire eqs. (4.9) and (4.11) differ by 13 %.

At (8.7, 7.0, 12) A in the near, central and far wire respectively, we first noticed a shift of $2\pi \times 50$ kHz in the RF drive resonance occurring over several minutes. This

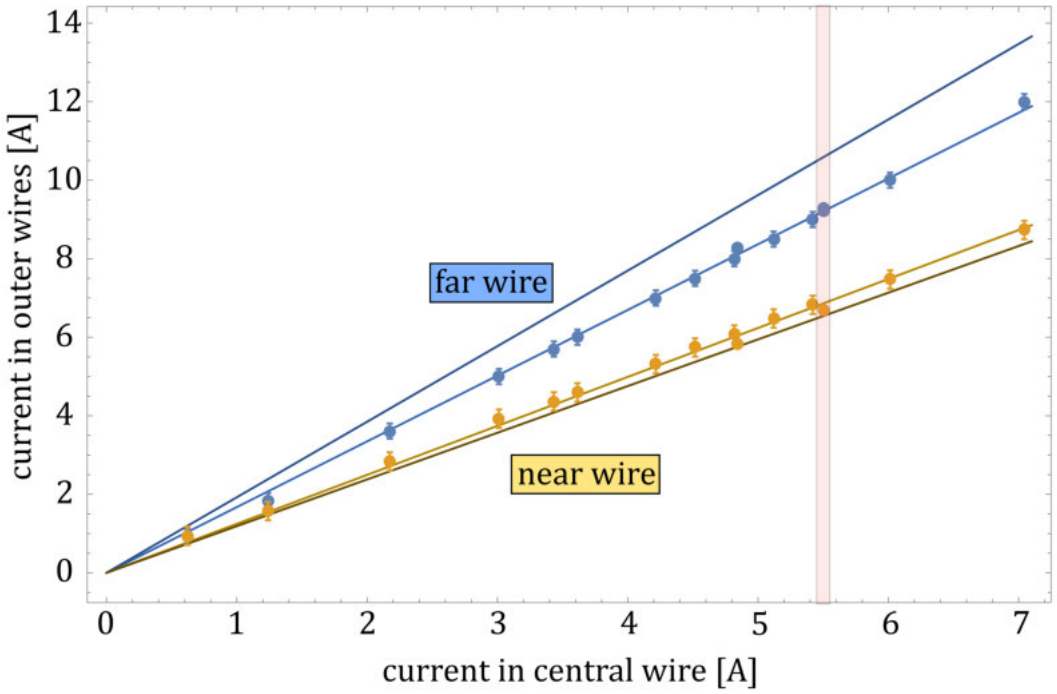

Figure 4.17: *experimentally found currents needed in far and near wire to compensate the magnetic field of the central wire. The light lines are given by eqs. (4.11) and (4.12), the darker ones by eqs. (4.9) and (4.10). The light red box marks the typical working point.*

shift is dependent on the applied current in the wires and was reproducible. Due to the time scale of minutes of the phenomenon, we associate it with the heating of the whole filter board, which also includes the RF drive supply line. With the thermal resistance eq. (4.3), we get a temperature difference of around 21 K. To avoid a change in trap frequencies, when the wires are active, we reduced the current to the setting of (6.703, 5.500, 9.293) A. These currents where found, while the external field axis was perpendicular to the trap surface. They produce a shift of less than $2\pi \times 50$ kHz in the HF carrier transition, which can be achieved by approximately 7 mA in either wire.

The asymmetric currents can be used to estimate the displacement of the wires to the trap chip. Including a displacement in eq. (2.65) yields the fig. 4.18. For the

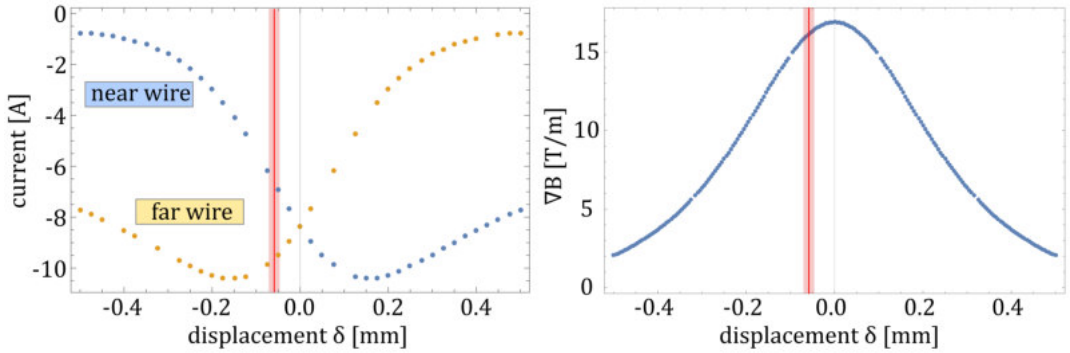

Figure 4.18: ***left:*** *calculated currents needed in the far and near wire to compensate a magnetic field of central wire due to a current of 5.500 A in dependence of the displacement of the wires.* ***right:*** *expected gradient with a displacement of the wires.*

working currents used during this work, we find a displacement of $\delta = -56(8)$ µm and with this an expected reduction of the gradient of 4(2) %.

4.2.5 Magnetic Map and Gradient

Radial Plane

Once the wires create a quadrupole field around the trap centre, we can pay attention to the gradient. To actually measure it, we displaced the ion out of the RF node by applying additional DC voltages and measured the frequency shift of the HF carrier [War+13]. The position of the ion was inferred from calculations of the new trapping potential. We usually use five neighbouring DC electrode pairs for the trapping potential, where the ion is trapped above the central pair. The resolution of the supply electronic is 0.3 mV. Applying this to both outer electrode pairs would result in a shift of the trap centre of less than 0.1 nm at a typical radial frequency of $2\pi \times 2.5$ MHz. The accuracy of the ion position is therefore probably stronger limited by changing electrical stray fields, especially after reloading.

The ion was moved in circles in the radial plane around the RF node. The plot in fig. 4.19 shows the position of the HF carrier at various ion positions without current flowing through the wires. The external magnetic field shows in the y-direction. We see variations at the order of magnitude of $2\pi \times 20$ kHz. This is consistent with slow changes of the magnetic field on the time scale of minutes seen in many measurements. The plot in fig. 4.20 shows the HF carrier position with active wires.

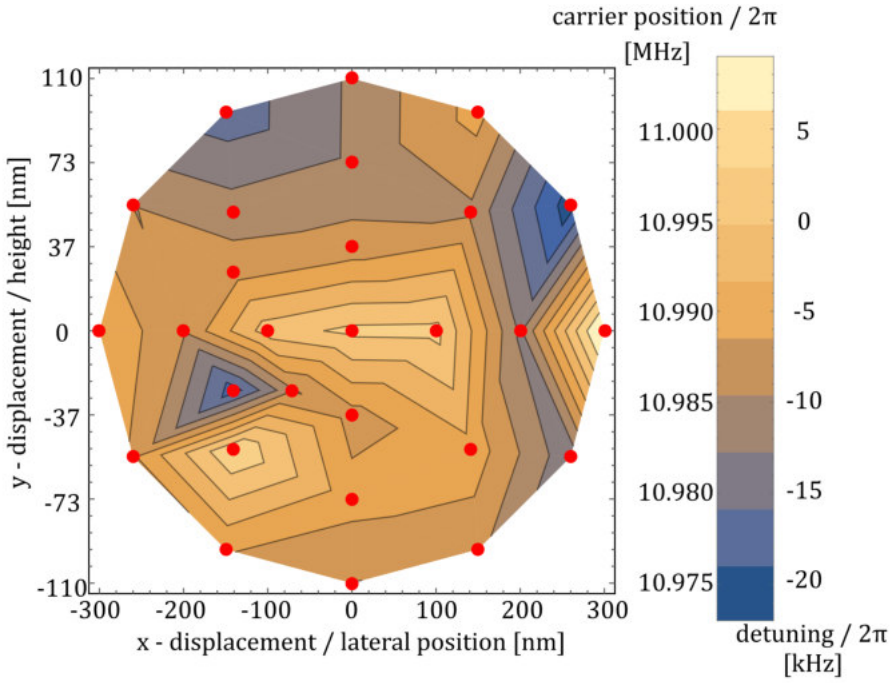

Figure 4.19: *map of the absolute value of the external magnetic field in the radial plane without magnetic field gradient. Red dots mark measuring points.*

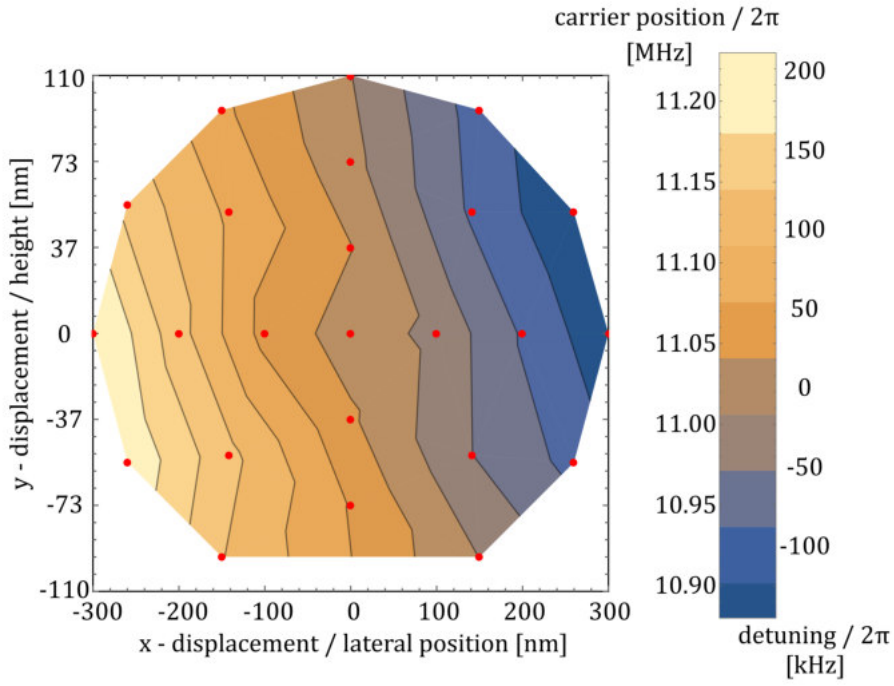

Figure 4.20: *map of the absolute value of the sum of the external magnetic field and the magnetic field gradient in the radial plane. Red dots mark measuring points.*

By fitting a magnetic field of

$$\mathbf{B} = \begin{pmatrix} 0 \\ \\ B_0 \end{pmatrix} + R(\theta) \cdot \begin{pmatrix} -b \cdot x \\ \\ b \cdot y \end{pmatrix}, \tag{4.13}$$

to the magnetic map of fig. 4.20, wherein $R(\theta)$ denotes a counter-clockwise rotation through θ, we extract a magnetic field gradient of $b = 16.3(9)$ T/m under an angle of $\theta = 12(6)^\circ$ to the surface of the trap. Errors in the frequencies have been set to the maximal variation of frequencies in the no-current magnetic map of fig. 4.19.

To see why the gradient is mainly in the lateral direction, we take a look at fig. 4.21. It shows the fields of the wire and the external coils and how they add up in theory. With the above given gradient, the quadrupole axes are tilted by -33° and 57° towards the trap surface respectively, in accordance with the asymmetrical current supply to the wires.

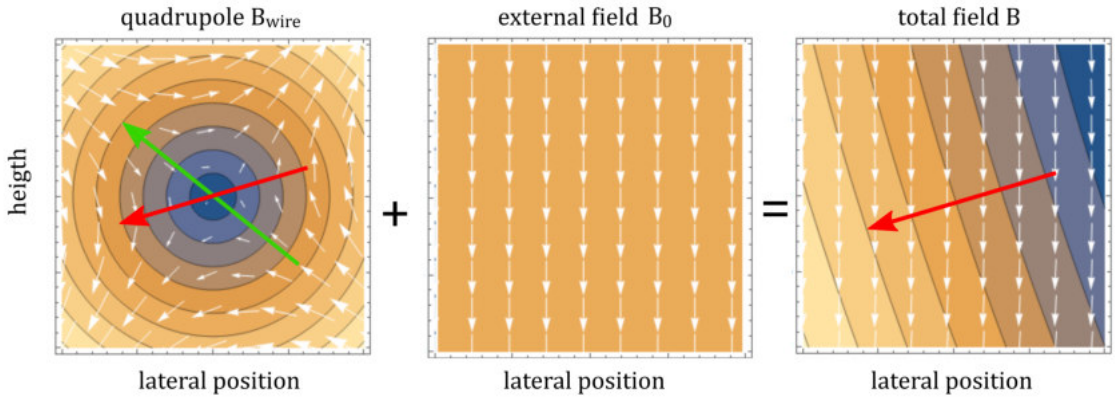

Figure 4.21: *visualisation of the magnetic field of the wires (left) and the external magnetic field (middle) and how they add up (right). In the background, the absolute value of the field is shown. The red arrow marks the gradient and the green arrow indicates one of the quadrupole axis of the magnetic field of the wires.*

Along the Trap Axis

The gradient along the trap axis can by principle be measured with a higher precision using a Ramsey scheme. For this, two ions are loaded into the trap. Then a 729 spectrum is taken to measure the magnetic field difference between both ions. To increase the resolution, the 729 pulse is divided into two parts with a waiting time in between, as depicted in fig. 4.22. Thus, the transition line shows Ramsey fringes as additional features. With the distance between the ions, that can be inferred from the axial trap frequency, we get a gradient along the axis of 0.02 T/m. However, with decreasing distance, this magnetic field differences increases, see inset, implying that the main source for the difference is caused by a small tilt of the ion crystal towards the magnetic field gradient. A displacement of 220 nm along the magnetic field gradient is sufficient to explain a shift of $2\pi \times 40$ kHz. In conclusion, we have found no clear dependency of the magnetic field to the position along the trap axis. We can merely say that the gradient is less than 0.02 T/m.

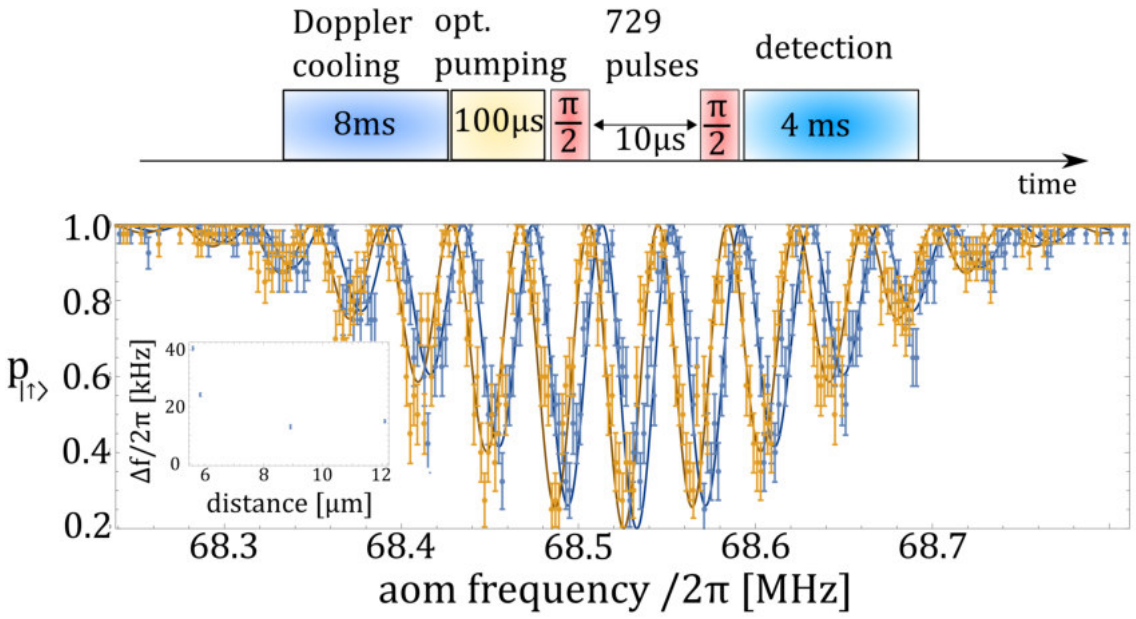

Figure 4.22: *Ramsey fringes of the* $|\downarrow\rangle \leftrightarrow D_{5/2}(m = -3/2)$ *transition for a two-ion crystal with a inter-ion distance of* 8.9 µ*m. Each colour represents one ion. Each point is the mean of 40 measurements. The inlet shows the frequency difference for four different axial trap frequencies and resulting inter-ion distances.*

4.2.6 Remanence

It was planed, to operate the etched copper wires in a pulsed scheme to minimise the heating of the system. Due to a loss in the contrast of ion fluorescence, we noticed however, that after a current pulse the atomic transition shifted far enough to have a significant loss in shelving effectiveness. Even for currents smaller than 1 A, a waiting time of several 100 µs to milliseconds was necessary before the shelving and detection could take place.

After a thorough check-up of the device sending the pulses, we finally switched to continuous currents. With this, we were able to take the plot in fig. 4.23. The HF carrier position was measured several times over an extended period of time, while switching the current completely on and off. With currents in the working setting, we have a small shift of less than $2\pi \times 50$ kHz towards the HF carrier position of the ion exposed to only the external magnetic field. When the current is switched off, the transition *instantly* shifts for more than $2\pi \times 200$ kHz. Thereafter it slowly heads back to the original value at the timescale of minutes.

Due to this remanence, a pulsed scheme was given up in this setup completely.

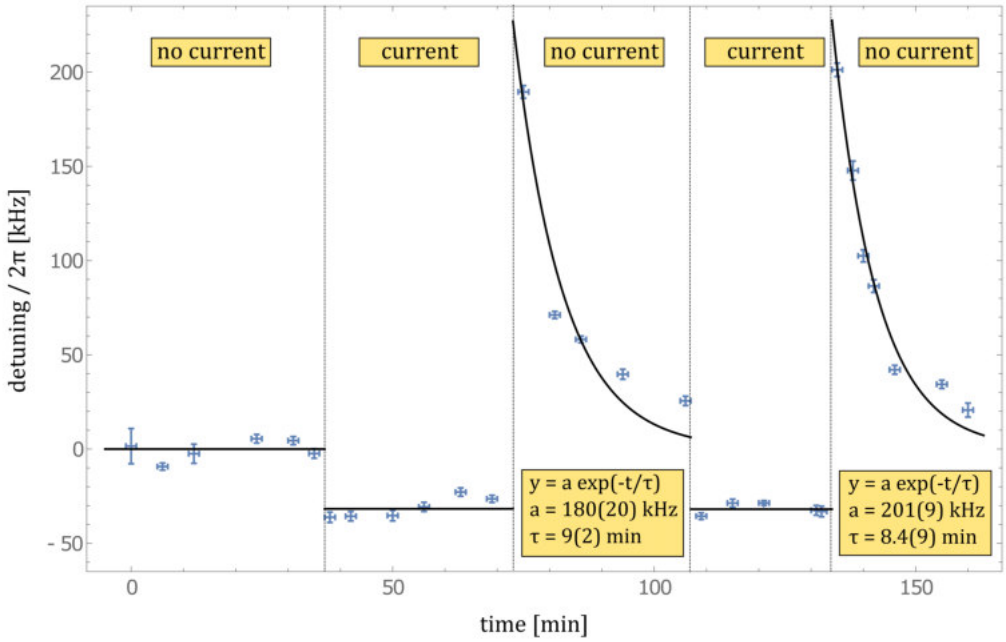

Figure 4.23: *Relative position of the* $|\downarrow\rangle \leftrightarrow |\uparrow\rangle$ *carrier, while switching the current creating the magnetic field gradient. For each data point the ion was probed 35 times.*

Chapter 5

HF Side Band Spectroscopy

5.1 Single Ion

In this section, the behaviour of a single ion within the magnetic field gradient field is investigated, starting with spectroscopy of motional side bands on the $|\downarrow\rangle \leftrightarrow |\uparrow\rangle$ transition. We will discuss the coherence time, the creation of coherent states and present measurements of the effective Lamb-Dicke factor.

5.1.1 Motional Side Bands

With the magnetic field gradient established, the coupling between internal and motional state is given by the effective Lamb-Dicke factor, see eq. (5.1). With the Zeeman splitting $\omega_a = 2\mu_B B/\hbar$ for the $|\downarrow\rangle \leftrightarrow |\uparrow\rangle$ it reads:

$$\eta = \mu_{\mathrm{B}} \nabla B \sqrt{\frac{2}{\hbar m \omega_n^3}} \tag{5.1}$$

For $\nabla B = 16$ T/m and $\omega_n = 2\pi \times 2$ MHz, we can expect up to $\eta = 1.8 \times 10^{-3}$, if the ion mode is parallel to the k-vector of the driving field and to the gradient. This is still less than the coupling on the optical S$\leftrightarrow$D transition with roughly $\eta_{SD} = 0.07$ for a comparison.

A spectrum of a single ion is shown in fig. 5.1. The $|\uparrow\rangle \leftrightarrow |\downarrow\rangle$ transition was probed with a HF pulse with a constant length of 1.75 ms. Besides the dominating carrier, the spectrum also features the red and blue motional side band of the weak radial mode with a line width of $2\pi \times 41(3)$ kHz. To verify the side band, its position was cross checked with a 729-spectrum. A more detailed scan of the red side band is shown in fig. 5.2. With a long enough HF pulse-time, we were also able to see the side band of the other radial mode, which is typically 10 times slower and has here a line width of $2\pi \times 20(2)$ kHz. In this work, we use the terms weak radial mode and x-mode as well as strong radial mode and y-mode synonymously, due to their strong alignment in these directions with a standard voltages on the DC electrodes. Since the magnetic field gradient along the trap axis is negligible, the axial side bands cannot be observed. The Rabi frequencies pertaining to the n^{th} order side bands scale with the n^{th} power of η and we do not observe an excitation on side bands of the orders $n > 1$.

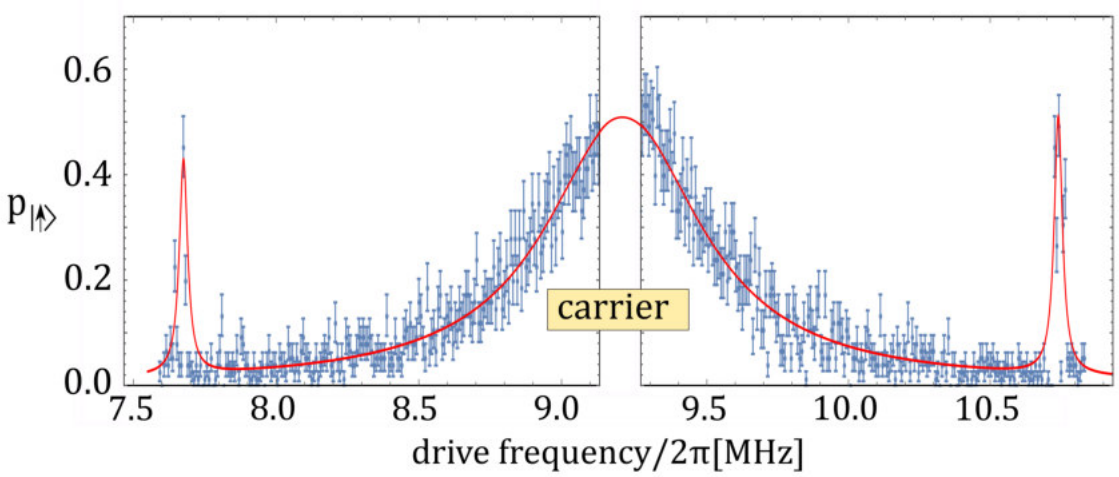

Figure 5.1: *HF spectroscopy of carrier and motional side bands on the* $|\downarrow\rangle \leftrightarrow |\uparrow\rangle$ *transition. The ion was probed 66 times with a HF pulse of length 1.75 ms with a power of 0.099 mW. The red line is a sum of Lorentzian fits to each peak.*

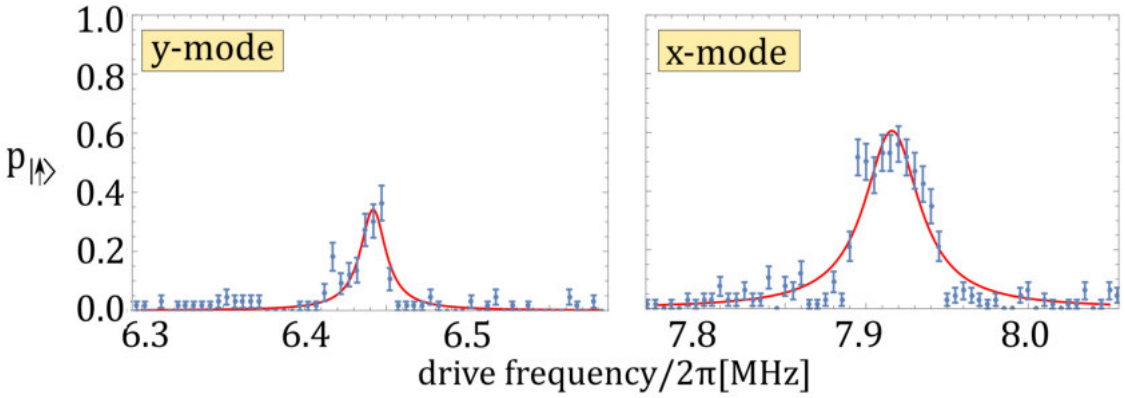

Figure 5.2: *HF spectroscopy of radial red side band transitions. We scan the frequency over the y- and x-mode, respectively, and observe the spin excitation at a distance of* $2\pi \times 1.9$ *MHz and* $2\pi \times 3.4$ *MHz from the carrier transition at* $2\pi \times 9.8$ *MHz with* $\tau = 500$ μs*,* $r = 66$ *and a power setting of 0.064 mW, cross-checked with respective side bands on the optical* $S_{1/2} \leftrightarrow D_{5/2}$ *transition. The carrier transition usually shows a FWHM below* $2\pi \times 1$ *MHz with these parameters, resulting in negligible off-resonant carrier excitation probability at the side band's frequency.*

Stability

A series of spectra of the rsb with the same parameters was taken, to characterise their stability. As can be seen in fig. 5.3, the centre frequency can vary by up to $2\pi \times 20$ kHz from measurement to measurement. This is in the same order of magnitude as the line width. Long-term drifts could not be observed.

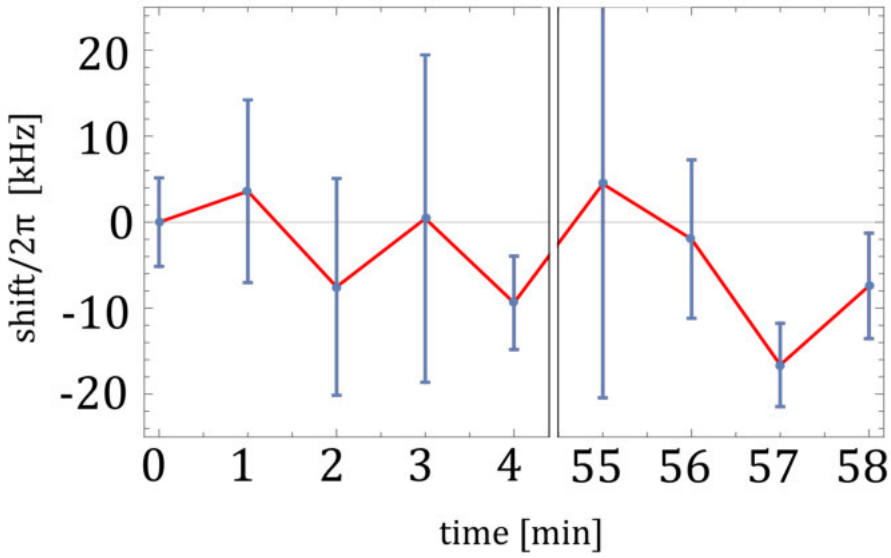

Figure 5.3: *stability of the the rsb: shown is the centre frequency from a spectrum taken with a pulse-time of 1.5 ms and 33 probings of the ion. The error-bars represent the line width of the side band.*

5.1.2 AC-Zeeman Effect

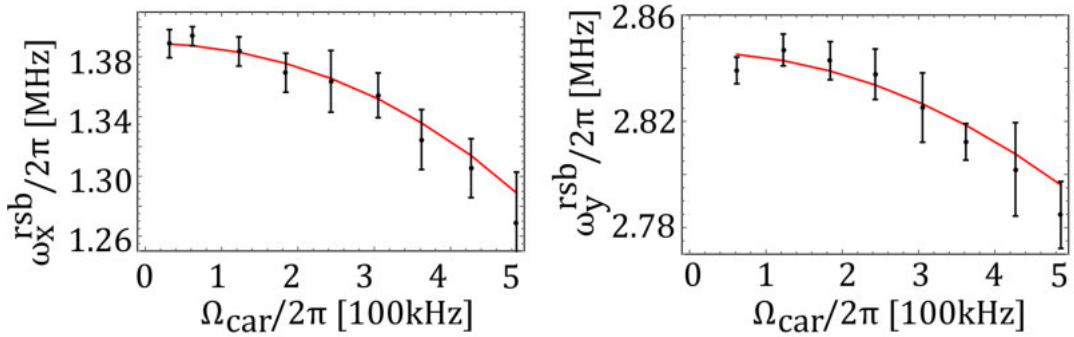

Figure 5.4: *shift of the the rsb due to excessive power in the driving field. Each point represents a spectrum taken with a HF pulse-time of 5 ms. The error-bars indicate the line width of the side band.*

As can be seen from fig. 5.1, the carrier transition is much stronger than the side bands and there are no higher order side bands, implying a low Lamb-Dicke factor. For a spectrum to feature side bands at all, this has to be compensated by long interaction times and high power settings, leading to faster Rabi oscillations. With typical settings of several $2\pi \times 100$ kHz for pulse-times up to the millisecond regime, the AC-Zeeman shift cannot be neglected. Figure 5.4 shows the distance of the side bands to the carrier in dependence of the incoming power. The order of magnitude for the shift reaches the $2\pi \times 100$ kHz regime and can be described by [Rus+17]:

$$\Delta\omega_{sb} = \Omega_{car}^2 \frac{\omega_a}{\omega_f^2 - \omega_a^2}, \tag{5.2}$$

where ω_a is the position of the carrier and ω_f the drive frequency.

5.1.3 Dynamics of the Side Band Transitions

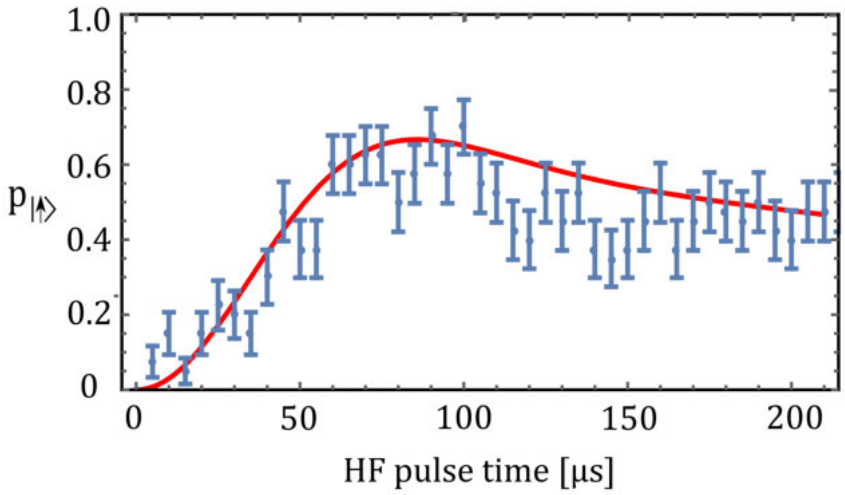

Figure 5.5: *time evolution of the rsb with a mode frequency of* $2\pi \times 1.1$ *MHz. For each point the ion was probed 40 times with a power of 0.06 mW.*

In most measurements of the time evolution of a side band, we observed an incoherent increase of the population of the $|\uparrow\rangle$ state, till it settles more or less at a probability of 0.5 on timescales between 100 µ and milliseconds. In order to observe at least the onset of coherent behaviour, we had to decrease the mode frequency to $2\pi \times 1.1$ MHz to increase the Lamb-Dicke factor, c.f. eq. (5.1). For this, the axial confinement had to be increased to more than 2×1.2 MHz, while the power setting was limited to 0.06 mW to avoid off-resonant carrier excitation. The measurement is shown in fig. 5.5, the fit to the data has a π-time of 85 µs and a mean phonon number of 20.

5.1.4 Coherence and Spin-echo

Due to the difficulties to observe coherent time evolution of the side bands, we have to look into the coherence time of our system. The strength of a J-type spin-spin coupling (eq. 2.49) goes with η^2. To harness it for a quantum simulation, we need several milliseconds of coherent dynamic. Figure 5.6 shows a long term observation of Rabi oscillations on the carrier. It reveals noteworthy deviations from a squared sinus on a timescale of 300 µs and complete loss of coherence not later than 700 µs.

To analyse this problem further, we did Ramsey experiments, as shown in fig. 5.7. The ion is brought in the equal superposition state $|\psi\rangle = \frac{1}{\sqrt{2}}(|\downarrow\rangle + |\uparrow\rangle)$ with a $\pi/2$-pulse on the HF carrier. Then the system evolves freely during a time t_{wait}, accumulating a phase

$$\chi(t_{\text{wait}}) = \int_0^{t_{\text{wait}}} \omega_a(t)\mathrm{d}t. \tag{5.3}$$

Another $\pi/2$-pulse will then map this phase to a population difference. The signal of the second $\pi/2$-pulse has thereby a phase ϕ in respect to the first pulse. Scanning over ϕ, while ω_a is constant leads to a probability of $p = 0.5 - 0.5\mathrm{Cos}[\phi + \chi]$ being in $|\downarrow\rangle$. Now if there are some stray magnetic fields present, the Zeeman splitting

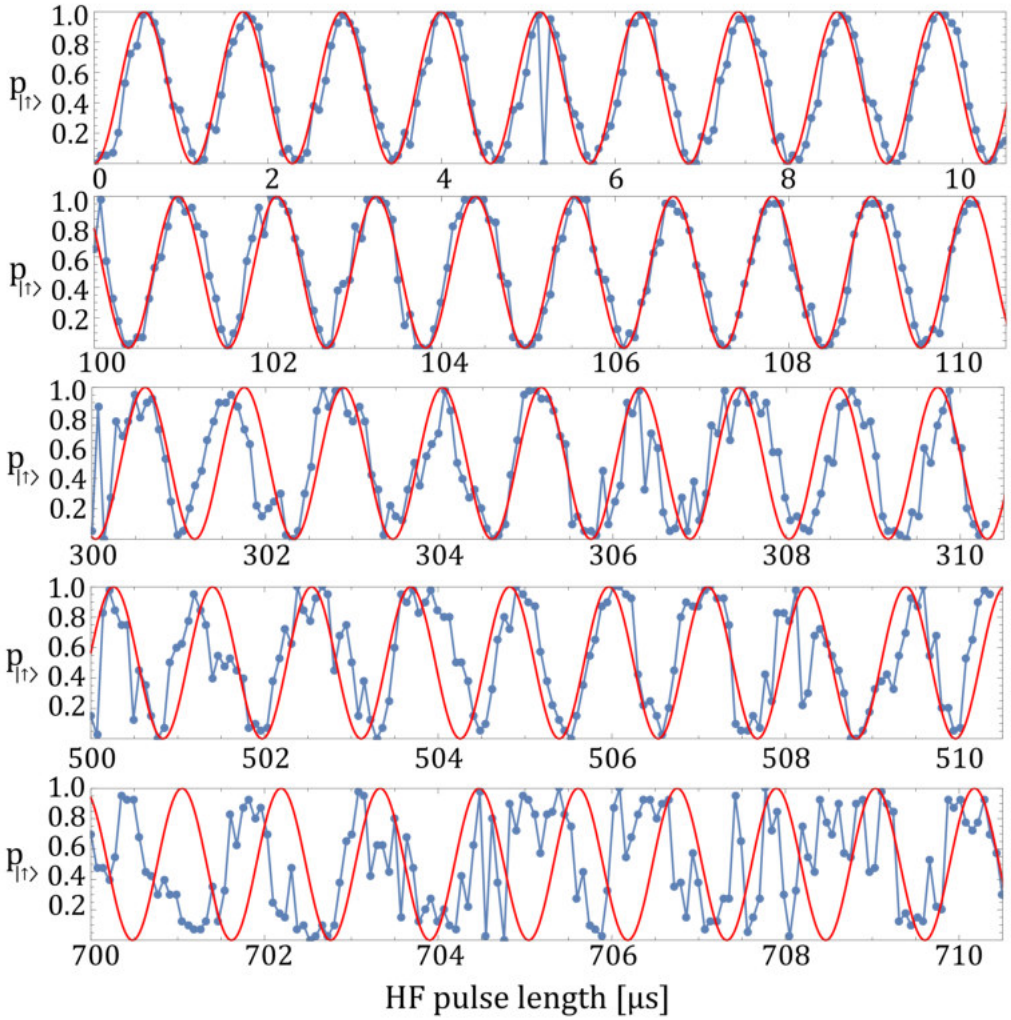

Figure 5.6: *Rabi oscillation on the HF carrier for different time intervals. The red curve is fitted to the first three data sets and has a frequency of* $\Omega = 2\pi \times 877$ *kHz.*

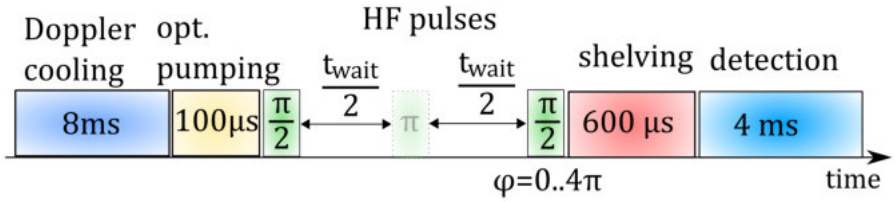

Figure 5.7: *HF Ramsey sequence.*

$\hbar\omega_a$ will be time dependent. This leads to different phases χ during each measuring cycle, thus starting to randomise p. For little changes in χ, the contrast of p, defined by

$$\text{contrast} = \frac{\max[p] - \min[p]}{\max[p] + \min[p]}, \tag{5.4}$$

is diminished, see fig. 5.8. The remaining contrast can than be plotted against the time of free evolution, yielding the bottom part of fig. 5.9. The data can be approximated by a Gaussian. The characteristic time for the contrast falling to 1/e is then called the *coherence time*. The dephasing can be counteracted by a spin-echo sequence, provided that the changes in $\omega_a(t)$ are slow, e.g. that $\omega_a(t)$ is

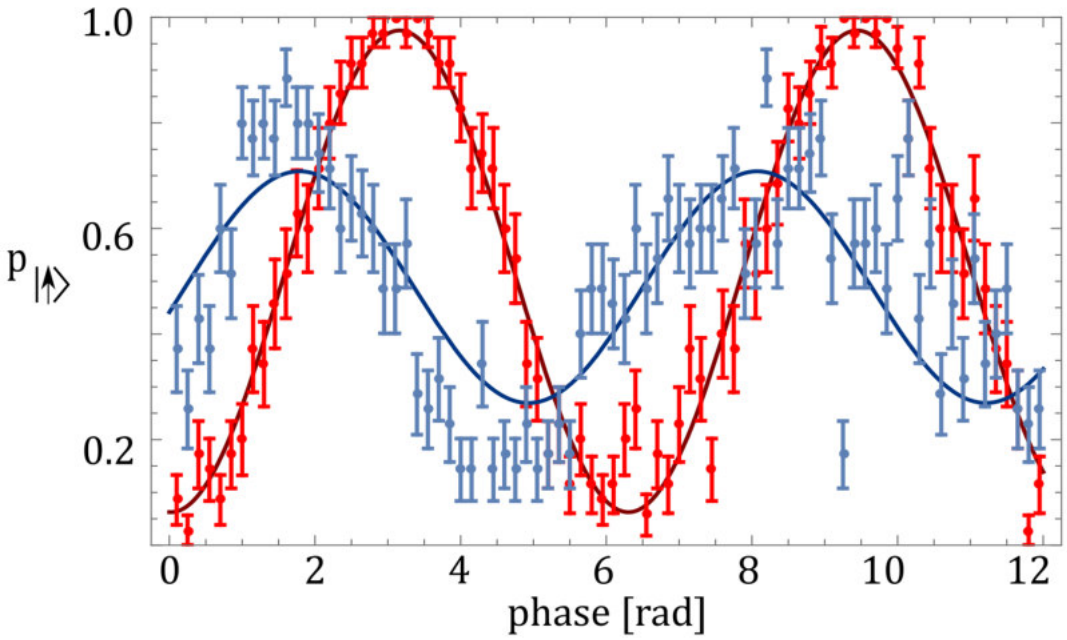

Figure 5.8: *Two example Ramsey fringes after a waiting time of 20 µs (red) and 300 µs (blue) with three π-pulses refocussing the spin.*

nearly constant during one measuring cycle. In that case, an additional π-pulse in the middle of the free evolution inverses the process. Thus, the phase accumulated during the second half neutralised the phase of the first half. For faster changes in $\omega_a(t)$, the time during the $\pi/2$-pulses can be further divided by additional π-pulses, as long as $\omega_a(t)$ is constant in the time interval before and after the pulse.

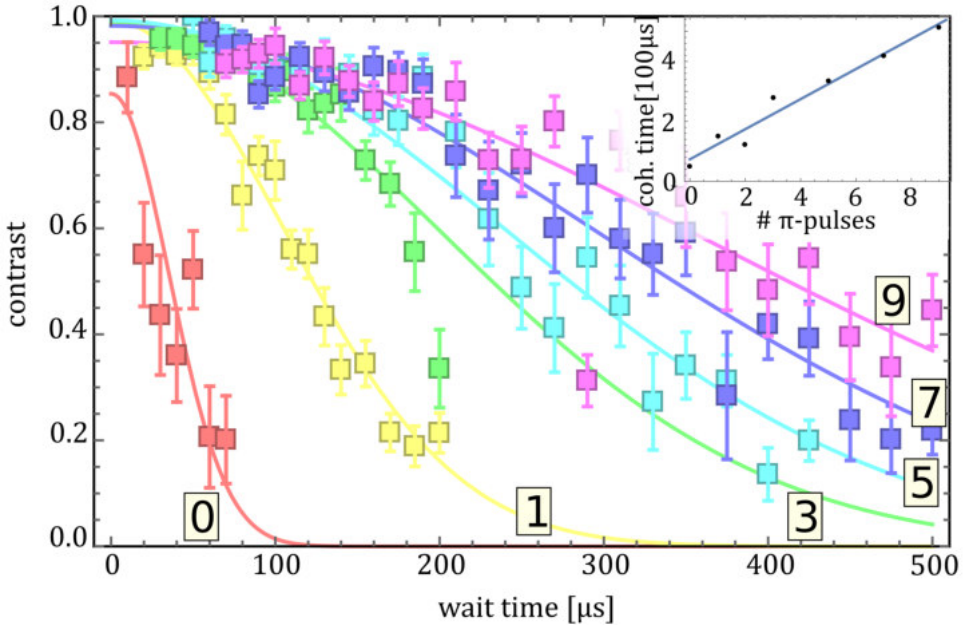

Figure 5.9: *Contrast loss of Ramsey fringes. The number at each data set, indicates the number of π-pulses used to refocus the spin. The inlet shows the time for the contrast falling to 1/e.*

The fringe contrast is fitted by a Gaussian decay with a 1/e-time of ~ 50 µs, see fig. 5.9. This is much shorter than what could be expected from the previous measurement, see fig. 5.6 and the additional decoherence source has yet to be identified. However, for an odd number l of π spin-echo refocussing pulses, we find that the measured coherence time scales with $l^{0.64(13)}$ and for $l = 9$ we reach ~ 0.5 ms. Such power law indicates a Lorentzian noise spectrum [BG+13] which in our case is fully dominated by fluctuations of currents ≤ 2 $\mathrm{mA_{rms}}$ within the wires for the magnetic field gradient. Trap control DC voltages are sufficiently stable, such that a calculated displacement of the ion crystal due to observed maximal noise from the voltage source on one or several electrodes is but a fraction of the radial wave packet size of 39(3) nm, keeping the ion crystal aligned within the gradient field.

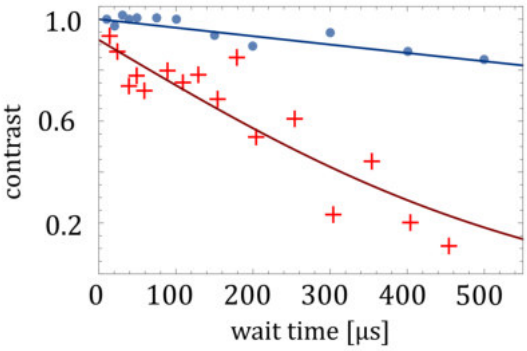

Figure 5.10: *Contrast loss of Ramsey fringes with three spin echo sequences for the external magnetic field perpendicular to the trap surface (red) and parallel to the trap axis (blue).*

An outdated firmware of the FPGA limited the number of sequences for this measurement. However, there is no fundamental limit to the number of π-pulses and the millisecond regime seems reachable. This is also, the most simplistic version. More sophisticated and robust schemes have been demonstrated [Pil+13].

If we align the external magnetic field along the trap axis, the coherence time increases by an order of magnitude, see fig. 5.10. At the same time, the magnetic field gradient and thus the effective Lamb-Dicke factor is reduced by an order of magnitude. The Rabi oscillations shown at the beginning of this chapter were observed with this setup.

5.1.5 Coherent Excitation

Another possibility to handle a low coherence time is, to go around it by speeding up the transitions, i.e. the Rabi frequency. According to eq. (2.37), we have:

$$\Omega_n^{-1} = \Omega_0 \frac{\eta \mathrm{e}^{-\eta^2/2}}{\sqrt{n}} L_n^1(\eta^2) \tag{5.5}$$

for the first red side band. Increasing Ω_0 by applying more power is possible, but would also broaden the already dominant carrier transition even further, leading to off-resonant excitations. Increasing η can be achieved by lowering the according trap frequency or heightening the magnetic field gradient. The first would bring the side bands closer to the carrier and would lead thus also to off-resonant carrier excitation. The latter is restricted by technical problems, discussed in ch. 6.2. Therefore, only the phonon dependency remains. The spin-spin interaction described by the Hamiltonian in eq. (2.60) does not depend on the phonon number in the modes, as long as the gradient is constant over a region of the corresponding wave paket size of the mode. Thus, a mode-specific spin manipulation can be sped up by a higher phonon number, without a detrimental effect onto the spin-spin interaction.

In fig. 5.11 is a phonon dependendy depicted for a $\eta = 0.07$ as an exemplary value for the $S_{1/2} \leftrightarrow D_{5/2}$ transition. For smaller η, the curves are getting stretched along the n-axis. We see that the red side band Rabi frequency increases for a while with increasing phonon number. As stated before, this behaviour can be approximated by $\Omega_0 \eta \sqrt{n}$.

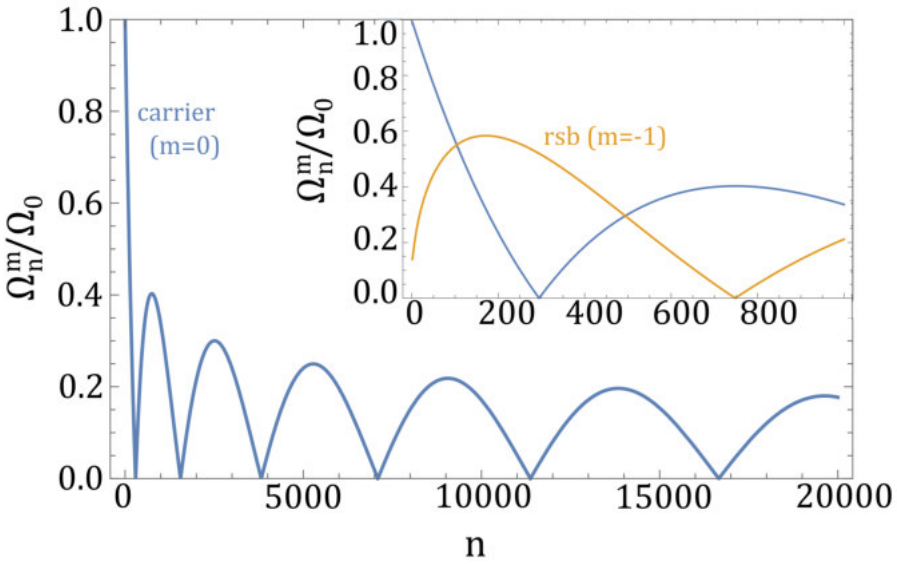

Figure 5.11: *Phonon dependency of the Rabi frequency (2.37) for an* $\eta = 0.07$*. The inlet shows a magnification for a lower number of phonons.*

To increase the phonon number, we apply an additional alternating voltage to the near wire. The electrical field couples to the charge of the ions and can excite the motional state if it has the according frequency. Thus, we end up with a coherent motional state. However, since the trap frequencies are in the low MHz regime, the corresponding wavelengths are huge compared to the distances between the ions. Therefore, only modes with a parallel movement of the ions can be excited and modes with counter propagating ions cannot be excited this way. Also, the axial modes cannot be excited, since the wire is parallel to the trap axis.

Figure 5.12 shows an excitation spectrum of a single ion. Both radial modes are clearly visible. At a peak in this spectrum, the ion is gathering so many phonons, that the Rabi frequency of the carrier of the $S_{1/2} \leftrightarrow D_{5/2}$ transition

$$\Omega_n^0 = \Omega_0 e^{-\eta^2/2} L_n^0(\eta^2) \tag{5.6}$$

has been considerably lowered, see fig. 5.11, and shelving is starting to lose its effectiveness and some population remains in $|\downarrow\rangle$.

Once we know the frequencies, at which the most phonons are generated, we choose one of them and scan over the power output of the signal generator creating the excitation pulse. Figure 5.13 shows such measurements. For a weak excitation field, the motional state of the ion is only negligibly altered, shelving works and the ion is dark during detection. For increasing power outputs, we get several peaks before the ion stays more or less permanently bright at the highest power level. To understand this behaviour, we once again have to take a look at fig. 2.37. Each time the carrier vanishes, shelving breaks down. When it recovers, so does the shelving process. This goes on, until even a local maximum of the Rabi frequency is no longer

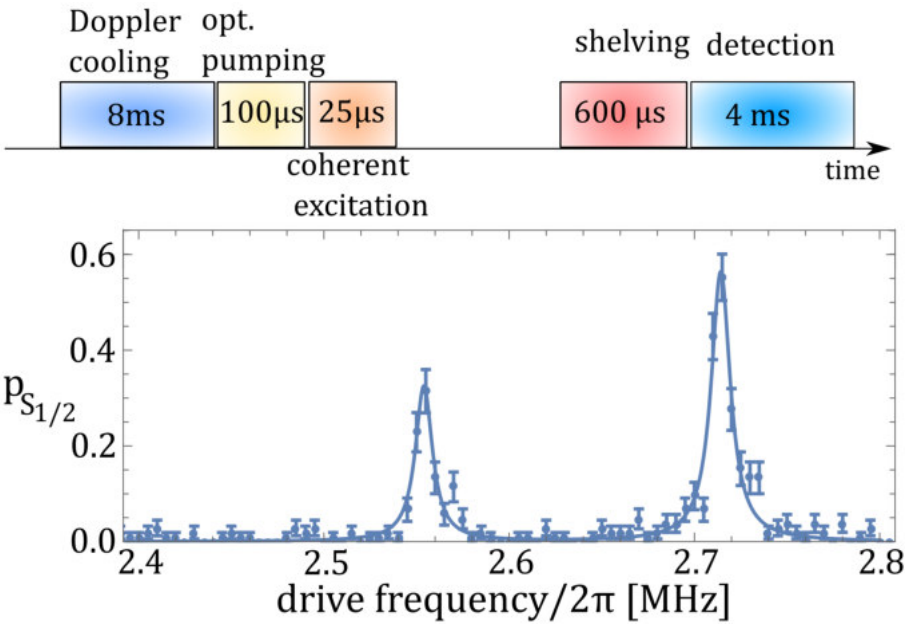

Figure 5.12: ***top:*** *sequence for characterising coherent excitation of trap modes.* ***bottom:*** *excitation spectrum of the radial modes of a single ion at a power of* 0.5 µ*W for* 500 µ*s. Each point represents 105 measurement cycles.*

fast enough. Since the state discrimination is based on the shelving of $|\downarrow\rangle$ to the $D_{5/2}$ level, we can only work in those regions that show a sufficiently high shelving effectiveness.

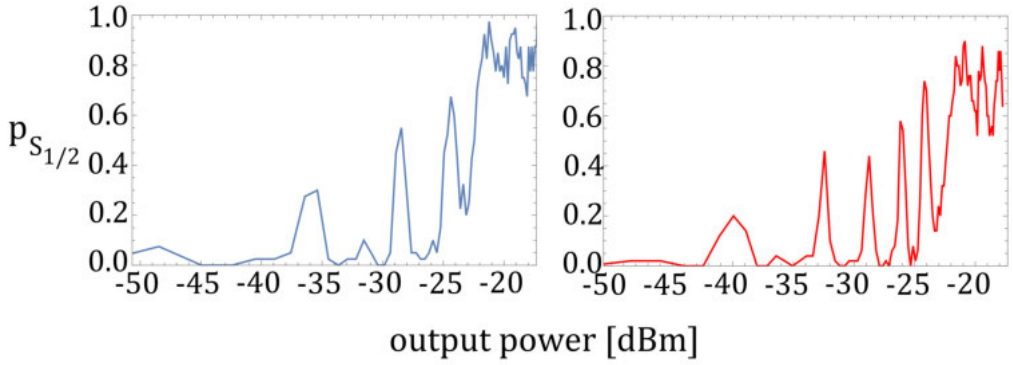

Figure 5.13: *scan over the excitation power* ***left:*** *for the weak radial mode at* $2\pi \times$ 2.65 *MHz with an excitaion time of* $t = 10$ µ*s* ***right:*** *for the strong radial mode at* $2\pi \times 3.01$ *MHz for* $t = 25$ µ*s.*

To infer the mean phonon number $\bar{n}$ after an excitation [Alo+16], pulse length scans on carrier and side bands of the $S_{1/2} \leftrightarrow D_{5/2}$ transition can be made and fitted with

$$p_{D_{5/2}} = \sum_n p_n^{\mathrm{coh}}(\bar{n}) \cdot \sin^2\left[\frac{\Omega_n^m}{2} t\right]. \tag{5.7}$$

But, in an excited state, the sum consists of hundreds to thousands of constituents, making this procedure computationally intensive and fault-prone. Thus, we followed a more pragmatic approach. For sufficiently high $\bar{n}$, the coherent state distribution (2.22) is approximately symmetric around $\bar{n}$. Since the standard deviation is a

function of $\bar{n}^{1/2}$, it is relatively strong localised around $\bar{n}$. Furthermore, eq. (5.6) is approximately symmetric in a small area around its extrema. We can thus assume that eq. (5.7) as a function of $\bar{n}$, for a fixed pulse-time t, has the extrema at the same positions as a Fock state with $\bar{n}$ phonons. Therefore, we can simply compare minima and maxima of a power scan with eq. (5.6) to get a relationship between the mean phonon number and the input power.

For this to work, η has to be known, which can be inferred from fits to a low phonon number state. However, in these fits $\bar{n}$ and η are free parameters, and the solution is not unique. This can be solved by cooling the ion to the motional ground state, thus eliminating $\bar{n}$. In this work, a sub Doppler cooling was not implemented, leaving us with a uncertainty in η, that origins in the uncertainty in the angle between the mode vector and the laser. It can by principle be inferred from and set by the applied voltages. However, electrical stray fields can tamper with the results. The above described procedure has been executed for the following three setups:

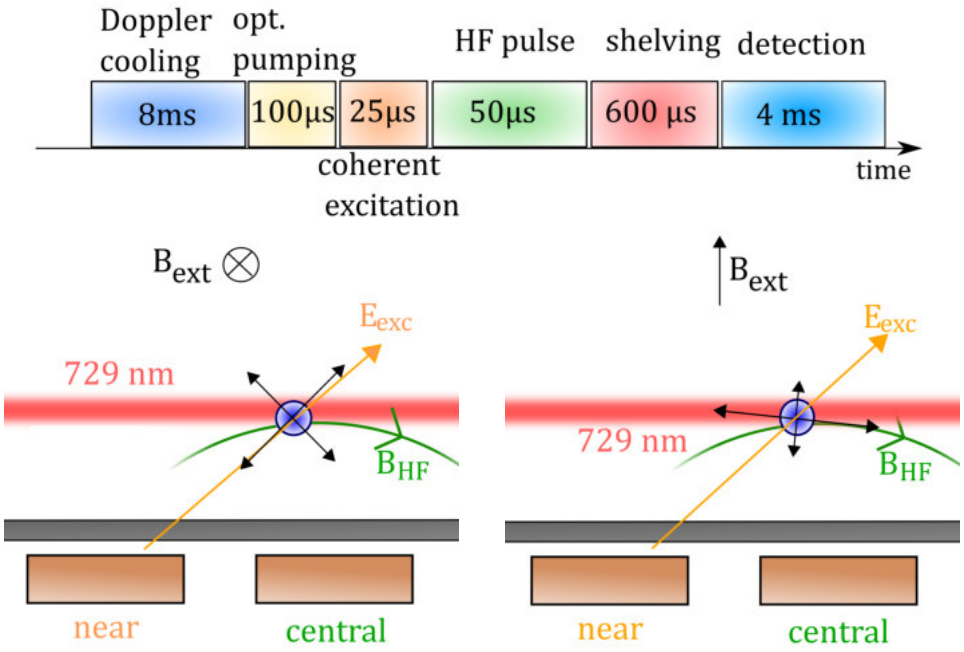

Figure 5.14: ***top:*** *sequence for HF dynamics with coherent excitation.* ***bottom:*** *schematics of the used setup during coherent excitation.*

- external magnetic field parallel to trap axis, excitation of the weak radial mode (x) at $2\pi \times 2.73$ MHz, fig. 5.14 left
- external magnetic field parallel to trap axis, excitation of the strong radial mode (y) at $2\pi \times 3.01$ MHz, fig. 5.14 left
- external magnetic field perpendicular to surface, excitation of weak radial mode (x) at $2\pi \times 2.02$ MHz, fig. 5.14 right

For the magnetic field parallel to the trap axis, weak and strong radial trap confinements have been set such, that they differ not more than $2\pi \times 150$ kHz and that they have an angle of approximately $\pi/4 \pm \pi/8$ to the 729 nm laser beam. The comparison between a power scan and eq. (5.6) yields in the first case

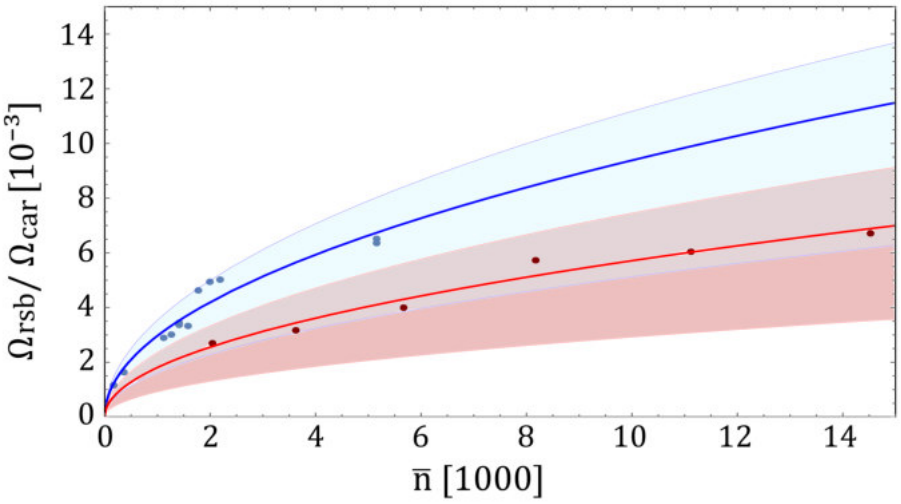

Figure 5.15: *effective Lamb-Dicke factor for a magnetic field parallel to the trap axis after excitation of the weak radial mode at* $2\pi \times 2.73$ *MHz (blue) and after excitation of the strong radial mode at* $2\pi \times 3.01$ *MHz (red). The coloured area indicates the uncertainty in phonon number, see text for details.*

$\bar{n} = (1.42\,^{+3.38}_{-0.31}) \times 10^5 P/\mathrm{mW}$ and in the second case $\bar{n} = (5.7\,^{+16.2}_{-2.4}) \times 10^6 P/\mathrm{mW}$. The difference in magnitude reflects the angle towards the excitation field, see fig. 5.14. In the third case, the strong confinement was set to $2\pi \times 2.8$ MHz, leading to an angle of about $\pi/16 \pm \pi/8$. A symmetric orientation of the modes towards the gradient was chosen to allow the investigation of both modes. Resulting in a phonon accumulation of $\bar{n} = (2.7\,^{+3.9}_{-1.5}) \times 10^6 P/\mathrm{mW}$.

We can now include a HF pulse into the sequence to drive the $|\downarrow\rangle \leftrightarrow |\uparrow\rangle$ transition, as shown in the upper part of fig. 5.14. We observe the time evolution of the carrier and the red side band. The ratio between the Rabi oscillations for both transitions is for a sufficiently small n:

$$\frac{\Omega_{\mathrm{rsb}}}{\Omega_{\mathrm{car}}} = \eta \bar{n}^{1/2} \tag{5.8}$$

Since we already know $\bar{n}$ from the power setting, we get a value for the effective Lamb-Dicke factor created by the magnetic field gradient. The results for the first two cases are shown in fig 5.15 and for the last case in 5.16, with some examples for the time evolution of the rsb at different mean phonon numbers. The extracted Lamb-Dicke factors read:

$$\eta_1 = (9.4\,^{+1.7}_{-4.3}) \times 10^{-5} \tag{5.9}$$
$$\eta_2 = (5.7\,^{+1.8}_{-2.8}) \times 10^{-5} \tag{5.10}$$
$$\eta_3 = (1.126 \pm 7) \times 10^{-3} \tag{5.11}$$

In the first two cases, the external magnetic field is perpendicular to the quadrupole field and thus the vectorial sum yields only a relatively small difference in the magnetic field. The magnetic field gradient is in the order of 0.5...1.5 T/m. In the third case, the external field and a part of the quadrupole adds up linearly, leading to greater differences in the magnetic field.

Without coherent excitation, we could expect π-times in the millisecond regime for η_1 and η_2 with typical parameters for $\Omega_0 = \pi/550$ ns and a thermal state of

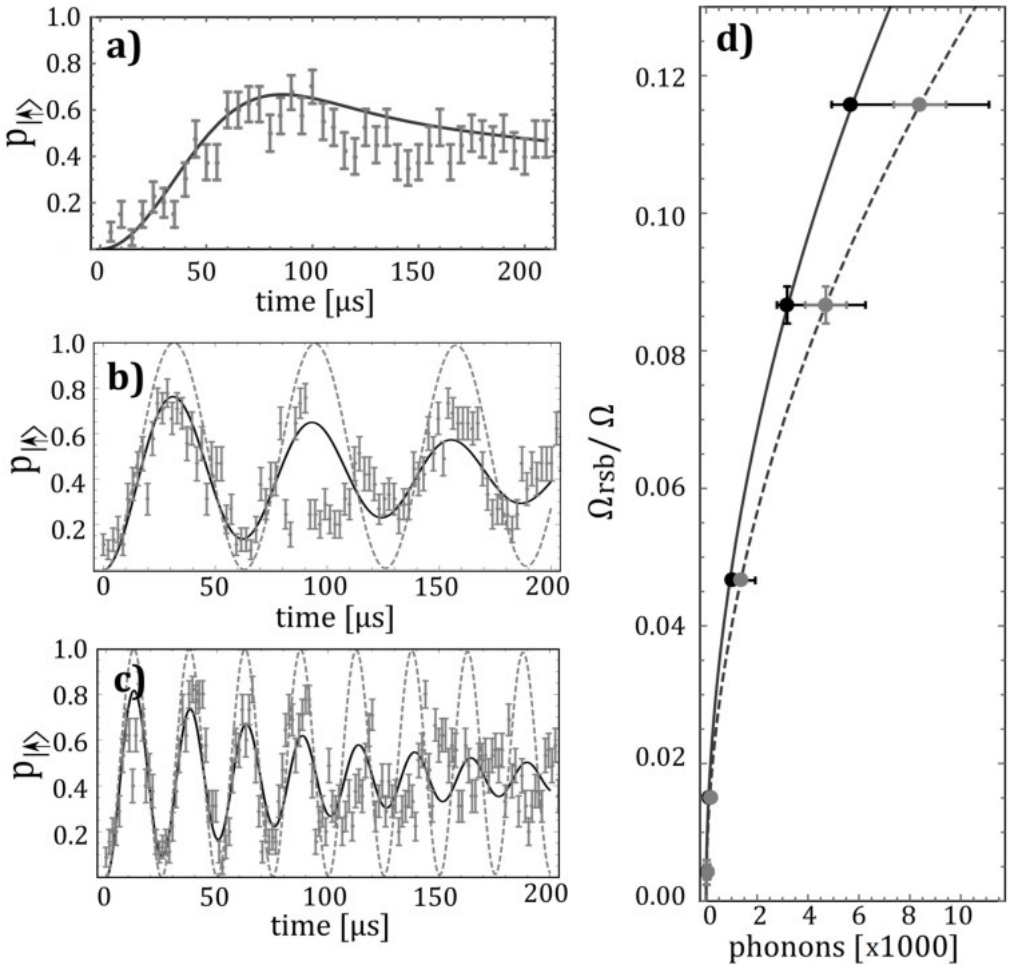

Figure 5.16: *Rabi oscillation on the red side band, at $2\pi\times 1.05$ MHz, for a single ion in* ***a)*** *a thermal state with a fit assuming a mean phonon number of* 20.9(2.5). ***b)*** *Rabi oscillation for a coherent state of $\bar{n}_{coh} = 1360(180)$ phonons and* ***c)*** *8400(1000). Due to the relatively small variation of the Rabi frequency over a coherent phonon distribution a sinusoidal fit (dashed lines) yields a viable approximation. An exponential decay with $\tilde{\tau}$ = 130(30) µs is taken into account for the fit (solid line).* ***d)*** *Determination of the effective Lamb-Dicke factor on the red side band enhancement from coherent excitation: Rabi frequency data $\Omega_{rsb}/\Omega = \eta\sqrt{n}$ for the the spin transition are fitted with a calculated η (grey, dotted) or scaled with mean phonon numbers, extracted from Rabi frequency data of the optical transition (black, solid). The error in the determination of $\bar{n}_{coh}$ is due to an uncertainty of laser direction and magnetic field gradient direction, with respect to the eigenvector of the radial mode. In (b,c,d) a radial frequency of $\omega_{rad}/2\pi = 2.02$ MHz was used.*

$\bar{n} = 20$, whereas η_3 already achieves a $t_\pi \approx 100$ µs, see fig. 5.16, a). Therefore, we are approximately a factor 2 too slow to see coherent dynamics on a side band with a Doppler cooled ion, see previous section. The possibilities to push down the π-time further and their downsides have already been discussed at the beginning of this section.

With a coherent excitation, in the third setup we achieved coherent states with up to $\bar{n}_{\mathrm{coh}}$= 8400(1000) in the weak radial mode and 1360(180) in the strong radial mode. With the calculated Lamb-Dicke factor we infer the grey dotted line in

fig. 5.16(d). To cross-check the results of $\bar{n}_{\mathrm{coh}}$, we also drive Rabi oscillations on the optical $S_{1/2} \leftrightarrow D_{5/2}$ transition with known Lamb-Dicke factor. Thus, we can infer the mean phonon number in dependence of the power level of the electric excitation [Alo+16]. We obtain $\bar{n}_{\mathrm{coh}} = 5600(^{+5500}_{-700})$ and $990(^{+940}_{-120})$, respectively, for the above mentioned cases. A fit to the Rabi oscillation of the rsb of the Zeeman transition with these mean phonon numbers yields $\eta = 0.0015(^{+1}_{-7})$, which agrees within errors with the calculated value from eq. (2.59). With the fitted Lamb-Dicke factor we infer the solid, black line in fig. 5.16(d).

The fastest spin flip on a side band could be achieved in about 12 µs with the coherent state of $\bar{n} = 8400(1000)$. The spectrum is shown in fig. 5.17. The side bands have a full width half maximum of 130 kHz. The according time evolution of the rsb is shown in the in fig. 5.16, c).

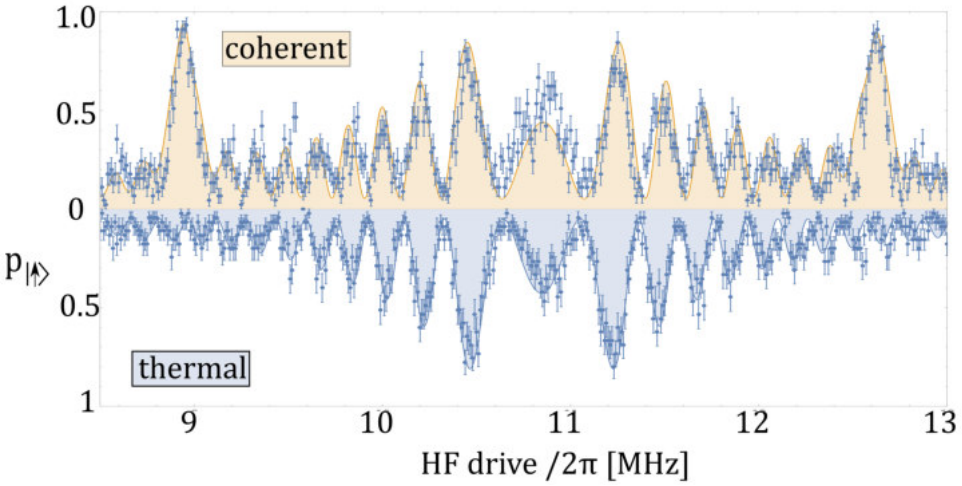

Figure 5.17: *HF spectrum of a thermal state with* $\bar{n} = 20.9(2.5)$ *and a coherent state with* $\bar{n} = 8400(1000)$*, each taken with a HF pulse-time of 7* µs.

5.2 Ion Crystals

This section is dedicated to crystals consisting of several ions. In particular, spectra of 2-, 3- and 4-ion crystals in a linear or planar configuration are presented.

5.2.1 2-Ion Crystals

With an increasing number of ions, additional motional modes arise. In fig. 5.18 the spectrum of a single ion is compared with the spectrum of a 2-ion crystal with the same trapping parameters. The peak that occurs in both plots around $2\pi \times$ 9.935 MHz is usually referred to as *common mode*, in short *com-mode*. It has the eigenvector $(1, 1)/\sqrt{2}$ and the frequency is identical to the according trap frequency of $2\pi \times 2.70$ MHz. The additional mode, only occurring for two ions, has the eigenvector (1,-1)/$\sqrt{2}$ and a smaller frequency by roughly $2\pi \times 80$ kHz.

The fact that the second mode can be seen in the spectrum is counter-intuitive at first. With an axial frequency of about $2\pi \times 630$ kHz, the distance between the ions is 7.6 µm, which is much smaller than the foci of the relevant lasers. Therefore, the ions are equally well initialised and read out, as can be seen at the base line

of the spectrum. The wavelength of the driving field has an order of magnitude of meters. It should not produce a force moving the ions in the opposite directions to each other.

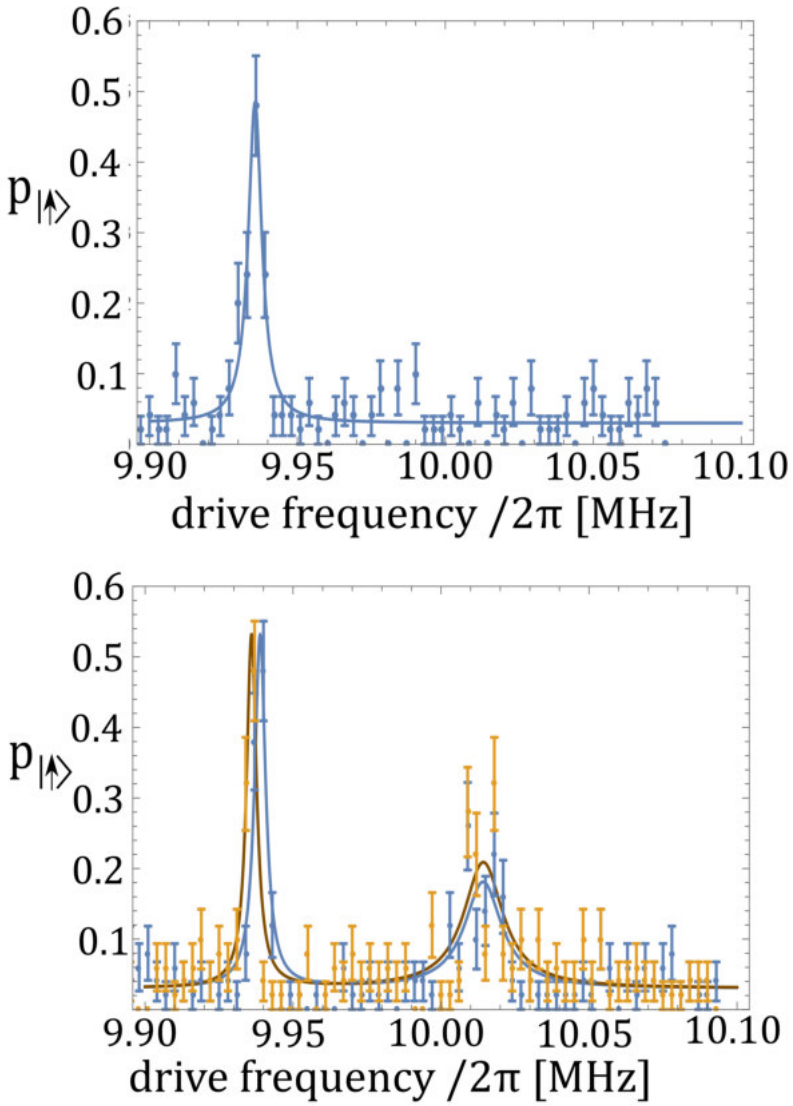

Figure 5.18: *spectrum of the red side band (strong radial mode). The ion was probed 50 times with a pulse-time of 7 ms with an output power of 0.99 μW.* ***top:*** *spectrum of a single ion.* ***bottom:*** *spectrum of each ion of a 2-ion crystal.*

In a simple model, the actual static force on the ion is caused by the magnetic field gradient and the spin alignment. The driving field induces off-resonant Rabi oscillations with partial spin flips. On each spin flip, the force on the ion due to the gradient also changes its direction. Thus, the trapped ion can be seen as a driven oscillator with an external force of frequency $\omega = \sqrt{\Omega_0^2 + \delta^2}$. Since Ω_0 is much smaller than the trap frequency ω_t, the resonant case at $\omega = \omega_t$ is given at a detuning of $\delta \approx \omega_t$. If both ions are initialised in the same state, the oscillating force points in the same direction, coupling the spin to the com-mode. On the other hand, if the spins are aligned anti-parallel, the gradient pushes the ions in opposite directions upon a spin flip and coupling the spin to the second mode.

As can be seen in fig. 5.19, the initialisation does not have a noteworthy effect

upon the occurrence of a peak in the spectrum. The sequences for this measurement is shown in the top part of fig. 5.19. First the ions are initialised in $|\downarrow\downarrow\rangle$. Then they are brought in the equal superposition state with a HF $\frac{\pi}{4}$ pulse. Any population in the $|\uparrow\rangle$ state is shelved with a $\frac{\pi}{2}$ pulse, before the first detection. The detection will break down the superposition randomly to any of the four possible spin alignments. Thereupon, the population that was in the $|\downarrow\rangle$ state is re-initialised and the population of the $D_{5/2}$ level is mapped back to the $|\uparrow\rangle$ level by another $\frac{\pi}{2}$ pulse. What's left, is the usual sequence for a HF spectrum. Afterwards, each measurement can be sorted by the result of the first detection.

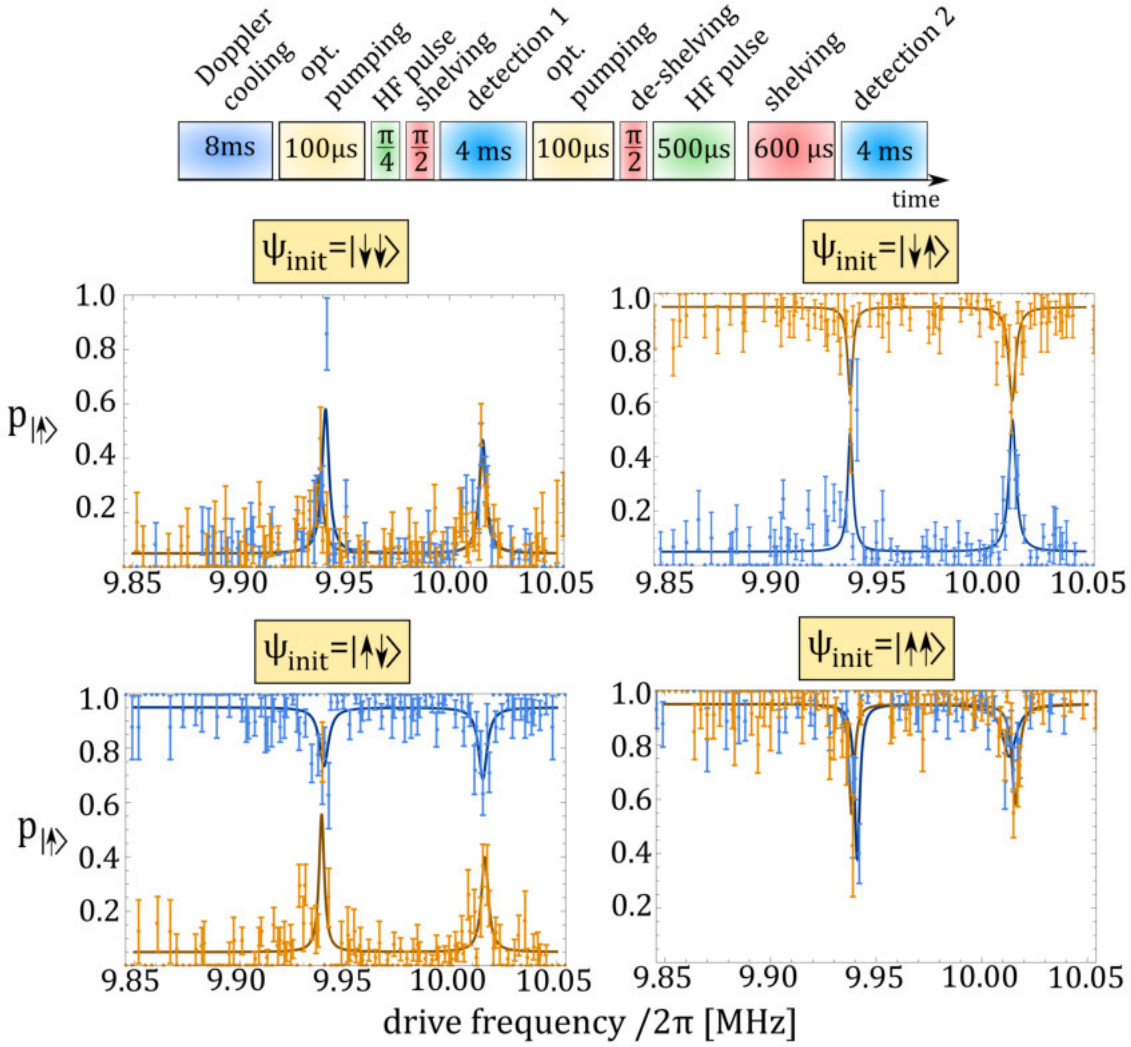

Figure 5.19: ***top**: sequence to test different spin-initialisation.**bottom**: spectra of a 2-ion crystal with different initial states ϕ_{init}. Blue denotes the state of the first ion and orange the state of the second ion. The spectrum pulse was 7 ms long with an output power of 0.99 µW. For each case the ion was probed 23(12) times on average per data point. The com-mode and the rocking mode are both appearing independent of spin-initialisation.*

Since the initialisation showed no measurable effect, we compared Ramsey fringes of two ions in a crystal with varying distance and got for the magnetic field gradient along the trap axis an upper limit of 0.02 T/m, see sec. 4.2.5. The associated difference in the resonant frequency has been observed to be in the order of $2\pi \times$ 10 kHz. This difference also leads to a $2\pi \times 10$ kHz faster off-resonant Rabi oscillation for one ion. Thus, the oscillating forces on both ions gather a phase difference of π after 50 µs. The π-time for the red side band with a Lamb-Dicke factor of $\eta = 1.1 \times 10^{-3}$ for a Doppler cooled ion is roughly 100 µs and a typical spectrum pulse is a multiple of that time. Thus, the force inducing the motional side bands pushes the ions in the same and in opposite directions for the same amount of time, leading to spectra featuring both modes. Another issue is the coherence time, which is on the same time scale as the dynamics of the side bands.

5.2.2 Linear Crystals

We investigate spin transitions in the vicinity of a structural transition of a small ion crystal of three ions by adjusting the anisotropy parameter $\alpha = (\omega_z/\omega_{rad})^2$, which is controlled via the DC voltages. For a small anisotropy, the ions align in a linear configuration along the trap axis. For α above the critical value α_{crit} ions are forming a zigzag-crystal [BKH92; Fis+08; Kau+12]. We took spectra using a sequence as shown earlier in fig. 5.12, wherein we monitored the fluorescence of one of the outer ions of the 3-ion crystal. Figure 5.20 shows spectra of that outer ion for four different sets of trap frequencies with increasing anisotropy. For three ions, the approximation $\alpha_{crit} = 2.94N^{-1.80}$ yields $\alpha_{crit} = 0.407$. The green spectrum was taken with the anisotropy being far away from the critical point and the ions aligned linearly along the trap axis. All three modes with the eigenvectors x-com = $(1,1,1)/\sqrt{3}$, x1 =$(1,0,-1)/\sqrt{2}$ and x2=$(1,-2,1)/\sqrt{6}$ in the direction of the weak radial confinement are visible. Increasing the value of α towards α_{crit} eigenfrequencies become smaller such that the observed resonances approach the carrier and get more pronounced as their effective Lamb-Dicke factors η are increasing. In the case of an anisotropy of 0.4, the mode driving the transition to the zigzag is as small as $2\pi \times 350$ kHz. The critical point was found at $\alpha_{crit} = 0.416(1)$. The spectrum for $\alpha = 0.42$ is already taken beyond the critical point with a zigzag crystal extending in the radial direction by about 1.2 µm and the modes x1 and x2 are mixed with respective modes of the z direction with a ratio of roughly 95:5. The lowest side band mode near a drive frequency of $2\pi \times 9$ MHz corresponds to a zigzag vibration of the crystal, with an eigenfrequency of $2\pi \times 215(14)$ kHz, consistent with the calculated value of $2\pi \times 225$ kHz.

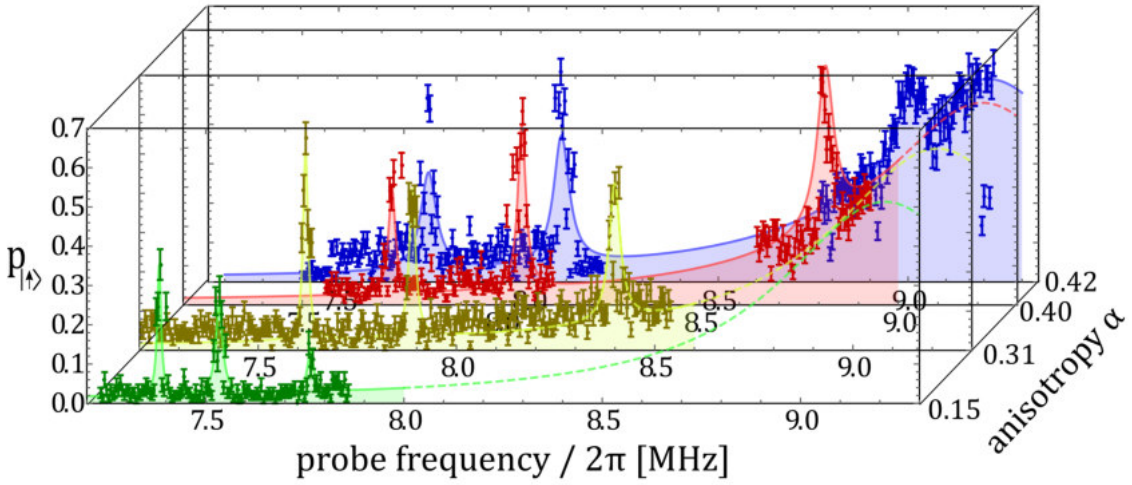

α		0.15			0.31	
mode	x-com	x1	x2	x-com	x1	x2
$\eta \times 10^3$	0.12	0.16	0.12	0.15	0.24	0.29
$\nu/2\pi$[MHz]	1.84	1.69	1.47	1.59	1.32	0.80
α		0.40			0.42	
mode	x-com	x1	x2	x-com	x1	x2
$\eta \times 10^3$	1.60	2.87	8.4	1.59	2.98	18.3
$\nu/2\pi$[MHz]	1.49	1.15	0.39	1.49	1.11	0.23

Figure 5.20: *spectra of a 3-ion crystal taken with the ROI on the outer ion, with four different sets of trap frequencies with* $\alpha = \{0.15, 0.31, 0.40, 0.42\}$. *For* $\alpha = 0.4$ *the zigzag mode shifts to* $2\pi \times 350$ *kHz (red points). At* $\alpha = 0.42$ *the critical point is already passed (blue points). The number of repetitions was* $r = 150$, $\tau = 1.75$ *ms, and the carrier transition was at* $2\pi \times 9.2$ *MHz. The table shows the absolute value of the calculated Lamb-Dicke factor according to eq. (5.1) for the observed ion with an angle of* $10°$ *between the magnetic field gradient and the direction of the weaker mode, inferred from numerical simulations, and the according mode frequency calculated from a pseudo potential approximation.*

Individual Addressing

In fig. 5.21 the com-mode side band of all ions of a 3-ion crystal is shown. The centre frequency is shifted for all ions by roughly $2\pi \times 25$ kHz. The spectra were taken simultaneously and the splitting is not the result of a erratically moving side band. The shift is one order of magnitude bigger than expected from eq. (2.55). Therefore, it is consistent with a small angle of the crystal towards the magnetic field as found before, see sec. 4.2.5. The splitting has the same order of magnitude as the line width. Therefore, an individual addressing of the ions via the side bands is principally possible. In the current state of the experiment it can at least be harnessed to bring a single ion into the equal superposition state.

The com-mode can be coherently excited to allow a full population inversion. The broader line width can than be counteracted by one of two schemes: first a proper set of voltages is found to tilt the whole crystal further into the gradient [Kau+17]. Changing to a lower axial frequency might be useful to achieve a shear force on both

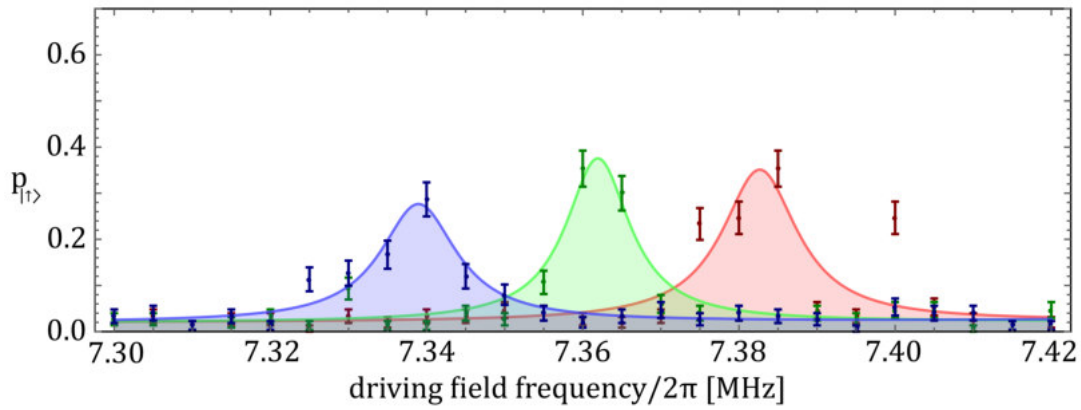

Figure 5.21: *Spectrum of each of the three ions of the same crystal with the same parameters as in fig. 5.20. A small tilt of the crystal axis towards the magnetic field, allows the individual addressing of ions.*

ends of the crystal. Thereby, each ion shows a different resonance frequency for the motional modes. However, such a procedure might be limited by the length of the chain. In the second more laborious approach, the crystal is split and the ion to be addressed is isolated over a single DC segment. There it can be shifted in the radial direction at will, to achieve a higher frequency separation to the other ions. The HF pulse is applied and afterwards the ions are brought back together. The development of such splitting and transportation schemes has seen great progress in recent years [Rus+14].

5.2.3 Planar Crystals

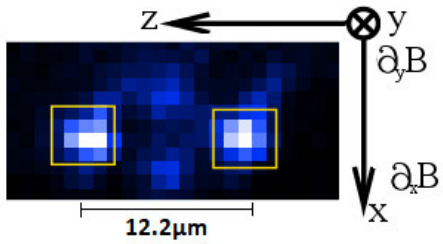

Figure 5.22: *camera picture of a 4-ion crystal in a planar configuration. The yellow boxes mark the ions that were observed during an experimental sequence.*

Our next focus in on a 4-ion crystal in a planar configuration, as seen in fig. 5.22. The plane of the crystal is tilted with regards to the trap axis, wherein the brighter, outer ions along the trap axis are on the trap axis and the darker, middle ions are off the trap axis. A state of the ions off the axis cannot be discriminated sufficiently. They are not properly initialised by the optical pumping, since the $S_{1/2} \leftrightarrow D_{5/2}$ transition frequency is shifted for those ions compared to those still on the trap axis due to the magnetic field gradient. To investigate the 4×3 eigenmodes of common vibration of the 4-ion crystal, we took spectra using a sequence as shown earlier in fig. 5.12, wherein we monitored the fluorescence of one or both of the outer ions of the 4-ion crystal. Figure 5.23 shows such a spectrum.

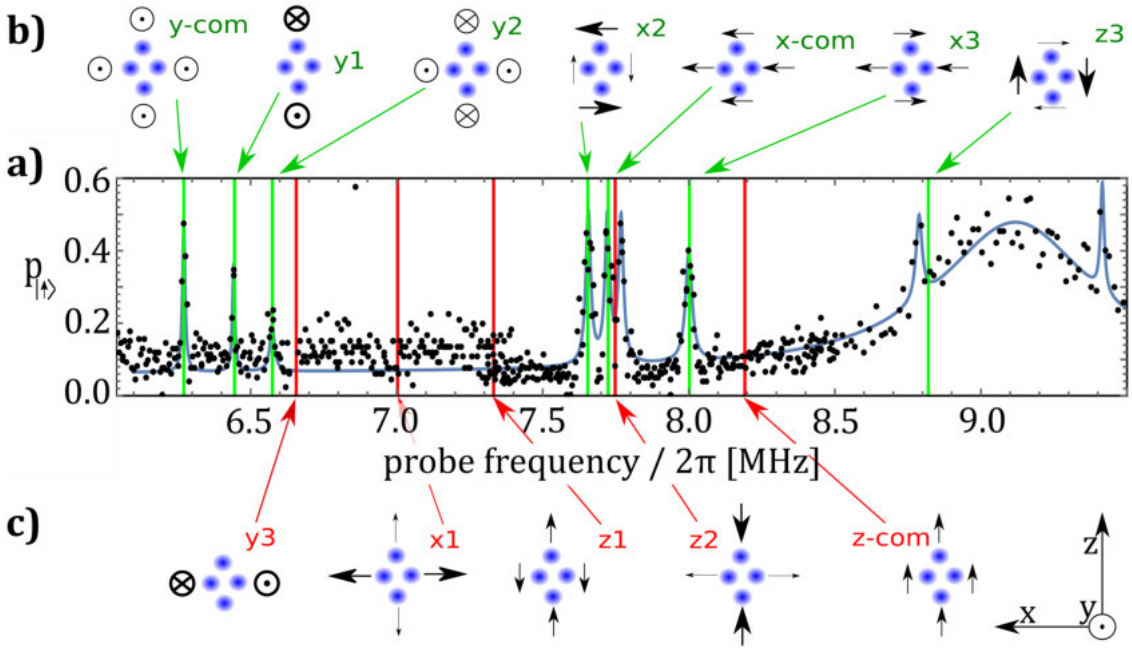

mode	y-com	y1	y2	y3	x1	z1
$\eta \times 10^3$	0.11	0.17	0.13	0.0	< 0.001	0.001
$\nu/2\pi$[MHz]	2.87	2.69	2.56	2.48	2.14	1.81

mode	x2	x-com	z2	x3	z-com	z3
$\eta \times 10^3$	1.56	1.47	0.002	2.01	0.003	6.67
$\nu/2\pi$[MHz]	1.5	1.43	1.41	1.16	0.98	0.46

Figure 5.23: ***a):*** *spectrum of a 4-ion planar crystal with $r = 66$, $\tau = 5$ ms, and a Rabi frequency of $2\pi \times 450$ kHz. Error-bars are omitted for clarity. The blue line is a sum of Lorentzian fits to each individual peak. Vertical lines indicate the calculated position of the eigenmodes from a pseudo potential approximation with an AC-Zeeman correction. Visualization of eigenmodes* ***b), c):*** *The relative strength of the motion is represented by the arrow size, (x, y, z) denote the predominant direction of motion, (1,2,3) indicate the highest to lowest mode frequency. b) eigenmodes observed in the spectrum. c) Eigenmodes with an oscillation direction of the observed ion perpendicular to the direction of the magnetic field gradient. The table shows the absolute value of the calculated Lamb-Dicke factor according to eq. (2.59) for the observed ion with an angle of 10° between the magnetic field gradient and the direction of the weaker mode, inferred from numerical simulations, and the according mode frequency calculated from a pseudo potential approximation. For a gradient along the trap z-axis the above mentioned value of 0.02 T/m was used.*

The magnetic field gradient couples only vibrational modes to the HF transition, which feature ion oscillations in the radial direction, i.e. parallel to the gradient, c.f. fig. 5.23 b). The radial x-modes, which are aligned with the gradient, show up as resonances x-com, x2 and x3 (resonance frequency indicated in green). Whereas, the eigenvector of the x1 mode, c.f. fig. 5.23 c), does not point along the magnetic field gradient with respect to the observed ions and is therefore not excited (resonance frequency indicated in red). As the HF excitation was at high power, saturating the transition with $\Omega_{\text{Rabi}} \sim 2\pi \times 450$ kHz, we also observe the radial modes with a weaker projection and stronger confinement: y-com, y1, and y2 (green). In contrast, mode y3, in which the observed ions do not move, does not show in the spectrum (red). The pure axial z-modes, namely z-com and z1, do not appear (red). In contrast, the mixed modes z2 (red) and z3 (green) do show up. In mode z3 the observed ions execute a radial movement. Its relatively small amount of overlap with the gradient is well compensated by its small eigenfrequency yielding a higher Lamb-Dicke factor. As for mode z2 showing up distinctly, this is counter-intuitive, since the observed ions do not move along the gradient. The mode is in close spectral vicinity to the x-com mode. Here, we assume that the strong HF drive field induces a mixing process between x-com and z2, resulting in dressed modes which show up in the spectrum. As ions are not all located on the radio frequency node of the trap, they undergo micro motion, a precise calculation of eigenfrequencies would require a Floquet-Lyapunov-approach [Kau+12]. Because of a sufficiently small Matthieu parameter $q = 0.22$, even a pseudo-potential calculation fits the observed resonances well. The mode frequencies (green and red lines) were calculated from a pseudo potential approach and are within a $2\pi \times 10$ kHz area from a feature in the spectrum after an AC-Zeeman correction.

Chapter 6

Conclusion and Outlook

We have shown coupled dynamics of motional and internal spin states with a transition frequency as low as $2\pi \times 10$ MHz by employing static magnetic field gradients created with current-carrying wires placed underneath an ion trap chip. We presented detailed resolved-side band spectroscopy in linear and planar multi-ion crystals. Knowledge of the eigenmodes and frequencies are paramount for the implementation of quantum simulation and for the tailoring of interaction strength between spins. For the crystal shown in fig. 5.22, we could expect a spin-spin coupling according to eq. (2.61) of $J_{1,4}/2\pi = -16.2$ Hz between the two ions at the extreme positions with respect to the trap z-axis, with the main contribution from the z3-mode. The two ions displaced from the trap axis should show a coupling of $J_{2,3}/2\pi = +4.4$ Hz, with comparable contributions from the x-com and x3 mode. Recently, fast and robust gate operations have been proposed [Arr+17] and would be in experimental reach. Other interesting directions are, studies of phase transitions with competing spin-spin interactions [Kim+10] implemented on larger planar ion crystals or studies of revealing non-linear mode couplings [Ges+14; Lem+15]

6.1 Decoherence

The coherence time has to be improved for the above-mentioned schemes. If we align the external magnetic field along the trap axis, the coherence time increases by an order of magnitude as compared to the external magnetic field being aligned perpendicular to the trap surface, see fig. 5.10. The magnetic field perpendicular to the trap surface is created by only one coil, which is displaced from the trap in the y-direction, see fig. 3.3. A pair of coils in a Helmholtz configuration for a more homogeneous external magnetic field should be employed.

We have shown, coherence can be improved by an order of magnitude by employing a simple spin echo sequence. This implies that the source of the decoherence shows a periodicity in the order of $2\pi \times 20$ kHz and can be attributed to fast oscillating magnetic fields. More complex refocusing schemes [Pil+13] may be employed to counteract this problem as well as the use of dressed states, that are robust against magnetic field fluctuations [Tim+11]. A shielding box of Mu metal has also proven to be useful [Rus+16].

Furthermore, the in-vacuum cable for the current wires can be arranged within recesses of the copper-water-cooling-pipe that leads to the AlN chip carrier, thus offering cooling and shielding against electrical noise at the same time. Also, a

fourth wire or an antenna should be implemented for the HF signals, whereas the hitherto existing three wires should only be operated by the DC current (pulses).

6.2 Magnetic Field Gradient

As one can see from eq. (5.1), an improvement of the coupling will mainly be possible by further increasing the magnetic field gradient. Improvements to the presented setup would entail first of all a further miniaturisation. The system is designed to withstand 20 A, which would scale the gradient to roughly 40 T/m. The wires themselves have shown to withstand up to 16 A each. Therefore, the height of the wires could be lowered by a factor of two, using the same currents as in this work.

However, for 15 % higher currents than used, we noticed that the resonance frequency of the helical resonator for the RF drive starts to shift on a timescale of minutes. We address this to the heating of the filter board, where the current carrying wires and the RF supply is mounted. A separation of the boards hosting the DC and RF supply lines from a board containing the current carrying wires is advisable, in particular, if one wants to use higher current densities. Optionally combined with deep trenches in the supporting copper plate for further thermal isolation. The found heat resistance is one to two orders of magnitude higher than would be expected from the sole bulk material and has to be considered as a contact resistance between the different constituents of the assembly. Improvements might be possible by broadening the cooling pipe and finding a monolithic design for the pipe and the supporting copper plate.

A pulsed scheme with a low duty cycle would reduce the heat load significantly and thus allowing higher currents. This couldn't be established in this experiment due to a remanence, which shifts the centre of the magnetic quadrupole field and declines with a decay constant of several minutes after the current has been switched off.

The other way to increase the gradient is getting its source closer to the ions, either by minimising the trap electrodes or by integrating the wires and the trap electrodes in a tightly arranged multi layer chip. The first case is limited by anomalous heating of the ions and excessive stray light as the trap centre gets closer to the chip surface, the latter has to find a better way to get rid of the heat load and probably has to be operated in a cryogenic environment. Traps with trapping heights of 40 µm and less have been demonstrated [Mie+16]. With a slightly thinner substrate for the trap chip and the smaller wire height, the total ion wire distance could effectively be halved and the magnetic field gradient could be increased by a factor of up to four. If the problem with the heat load can be solved for good, flat wires made with thick-film technology are becoming more interesting. They could decrease a height of the wires by further factor of 2.

Appendix A

Current Wires

Copper

Images from optical microscopy of the current carrying copper wires for the magnetic gradient.

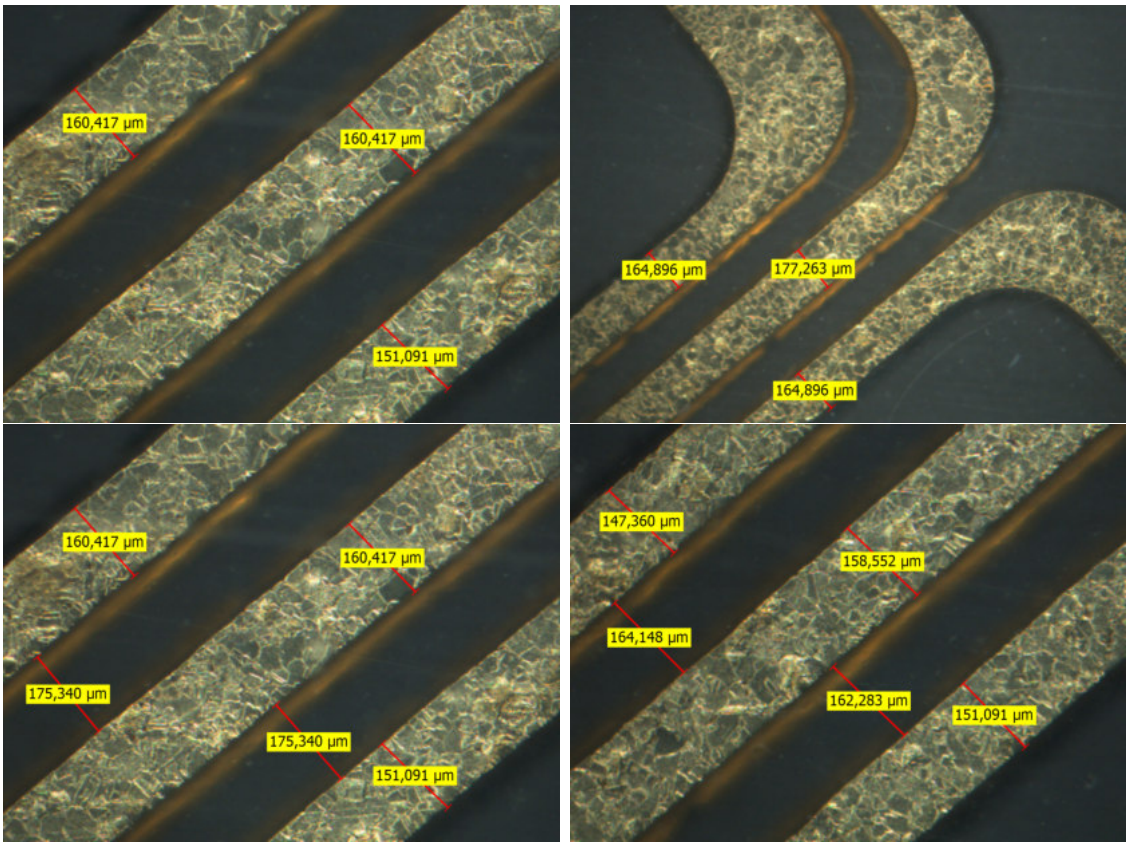

Figure A.1

AgPt

The following pages show an excerpt from the report on the fabrication of multi-layered AgPt wires with thickfilm technology from the Frauenhofer-Institut für Keramische Technologien und Systeme IKTS, Dresden.

2. 1. Schichtaufbau

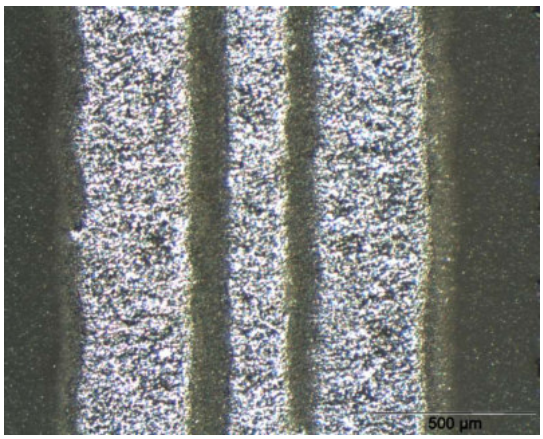

LB links µm	LB mitte µm	LB rechts µm	Abstand links-mitte µm	Abstand mitte-rechts µm
341,56	181,82	346,75	118,18	94,81
354,55	187,01	358,44	109,09	83,12
349,35	184,42	344,16	115,58	97,40
				85,71
348,48	184,42	349,78	114,29	90,26

LB…Leiterbahn

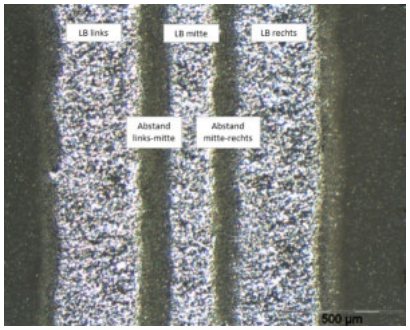

Kein direkter Kontakt zwischen den Leiterbahnen messbar

2. Schichtaufbau erfolgt

Fraunhofer

3. 2. Schichtaufbau

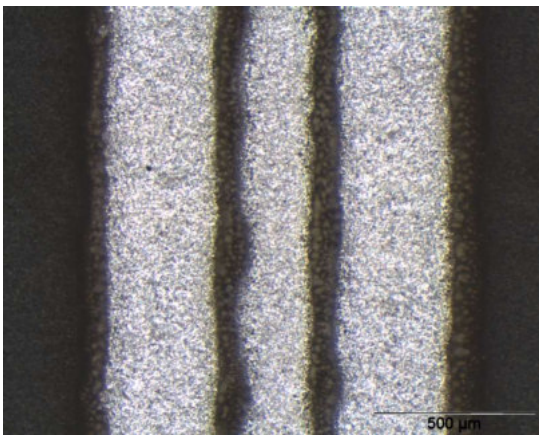

LB links µm	LB mitte µm	LB rechts µm	Abstand links-mitte µm	Abstand mitte-rechts µm
331,17	219,48	349,35	84,42	83,12
333,77	228,57	337,66	84,42	77,92
349,35	225,97	337,66	77,92	92,21
328,57	224,68	335,06	83,12	83,12
337,66	219,48	342,86	77,92	83,12
349,35	224,68	357,14	66,23	92,21
338,31	223,81	343,29	79,00	85,28

LB…Leiterbahn

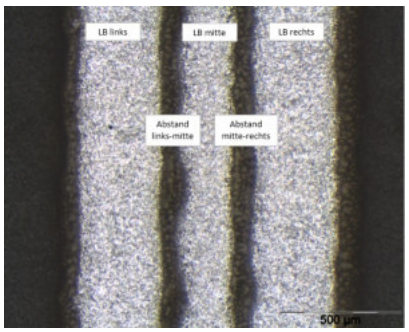

Direkter Kontakt zwischen den Leiterbahnen messbar

Kein Schichtaufbau kann mehr erfolgen
ABBRUCH

Fraunhofer

3. 2. Schichtaufbau

Direkter Kontakt zwischen den Leiterbahnen messbar

MOhm-Bereich, wahrscheinlich noch kein direkter Kontakt, aber viele Silberverinselungen nahe zwischen den Leiterzügen

Ohm-Bereich, direkter Kontakt (siehe Bilder)

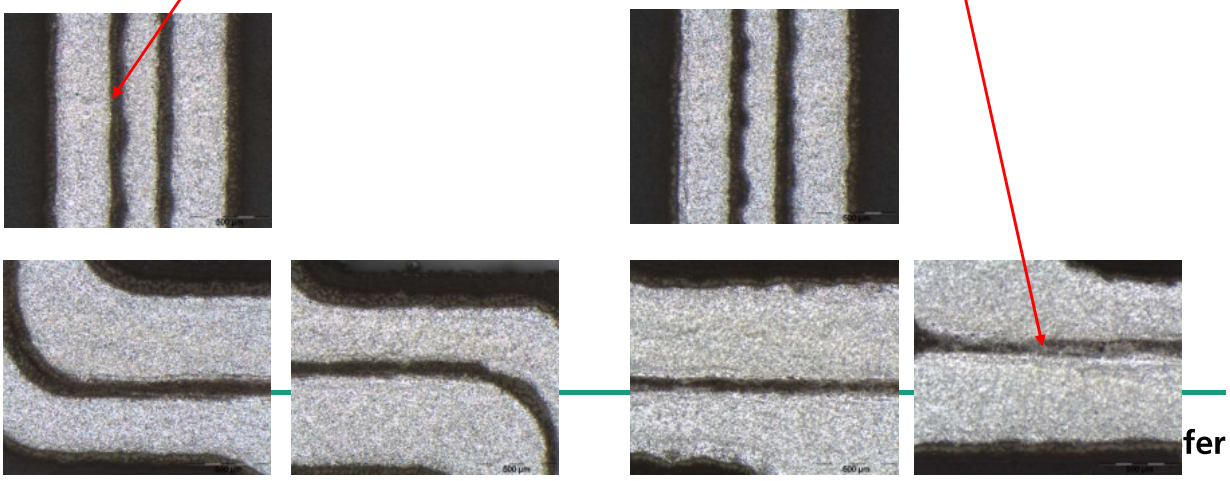

fer

3. 2. Schichtaufbau → Silberverinselungen im Detail

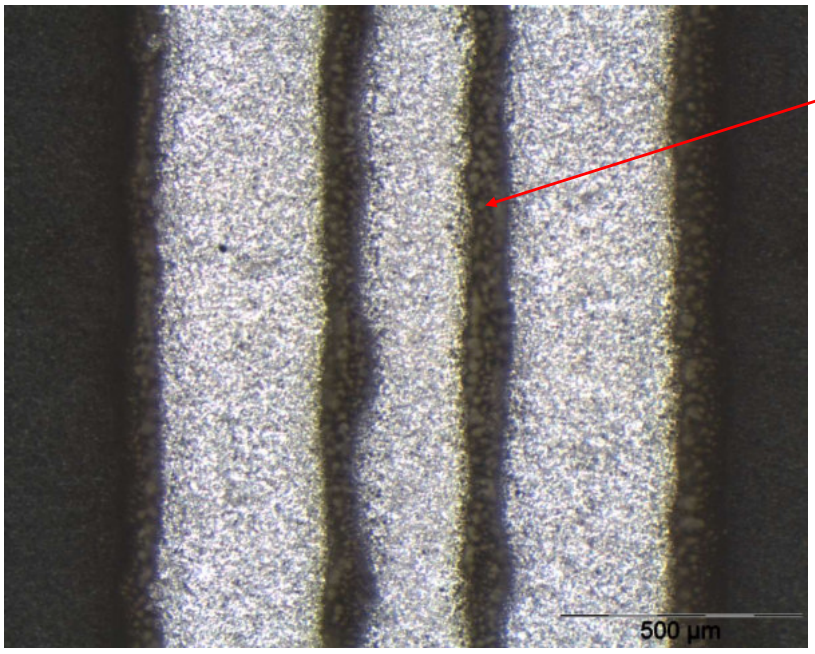

Silberverinselungen

Möglicherweise können diese zum hochohmigen Kontakt führen

Appendix B

List of Figures

Appendix C

References

[Alh+96] R. Alheit et al. "Higher order non-linear resonances in a Paul trap". In: *Int. J. Mass Spectrometry and Ion Processes* 154.3 (1996), pp. 155 –169.

[Alo+16] J. Alonso et al. "Generation of large coherent states by bang–bang control of a trapped-ion oscillator". In: *Nature Commun.* 7 (2016), p. 11243.

[Arr+17] I. Arrazola et al. "Fast and Robust Two-Qubit Gates with Microwave-Driven Trapped Ions". In: *arXiv:1706.02877* (2017).

[BCS04] G. Benenti, G. Casati, and G. Strini. *Principles of Quantum Computation and Information - Volume I: Basic Concepts*. 3rd. Singapore: World Scientific, 2004.

[BG+13] N. Bar-Gill et al. "Solid-state electronic spin coherence time approaching one second". In: *Nat. Phys.* 4 (2013), p. 1743.

[BKH92] G. Birkl, S. Kassner, and Walther H. "Multiple-shell structures of laser-cooled $^{24}Mg^{+}$ ions in a quadrupole storage ring". In: *Nature* 357 (1992), pp. 310–313.

[BS15] A. Bautista-Salvador. "Integrated Electromagnets and Radiofrequency Spectroscopy in a Planar Paul Trap". PhD thesis. Universität Ulm, 2015.

[Bar+22] P. Barthel et al. "Robust Two-Qubit Gates Using Pulsed Dynamical Decoupling". In: *arXiv:2208:00187* (2022).

[Ben82] P. Benioff. "Quantum mechanical hamiltonian models of turing machines". In: *J. Stat. Phys.* 29.3 (1982), pp. 515–546.

[Ber+11] A. Bermudez et al. "Frustrated Quantum Spin Models with Cold Coulomb Crystals". In: *Phys. Rev. Lett.* 107 (2011), p. 207209.

[Bri+12] J. Britton et al. "Engineered two-dimensional Ising interactions in a trapped-ion quantum simulator with hundreds of spins". In: *Nature* 484 (2012), p. 489.

[CG69] K. E. Cahill and R. J. Glauber. "Ordered Expansions in Boson Amplitude Operators". In: *Phys. Rev.* 177 (5 1969), pp. 1857–1881.

[CLJ08] J. Chiaverini and W. E. Lybarger Jr. “Laserless trapped-ion quantum simulations without spontaneous scattering using microtrap arrays”. In: *Phys. Rev. A* 77.2 (2008), p. 022324.

[CZ95] J. I. Cirac and P. Zoller. “Quantum Computations with Cold Trapped Ions”. In: *Phys. Rev. Lett.* 74.20 (1995), pp. 4091–4094.

[Chi+05] J. Chiaverini et al. “Surface-electrode architecture for ion-trap quantum information processing”. In: *Quant. Inf. Comput.* 5.6 (2005), pp. 419–439.

[Cit+77] M.L. Citron et al. “Experimental study of power broadening in a two-level atom”. In: *Phys. Rev. A* 16 (4 1977), pp. 1507–1512.

[Deu07] T. W. Deuschle. “Kalte Ionenkristalle in einer segmentierten Paul-Falle”. PhD thesis. Universität Ulm, 2007.

[DiV00] D. P. DiVincenzo. “The Physical Implementation of Quantum Computation”. In: *arXiv:quant-ph/0002077* (2000).

[Don+05] E. A. Donley et al. “Double-pass acousto-optic modulator system”. In: *Rev. Sci. Instrum.* 76 (2005), p. 063112.

[Dre+83] R. W. P. Drever et al. “Laser phase and frequency stabilization using an optical resonator”. In: *Appl. Phys. B* 31.2 (1983), pp. 97–105.

[Enz+00] D. G. Enzer et al. “Observation of Power-Law Scaling for Phase Transitions in Linear Trapped Ion Crystals”. In: *Phys. Rev. Lett.* 85 (12 2000), pp. 2466–2469.

[Fey82] R. P. Feynman. “Simulating Physics with Computers”. In: *Int. J. Theor. Phys.* 21.6/7 (1982), pp. 467–488.

[Fis+08] S. Fishman et al. “Structural phase transitions in low-dimensional ion crystals”. In: *Phys. Rev. B* 77 (2008), p. 064111.

[Fli09] T. Fließbach. *Mechanik*. 6th. Heidelberg: Spektrum Akademischer Verlag, 2009.

[Fox06] M. Fox. *Quantum Optics - An Introduction*. 1th. New York: Oxford University Press Inc., 2006.

[Ges+14] M. Gessner et al. “Nonlinear spectroscopy of controllable many-body quantum systems”. In: *New J. Phys.* 16 (2014), p. 092001.

[Gro+04] S. Groth et al. “Atom chips: Fabrication and thermal properties”. In: *Appl. Phys. Lett.* 85 (2004), p. 2980.

[Gro97] L. K. Grover. “Quantum Mechanics Helps in Searching for a Needle in a Haystack”. In: *Phys. Rev. Lett.* 79 (2 1997), pp. 325–328.

[Gul+01] S. Gulde et al. “Simple and efficient photo-ionization loading of ions for precision ion-trapping experiments”. In: *Appl. Phys. B* 73.8 (2001), pp. 861–863.

[HD13] H. Haeffner and N. Daniilidis. *Private Communication*. University of California, 2013.

[HRB08] H. Häffner, C. Roos, and R. Blatt. “Quantum computing with trapped ions”. In: *Physics Reports* 469 (2008), p. 155.

[HS75] T. W. Hänsch and A. L. Schawlow. "Cooling of Gases by Laser Radiation". In: *Opt. Commun.* 13.1 (1975), p. 68.

[Har+16] T. P. Harty et al. "High-Fidelity Trapped-Ion Quantum Logic Using Near-Field Microwaves". In: *Phys. Rev. Lett.* 117 (2016), p. 140501.

[Hit+12] D. A. Hite et al. "100-Fold Reduction of Electric-Field Noise in an Ion Trap Cleaned with In Situ Argon-Ion-Beam Bombardment". In: *Phys. Rev. Lett.* 109 (10 2012), p. 103001.

[Hou08] M. G. House. "Analytic model for electrostatic fields in surface-electrode ion traps". In: *Phys. Rev. A* 78 (2008), p. 033402.

[Isl+13] R. Islam et al. "Emergence and Frustration of Magnetism with Variable-Range Interactions in a Quantum Simulator". In: *Science* 340.6132 (2013), pp. 583–587.

[JVW09] M. Johanning, A. F. Varón, and C. Wunderlich. "Quantum simulations with cold trapped ions". In: *J. Phys. B* 42.15 (2009), p. 154009.

[Jam98] D. F. V. James. "Quantum dynamics of cold trapped ions with application to quantum computation". In: *Appl. Phys. B* 66.2 (1998), pp. 181–190.

[Joh+09] M. Johanning et al. "Individual Addressing of Trapped Ions and Coupling of Motional and Spin States Using rf Radiation". In: *Phys. Rev. Lett.* 102 (7 2009), p. 073004.

[Jur+14] P. Jurcevic et al. "Quasiparticle engineering and entanglement propagation in a quantum many-body system". In: *Nature* 511.7508 (2014), pp. 202–205.

[Jur+17] P. Jurcevic et al. "Direct Observation of Dynamical Quantum Phase Transitions in an Interacting Many-Body System". In: *Phys. Rev. Lett.* 119 (2017), p. 080501.

[Kau+12] H. Kaufmann et al. "Precise Experimental Investigation of Eigenmodes in a Planar Ion Crystal". In: *Phys. Rev. Lett.* 109 (26 2012), p. 263003.

[Kau+17] H. Kaufmann et al. "Fast ion swapping for quantum information processing". In: *Phys. Rev. A* 95 (2017), p. 052319.

[Kaw+17] Y. Kawai et al. "Surface-electrode trap with an integrated permanent magnet for generating a magnetic-field gradient at trapped ions". In: *J. Phys. B* 50.2 (2017), p. 025501.

[Khr+12] A. Khromova et al. "Designer Spin Pseudomolecule Implemented with Trapped Ions in a Magnetic Gradient". In: *Phys. Rev. Lett.* 108 (22 2012), p. 220502.

[Kie+23] Dominik Kiesenhofer et al. "Controlling Two-Dimensional Coulomb Crystals of More Than 100 Ions in a Monolithic Radio-Frequency Trap". In: *PRX Quantum* 4 (2 2023), p. 020317.

[Kim+10] K. Kim et al. "Quantum simulation of frustrated Ising spins with trapped ions". In: *Nature* 465 (2010), pp. 590–593.

[Kos+05] N. Kosugi et al. "Theory of damped Rabi oscillations". In: *Phys. Rev. B* 72 (17 2005), p. 172509.

[Kot+14] S. Kotler et al. “Measurement of the magnetic interaction between two bound electrons of two separate ions”. In: *Nature* 510 (2014), p. 376.

[Kum+11] M. Kumph et al. “Two-dimensional arrays of radio-frequency ion traps with addressable interactions”. In: *New J. Phys.* 13.7 (2011), p. 073043.

[Kum+16] M. Kumph et al. “Operation of a planar-electrode ion-trap array with adjustable RF electrodes”. In: *New J. Phys.* 18 (2016), p. 023047.

[Kun+14] P. J. Kunert et al. “A planar ion trap chip with integrated structures for an adjustable magnetic field gradient”. In: *Appl. Phys. B* 114.1 (2014), pp. 27–36.

[Lak+15] K. Lake et al. “Generation of spin-motion entanglement in a trapped ion using long-wavelength radiation”. In: *Phys. Rev. A* 91 (1 2015), p. 012319.

[Lan+11] B. P. Lanyon et al. “Universal Digital Quantum Simulation with Trapped Ions”. In: *Science* 334.6052 (2011), pp. 57–61.

[Lei+03a] D. Leibfried et al. “Experimental demonstration of a robust, high-fidelity geometric two ion-qubit phase gate”. In: *Nature* 422.6930 (2003), pp. 412–415.

[Lei+03b] D. Leibfried et al. “Quantum dynamics of single trapped ions”. In: *Rev. Mod. Phys.* 75.1 (2003), pp. 281–324.

[Lem+15] A. Lemmer et al. “Two-Dimensional Spectroscopy for the Study of Ion Coulomb Crystals”. In: *Phys. Rev. Lett.* 114 (2015), p. 073001.

[MK01] Malinovsky, V. S. and Krause, J. L. “General theory of population transfer by adiabatic rapid passage with intense, chirped laser pulses”. In: *Eur. Phys. J. D* 14.2 (2001), pp. 147–155.

[MW01] F. Mintert and Ch. Wunderlich. “Ion-Trap Quantum Logic Using Long-Wavelength Radiation”. In: *Phys. Rev. Lett.* 87 (25 2001), p. 257904.

[Mac12] T. Macha. “Frequenzstabilisierung eines Titan-Saphir-Lasers und Verbesserung von Qubits mit Ca^+-Ionen”. MA thesis. Johannes Gutenberg-Universität Mainz, 2012.

[Mie+16] M. Mielenz et al. “Arrays of individually controlled ions suitable for two-dimensional quantum simulations,” in: *Nat. Commun.* 7 (2016), p. 11839.

[Mon+11] T. Monz et al. “14-Qubit Entanglement: Creation and Coherence”. In: *Phys. Rev. Lett.* 106 (13 2011), p. 130506.

[Osp+11] C. Ospelkaus et al. “Microwave quantum logic gates for trapped ions”. In: *Nature* 476 (2011), pp. 181–184.

[Pau90] W. Paul. “Electromagnetic Traps for Charged and Neutral Particles”. In: *Rev. Mod. Phys.* 62.3 (1990), pp. 531–540.

[Pil+13] C. Piltz et al. “Protecting Conditional Quantum Gates by Robust Dynamical Decoupling”. In: *Phys. Rev. Lett.* 110 (20 2013), p. 200501.

[Pil+14] C. Piltz et al. “A trapped-ion-based quantum byte with 10^{-5} next-neighbour cross-talk”. In: *Nat. Comm.* 5 (2014), p. 4679.

[Por+08] D. Porras et al. “Mesoscopic spin-boson models of trapped ions”. In: *Phys. Rev. A* 78 (1 2008), p. 010101.

[Pos+09] U. G. Poschinger et al. “Coherent manipulation of a 40 Ca + spin qubit in a micro ion trap”. In: *J. Phys. B* 42.15 (2009), p. 154013.

[Qia+22] M. Qiao et al. “Observing frustrated quantum magnetism in two-dimensional ion crystalss”. In: *arXiv:2204.07283 [quant-ph]* (2022).

[Rei02] J. Reichel. “Microchip traps and Bose–Einstein condensation”. In: *Applied Physics B* 74.6 (2002), pp. 469–487.

[Roo00] C. F. Roos. “Controlling the quantum state of trapped ions”. PhD thesis. Leopold-Franzens-Universität Innsbruck, 2000.

[Rot03] D. Rotter. “Photoionisation von Kalzium”. MA thesis. Universität Innsbruck, 2003.

[Rus+14] T. Ruster et al. “Experimental realization of fast ion separation in segmented Paul traps”. In: *Phys. Rev. A* 90 (3 2014), p. 033410.

[Rus+16] T. Ruster et al. “A long-lived Zeeman trapped-ion qubit”. In: *Appl. Phys. B* 122.10 (2016), pp. 1–7.

[Rus+17] T. Ruster et al. “Entanglement-based dc magnetometry with separated ions”. In: *arXiv:* 1704.01793 [quant-ph] (2017), supplementary.

[Sho97] P. W. Shor. “Polynomial-Time Algorithms for Prime Factorization and Discrete Logarithms on a Quantum Computer”. In: *SIAM J. Comput.* 26 (1997), p. 1484.

[Sin+02] K. Singer et al. “Low-cost mechanical shutter for light beams”. In: *Rev. Sci. Instrum.* 73 (2002), p. 4402.

[Sri+21] R. Srinivas et al. “High-fidelity laser-free universal control of trapped ion qubits”. In: *Nature* 597 (2021), 209–213.

[Tim+11] N. Timoney et al. “Quantum gates and memory using microwave-dressed states”. In: *Nature* 476 (2011), pp. 185–188.

[Tur37] A. M. Turing. “On Computable Numbers, with an Application to the Entscheidungsproblem”. In: *Proc. London Math. Soc.* s2-42 (1937), pp. 230–265.

[Ulm+13] S. Ulm et al. “Observation of the Kibble–Zurek scaling law for defect formation in ion crystals”. In: *Nature Commun.* 4 (2013), p. 2290.

[Val+21] C. H. Valahu et al. “Robust entanglement by continuous dynamical decoupling of the J-coupling interaction”. In: *New J. Phys.* 23 (2021), p. 113012.

[WDW78] D. J. Wineland, R. E. Drullinger, and F. L. Walls. “Radiation-Pressure Cooling of Bound Resonant Absorbers”. In: *Phys. Rev. Lett.* 40 (25 1978), pp. 1639–1642.

[WFW93] Y. Wang, J. Franzen, and K. P. Wanczek. “The non-linear resonance ion trap. Part 2. A general theoretical analysis”. In: *Int. J. Mass. Spectrom.* 124 (1993), pp. 125–144.

[WI79] D. J. Wineland and Wayne M. Itano. “Laser cooling of atoms”. In: *Phys. Rev. A* 20 (4 1979), pp. 1521–1540.

[WSNR17] M. L. Wall, A. Safavi-Naini, and A. M. Rey. "Boson-mediated quantum spin simulators in transverse fields: XY model and spin-boson entanglement". In: *Phys. Rev. A* 95 (1 2017), p. 013602.

[Wal+11] A. Walther et al. "Single ion as a shot-noise-limited magnetic-field-gradient probe". In: *Phys. Rev. A* 83 (6 2011), p. 062329.

[Wan+09] S. X. Wang et al. "Individual addressing of ions using magnetic field gradients in a surface-electrode ion trap". In: *Appl. Phys. Lett.* 94 (2009), p. 094103.

[Wan15] ST. Wang. "Quantum Computation under Micromotion in a Planar Ion Crystal." In: *Sci Rep* 5 (2015), p. 8555.

[War+13] U. Warring et al. "Techniques for microwave near-field quantum control of trapped ions". In: *Phys. Rev. A* 87 (2013), p. 013437.

[Wei+15] S. Weidt et al. "Ground-State Cooling of a Trapped Ion Using Long-Wavelength Radiation". In: *Phys. Rev. Lett.* 115 (1 2015), p. 013002.

[Wei+16] S. Weidt et al. "Trapped-Ion Quantum Logic with Global Radiation Fields". In: *Phys. Rev. Lett.* 117 (22 2016), p. 220501.

[Wel+11] J. Welzel et al. "Designing spin-spin interactions with one and two dimensional ion crystals in planar micro traps". In: *Eur. Phys. J. D* 65.1 (2011), pp. 285–297.

[Wie11] A. Wiens. "Detection of Qubit registers in a micro trap". MA thesis. Johannes Gutenberg-Universität Mainz, 2011.

[Win+98] D. J. Wineland et al. "Experimental Issues in Coherent Quantum-State Manipulation of Trapped Ions". In: *J. Res. Natl. Inst. Stand. Technol.* 103.3 (1998), pp. 259–328.

[Wun+07] C. Wunderlich et al. "Robust state preparation of a single trapped ion by adiabatic passage". In: *J. Mod. Opt.* 54 (2007), p. 1541.

[Wun02] C. Wunderlich. "Conditional Spin Resonance with Trapped Ions". In: *Laser Physics at the Limits*. Ed. by H. Figger, C. Zimmermann, and D. Meschede. Berlin, Heidelberg: Springer, 2002, pp. 261–273.

[ZCH23] J. Zhang, B. T. Chow, and P. C. Haljan. "Spectroscopic characterization of the quantum linear-zigzag transition in trapped ions". In: *npj Quantum Inf* 9 (2023), p. 68.

[Zar+19] G. Zarantonello et al. "Robust and Resource-Efficient Microwave Near-Field Entangling $^9Be^+$ Gate". In: *Phys. Rev. Lett.* 123 (2019), p. 260503.

[Zha+17] JJ. Zhang et al. "Observation of a Many-Body Dynamical Phase Transition in a 53-Qubit Quantum Simulator". In: *Nature* 551 (2017), p. 601.

[Zie12] F. Ziesel. "Quantum State Manipulation and Dynamics in Micro Ion Traps". PhD thesis. Universität Ulm, 2012.

Appendix D

Scientific Publications

Publications in Journals

Spin and motion dynamics with zagzag ion crystals in transverse magnetic field gradients
J. Welzel, F. Stopp, and F. Schmidt-Kaler
J. Phys. B: At. Mol. Opt. Phys. **52** (2019) p.025301

Poster Presentations

RF-Spektroskopie von $^{40}Ca^{+}$ Kristallen
J. Welzel, F. Stopp, F. Schmidt-Kaler
DPG Spring Meeting 2017 in Mainz

Aufbau einer hybriden Ionenfalle für Spin-Spin Wechselwirkungen
J. Welzel, N. Kurz, A. Bautista-Salvador, F. Schmidt-Kaler
DPG Spring Meeting 2014 in Berlin

Implementing Tools for quantum simulations in a planar trap
N. Kurz, J. Welzel, A. Bautista-Salvador, R. Gerritsma, F. Schmidt-Kaler
Annual Restreat 2013 of SFB/TRR49

Radiofrequency Spectroscopy of a single $^{40}Ca^{+}$ qubit
J. Welzel, A. Bautista-Salvador, N. Kurz, R. Gerritsma, F. Schmidt-Kaler
DPG Spring Meeting 2013 in Hannover

Appendix E

Curriculum Vitae

Persönliche Daten

Jens Welzel
Hegaustraße 3/1
78315 Radolfzell

Geb. am 05. Januar 1985 in Überlingen
Ledig, deutsch

E-Mail: jens.welzel@web.de

Berufspraxis

seit 07.2022	Zugelassener Vertreter vor dem Europäischen Patentamt
seit 07.2017	Daub, Patentanwaltskanzlei & Rechtsanwaltskanzlei in Überlingen Patentsachbearbeiter
03.2011-03.2017	Johannes Gutenberg-Universität Mainz Wissenschaftlicher Mitarbeiter in der Abteilung *Kalte Ionen und Experimentelle Quanteninformation*.

Studium

seit 12.2013	Johannes Gutenberg-Universität Mainz Promotionsstudium mit dem Thema *Spindependent forces in planar Paul traps*. Betreuer: Prof. Dr. Ferdinand Schmidt-Kaler
10.2005–03.2011	Universität Ulm Diplomstudiengang Physik mit Abschlussnote: sehr gut (1,0)

- Schwerpunktfächer: Quanteninformationsverarbeitung, Theorie de kondensierten Materie, Quantenfeldtheorie
- Diplomarbeit im Institut für Quanteninformationsverarbeitung mit dem Thema *Planare Spin-Spin Simulatoren* und Note sehr gut (1,0)
  Betreuer: Prof. Dr. Ferdinand Schmidt-Kaler

Schulbildung & Wehrdienst

10.2004–06.2005	Grundwehrdienst und Ausbildung zum Fernmelder in Meßstetten
09.1995–06.2004	Nellenburg-Gymnasium Stockach Abschluss mit Abitur und Note sehr gut (1,1)

Radolfzell, 1. Oktober 2023